Chain Growth of Alkenes to Produce Commodity Chemicals with Heterogeneous Catalysts

By

Zhuoran Xu

A dissertation submitted in partial fulfillment of

the requirements for the degree of

Doctor of Philosophy

(Chemical Engineering)

At the

UNIVERSITY OF WISCONSIN-MADISON

2017

Date of final oral examination: 11/07/2017

The dissertation is approved by the following members of the final oral committee:

George W. Huber, Professor, Chemical and Biological Engineering

James A. Dumesic, Professor, Chemical and Biological Engineering

Manos Mavrikakis, Professor, Chemical and Biological Engineering

Thatcher W. Root, Professor, Chemical and Biological Engineering

Ive Hermans, Professor, Chemistry

Abstract

Current US natural gas prices are the lowest in nearly 20 years thanks to the recent development of hydraulic fracturing technology. The shale gas incentive has provided the olefin industry an opportunity to obtain light alkenes at lower prices and to convert light alkenes into molecules with higher values. The oligomerization of light alkene into longer chain oligomers with controlled chain length and carbon bone structure is commercially achieved with homogeneous catalysts because of the poor selectivity with heterogeneous catalysts. The research here presents different approaches for the oligomerization of light olefins with a variety of heterogeneous catalysts.

Medium-pore zeolites have a higher selectivity towards true oligomers with ethylene or 1-butene as a feedstock than the small-pore and large-pore zeolite catalysts. Specifically, H-ferrierite has the highest dimer selectivity from 1-butene among the commercially available un-modified zeolites including H-ZSM-5, H-Mordenite and H-β zeolite. Deactivation is inhibited when operating 1-butene conversion with H-ferrierite in the supercritical phase. Two-dimensional gas chromatograph (2D-GC) was used to analyze the complex product mixtures from this reaction which allows us to separate and quantify nearly a hundred olefin isomers. Over 99% of the oligomer products observed from H-ferrierite were branched. A carbocation-based reaction mechanism occurs with zeolites which forms branched olefins due to the catalysis of the Brønsted acid sites naturally existing within a zeolite framework.

A carbon supported cobalt oxide catalyst (CoO_X/N-C) was studied for light olefin conversion. The catalyst was synthesized by depositing cobalt nitrate precursor onto a mesoporous carbon material previously treated with NH_4OH, followed by decomposition of cobalt salt to form cobalt oxide. Pretreated at 230 ℃, the CoO_X/N-C produced 70-85% of linear dimer among all the dimers observed from 1-butene conversion. The Co(III) content is sensitive to the pretreatment temperature, and the catalyst pretreated at 230 ℃ has the highest Co(III) content with the highest oligomerization activity. The side reaction involves double bond isomerization of the alpha-olefin feed to form internal olefins. The internal olefins are inactive towards oligomerization. Nevertheless, CoO_X/N-C was found to be active and selective in converting a diversity of light LAOs including ethylene, propylene, 1-butene and 1-hexene into linear dimers with above 50% distribution. The isomerization of 1-butene or 1-hexene was a competing reaction that effectively inhibited the formation of branched dimers. The products from this catalyst follow a Cossee-type mechanism. The Cossee-Arlman mechanism was initially proposed to describe the polymerization of α-

olefins with Ziegler-Natta catalysts or metallocene catalysts [1], where the oligomer chain continues to grow by combining the monomer with the intermediate coordination complex. The catalyst however, suffered from deactivation. Catalyst deactivation is mainly caused by site blocking from olefin accumulation.

A bimetallic, chromium-promoted cobalt on carbon catalyst (Cr-CoO_X/N-C) was synthesized, characterized, and tested for ethylene and 1-butene conversion. No significant loss of activity was observed when 1-butene was converted with Cr-CoO_X/N-C. The bimetallic catalyst showed enhanced activity and stability in converting both olefin feeds as compared to CoO_X/N-C. Particularly, the Cr-CoO_X/N-C was able to deliver a 1-butene selectivity of 82.4% at an ethylene conversion of 8.9%. Addition of Cr altered the cobalt oxidation state with more Co (II) existing in Cr-CoO_X/N-C compared to CoO_X/N-C. The Co (II) species in the catalyst is beneficial for the final desorption step of the oligomer products from the active site – which could be the reason why a more stable catalyst is attained where oligomer accumulation can be effectively avoided. A preliminary kinetic modelling for ethylene conversion with Cr-CoO_X/N-C was constructed. The results from the kinetic modelling pointed to a higher (50%) active site dispersion that was achieved with the Cr-promoted catalyst as compared to the non-promoted catalyst.

Acknowledgments

I feel grateful and fortunate to have a number of people in my life that makes the completion of my PhD thesis smooth. I owe a debt of gratitude to Prof. George W. Huber, whose optimism and passion in research have influenced me greatly in the past five years. Without his encouragement and trust in me, I would still be that timid student without any clue of where to go. I have harvested tremendously under his guidance. To name a few, I've learnt to analyze research data and different prospectives in a more rigorous way; I become experienced in public presentations due to multiple opportunities to attend conferences; and I have grown greatly in scientific writing and communication. I want to thank Prof. Hermans and Prof. Mavrikakis, for giving me the chances to collaborate with their group members, and for providing me with helpful guidance in my research work. I would like to thank Prof. Dumesic, for opening the door to the fundamentals in kinetics during two excellent courses. I want to thank Prof. Root for teaching an interesting course and exposing me to the energy-related topics. Thank you all for your interest in my work and presenting as my committee members.

I would have accomplished much less without the help and support from the collaborators from various research groups and especially, from Dow Chemical who has provided funding for my study. I want to thank Devon Resenfeld, Jessica Rogers and Yomaira Pagan-Torres for their discussion about my research, and for their comments on my manuscript which greatly improved the quality of my work. I want to thank Yong Tae Kim who has trained me upon my joining the group on various techniques and taught me many useful skills in research. I want to thank Joe Chada and Dongting Zhao for being such great collaborators and providing support for my work; plus my life wouldn't be that enjoyable without their friendship. I would like to thank Carlos Carrero and Lang Xu for their support in the metarials and kinetics work in my research.

I continuously found myself immersed in a pool of warm-hearted people in Huber's research group. I want to thank Prof. James Miller, Ronen Weingarten, Chris Gilbert, Ani Upadhye, Juliana Espindola, Jechan Lee, Hyung Ju Kim, Insoo Ro and Pranav Karanjkar for providing me help whenever I reached out to them. I want to thank Nat Eagan, Peter Galebach, Daniel McClelland, Siddarth Krishna, Kevin Barnett, Keishla Rivera-Dones, Theodore Walker and Mark Lindsay for making Huber's group functioning at its fullest from time to time. I would like to thank Eric Codner, Mary Heimbecker, Russ Poyner and Kathy Heinzen for being such great staffs in the CBE department who have helped me in various situations.

Madison has always been a great place to live – thanks to my friends who are always there to accompany me during my up and down times. They include: Yuying Shi, Jiayue He, Yifei Liu, Mrunmayi Kumbhalkar, Ling Hao, Qing Yu, Haoyan Jia, Yunhai Bai, Sha Li, Xuanrong Guo, Wujun Liu, Xiao Zhang, Lu Guo, Yajin Chen. I feel lucky to have known them in the past 5-6 years. I want to thank them all for their support in me.

Nothing I accomplished would have been possible if my parents did not believe in me every step of the way. Their happiness and encouragements mean everything to me and they're the motivation that pushes me forward every day. I am fairly certain that I received blesses from my grandparents in haven, too. Lastly, I would like to thank Josh Frederick, for his endless support and care for me in my life, and for cultivating the calm and pleasant characters in myself.

Table of Contents

List of Figures

List of Tables

CHAPTER 1 Introduction

The United States' production of natural gas has increased by 35% in the past decade thanks to the large-scale implementation of hydraulic fracturing technology [2]. Steam cracking of the light alkane compounds of the natural gas produces alkenes. Alkenes are a family of unsaturated hydrocarbons that provide the petroleum and chemical industries with a platform to derive a diversity of products *via* several classes of chemical reactions. Specifically, the capability of oligomerizing light alkenes into longer chain oligomers is critical in obtaining the desired carbon bone structure applicable for a number of downstream processes. Based on the branchness and the position of the double bond, the oligomer products can be classified into three categories: linear alpha olefin (LAO), linear internal olefin (LIO), and branched olefin. The branched oligomer products are useful to make fuel additives to improve the octane number in a gasoline product following a hydrogenation process. LAOs, especially those with a relatively low carbon number such as 1-butene, 1-hexene and 1-octene are used as important comonomers in the production of polyethylene. The average annual growth rate between 2012 and 2018 for LAOs used for such purpose is 4.5% [3]. Alternatively, straight-chain olefins including both LAO and LIO are important building blocks for the synthesis of oxo-alcohols. The market of oxo-alcohols is forecasted to be around 12,963 KT in terms of volume in 2020 growing at a compound annual growth rate (CAGR) around 4.3% [4].

The current manufacture of the LAO products is achieved exclusively with homogeneous catalysts. For example, in the Ineos (Ethyl) Process, i.e. stoichiometric Ziegler process, an excess amount of ethylene is contacted with a stoichiometric quantity of triethylaluminum [5] to produce polyethylene. An on-purpose route to produce 1-hexene from ethylene was established by Chevron Phillips Chemicals that adopts a chromium-based homogeneous catalyst [6]. A flow diagram demonstrating the processes to produce LAOs with homogeneous catalyst systems is shown in Figure 1.1.

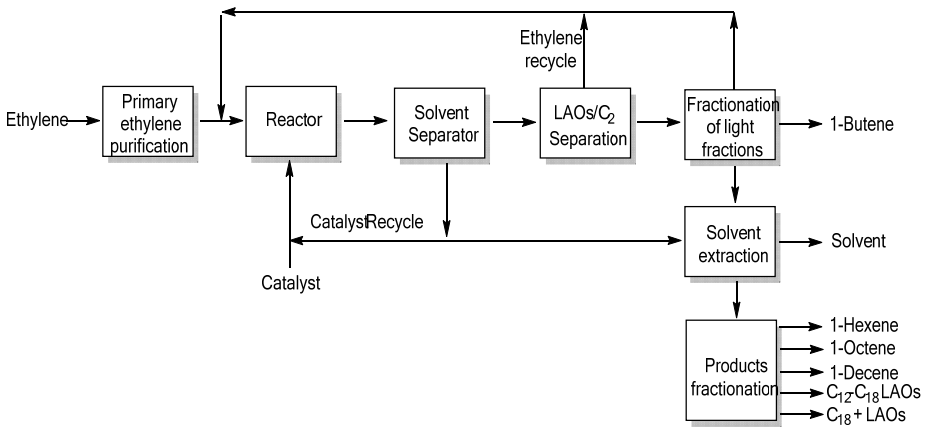

Figure 1.1 Block diagram of the conventional linear alpha olefin process catalyzed by a homogeneous catalyst, adapted from Belov [7].

There are generally two families of homogeneous catalysts for light olefin oligomerization to produce LAOs. One is a trialkylaluminum-based compound with Ziegler catalyst as a representative for ethylene oligomerization [8]. The chain growth is continued when the incoming ethylene molecule inserts into the metal-carbon bond. This type of chain growth frequently results in a broad range of oligomer product distribution thus making it hard to control the carbon chain length in the product. This type of chain growth is described by a Cossee-type mechanism [1]. The other family of homogeneous catalyst is a metalloorganic-based compound with metallocene catalyst as a representative for ethylene oligomerization. A handful of transition metals, including Ti, Zr, Pd, Ni, Co, Fe and Cr were shown to be active for LAO synthesis from ethylene [9-14]. The product distribution is frequently determined by the stability of the metallacyclic intermediate formed upon ethylene insertion, as depicted in Figure 1.2. Such type of chain growth is described by a metallacycle mechanism.

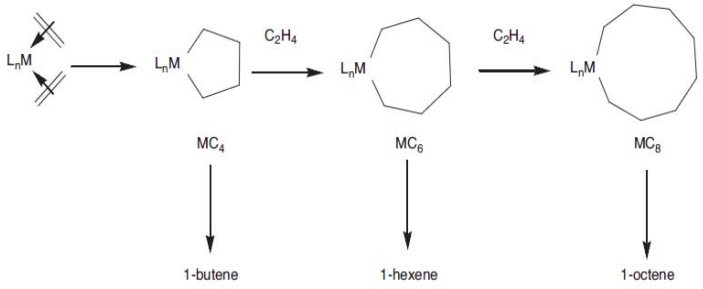

Figure 1.2 Metallacyclic mechanism for selective ethylene oligomerization adapted from Forestière [15].

The homogeneous catalysis processes suffer from several challenges including the high purity requirements of feed molecules (below 10 ppm sulfur content [16]). The catalysts require an activator, recycling the solvent and have difficulty with recycling/regeneration. Nevertheless, the key advantage of homogeneous catalysts is that high selectivity and activity towards linear oligomers are obtained. Replacing homogeneous catalysts with an efficient heterogeneous analogue that is potentially regenerable, does not require addition of an activator and is resistant to feed impurities could drastically lower the capital and operating costs, and hence improve the competitiveness of the US chemical industry.

Oligomerization of 1-butene has been studied with both homogeneous and heterogeneous catalysts. The catalysts with the highest selectivity towards linear octenes are tabulated in Table 1.1. A homogeneous catalysts with a cobalt center surrounded by bis(imino)pyridine ligand showed the highest linear octene distribution (70-98%) reported. An unmodified ferrierite catalyst, as will be described more in detail in Chapter 2, did not show any significant selectivity of linear octene. Ion-exchanged zeolites were also studied by early literatures. The incorporation of a transition metal such as Co and Ni into a zeolite framework was able to show ~35% linear octene distribution. A carbon supported cobalt catalyst, which was synthesized and tested for the conversion of a series light olefins including ethylene, propylene, 1-butene and 1-hexene in an early patent, showed above 50% selectivity towards the linear dimer products.

Table 1.1 A summary of literature research on the conversion of 1-butene into linear octenes with homogeneous and heterogeneous catalysts.

Catalyst	Bis(imino)pyridine cobalt [17]	H-FER [18]	Co,Na,Ca-Y [19]	HNaNi-ZSM-5 [20]	Ammoniated Co/C [21]
Synthesis	Organometallic compound	Commercial zeolite	Ion-exchanged zeolite Y	Ion-exchanged H-ZSM-5	Doubly ammoniated, incipient wetness impregnation
Reaction Condition	30 bar, 30 ℃	62.7 bar, 150 ℃	(70 bar total, co-feed hexane) 0.91 bar, 130 ℃	80 bar, 120 ℃	31 bar, 150 ℃
Linear octene distribution	70-98%	0	31.4%	36.6%	65.3%

Aside from the catalysts listed in Table 1.1, ligand-modified molecular heterogeneous catalysts have also been studied for the production of straight-chain oligomers. For example, Cai *et al.* [22] have observed a 1-butene selectivity of 95% at 23% ethylene conversion with a $Ni^{I}L_2(O_s)_2$ catalyst where L = PEt_3. The particular ligand-

metal structure helped stabilize an intermediate metallacyclopentane for the formation of 1-butene. A Ni-exchanged MOF-based material denoted as Ni-MFU-4*l* and synthesized by Metzger *et al.* [23] combined a high activity (turnover frequency (TOF)=21,000 h^{-1}) with a high 1-butene selectivity (92.0 wt.%) upon activation with a co-catalyst.

In this thesis, efforts have been made to develop an efficient heterogeneous catalyst to convert light olefins into straight chain oligomers with a high selectivity. Several structure-performance relationships have been established to better understand the nature of the active site. Attempts to derive a reaction mechanism for different catalysts have been made which resulted in a comprehensive explanation of the observed product distribution.

In Chapter 2, zeolite catalysis and the reaction mechanism will be discussed based on the results obtained during 1-butene conversion. The fixed-bed reactor system together with the analytical instrumentation setup used in this thesis research will be briefly described. Product selectivity, catalyst stability and the cause of catalyst deactivation will be discussed during 1-butene conversion with H-ferrierite. Finally, a reaction mechanism based on carbocation chemistry will be derived that could explain the products observed from H-ferrierite and identified *via* 2D-GC/MS. Due to the catalysis of the Brønsted acid sites within zeolites, the production of highly branched oligomers with a well-controlled carbon chain length can be achieved.

In Chapter 3, 1-butene conversion with a carbon supported cobalt catalyst is demonstrated. A high selectivity (70%-85%) of linear octene was observed. The activity of the catalyst was found to be sensitive to its pretreatment temperature. The total oligomer yield was doubled with a decreasing pretreatment temperature from 270 ℃ to 230 ℃. Characterization results including powder X-ray diffraction (pXRD), X-ray absorption near edge structure (XANES), Raman spectroscopy and thermogravimetric analysis revealed a change in the cobalt oxidation state composition at different pretreatment temperatures. The cobalt appears to be more reduced at a high pretreatment temperature. It was proposed that the active site for oligomerization involves a Co(III) species. The reaction was temporarily described with a metallacyle mechanism.

Chapter 4 will aim to elucidate the reaction mechanism of carbon supported cobalt catalyst and to evaluate its performance in converting various types of light olefins. In this chapter, the conversion of ethylene, 1-butene, propylene, 1-hexene and 1-hexene/internal hexene mixture will be studied and compared in parallel. The linear

dimer distribution for each of the olefin feed is found to be above 50%. The catalyst suffered from different levels of deactivation during reaction. A preliminary Brunauer-Emmett-Teller (BET) measurement together with a TGA analysis of the spent catalyst samples revealed that the deactivation is most likely caused by olefin deposition and site blocking. To account for all the dimer isomer products – after the identification of the double bond position thanks to the 2D-GC technique – a Cossee type mechanism was found sufficient to describe the product selectivity with the carbon supported cobalt catalyst.

A bimetallic catalyst will be discussed in Chapter 5 which showed enhanced activity and stability for both ethylene and 1-butene oligomerization. The Cr – promoted cobalt on carbon catalyst demonstrated a high selectivity of 1-butene during ethylene conversion without the use of a co-catalyst. Characterization results of the bimetallic catalyst including XANES, EXAFS, pXRD, STEM and XPS have evidenced a charge transfer from Cr to Co. As a consequence, the cobalt appears more reduced in the bimetallic catalyst whereas the chromium appears more oxidized compared to their monometallic counterparts. The cobalt oxide particle size also appeared to be smaller in the bimetallic catalyst compared to the monometallic cobalt catalyst, which indicates a higher metal dispersion achieved upon addition of Cr.

CHAPTER 2 Zeolite-Based Catalysts for Alkene Oligomerization

Yong Tae Kim, Joseph P. Chada, Zhuoran Xu, Yomaira J. Pagan-Torres, Devon C. Rosenfeld, William L. Winniford, Eric Schmidt, George W. Huber. Low Temperature Oligomerization of 1-Butene with H-Ferrierite. *Journal of Catalysis,* 2015, 323, 33-44.

2.1 Introduction

Zeolites are aluminosilicate minerals built upon certain types of framework structures. The Brønsted and Lewis acid sites coexist within an unmodified zeolite. Zeolites are widely used solid acid catalysts in petrochemical industry due to their advantages such as being easily regenerable and stable over a wide temperature range, and being able to process feeds that contain mixtures of olefins. The shape selectivity feature of zeolites can be applied to control the product distribution within the pore channels [24-26]. For instance, it has been shown with density functional theory (DFT) that the pore confinement effects inside certain zeolites (ZSM-5 and ZSM-22) could increase the rate of ethylene dimerization [27]. By judicious catalyst and process parameter selection, a more desired selectivity can be achieved in the production of longer chain olefins from light alkenes.

A diversity of channel networks found within various zeolites could influence the product selectivity for alkene oligomerization differently. Varying the zeolite structure affects the diffusivity of both reactants and products for a chemical reaction. Additionally, the shape selectivity can also be achieved by constraining the formation of certain transition states. For example, medium-pore zeolites (constraint index between 1 and 12) having 10 member-ring channels are suitable frameworks for the selective production of C8-C12 olefins from butene oligomerization [28-30]. It was proposed that the side reactions such as cracking and hydride transfer were suppressed in the narrow 10 member-ring tubular channels within MCM-22 as compared to large pore zeolites such as US-Y and zeolite beta during 1-hexene oligomerization [31]. The volume of the zeolite cavity having the maximum included sphere diameter of approximately 7 Å is almost the same as that of the *n*-octyl carbocations [32], which could be suitable for butene dimerization. Ferrierite (FER), ZSM-57 and ZSM-23 have a volume of 124-165 $Å^3$, similar to that of *n*-octyl carbocations (180 $Å^3$). Martens and co-workers reported that ZSM-57 with a lobate pore structure has a high butene conversion combined with a high selectivity for dimers [28]. HFER was also demonstrated to have a relatively high C4 dimer selectivity during butene oligomerization next to ZSM-57. The synthesis of ZSM-57 with the general lab apparatus however, has not been successful. The best batch was obtained with a ZSM-57 phase purity of 86%.

The channel dimension within zeolite structure could also influence the product selectivity. It was suggested that 1-dimensional channel systems such as ZSM-22 and ZSM-23 are able to minimize the number of chain branching in the oligomer products [33]. Similar in pore size to ZSM-57 and ZSM-23, FER consists of 2-dimensional,

intersecting 8- and 10-member-ring channels. Yoon *et al*. reported that FER shows stable isobutene conversion with a higher selectivity for butene trimers as compared to ZSM-5 and mordenite [34]. Theses zeolite catalysts could potentially be further modified by controlling the location of the acid sites that could minimize the number of chain branching [33, 35].

Brønsted acid sites in zeolites are known to catalyze alkene oligomerization through a classical carbocation mechanism. At moderate temperature (473 – 573 K) and pressure (30 – 100 bar), the product distribution shifted to high molecular weight olefins (trimers, tetramers, etc.) [26, 32]. C4 olefin conversion over acid-based catalysts involves undesired side reactions that lead to the accumulation of heavy hydrocarbons (i.e. coke) in zeolite pores [36, 37].

The number of chain branches (NCB) in the oligomer products can be reduced by incorporating a transition metal cation within the zeolite framework. Franken *et al.* has reported a Co, Na, Ca –Y zeolite that was able to oligomerize 1-butene with high selectivity of butene dimers [19]. An NCB value of 1.1 was achieved at 403 K reaction temperature, as compared to around 2.0 NCB values obtained with narrow tubular pore zeolite such as ZSM-22. Another example is reported by Beltrame *et al.* on a Ni-ZSM-5 catalyst that was able to convert 1-butene into butene dimers with an NCB value of 1.89.

In this chapter, the synthesis of medium pore zeolites including MCM-22 and ZSM-23; and a large pore zeolite Mordenite will be briefly discussed. 1-Butene oligomerization was conducted with HFER catalyst, and the application of two-dimensional gas chromatography (GC × GC – MS) in the determination and quantification of the complex hydrocarbon compounds will be demonstrated. According to the analytical results of the product mixture, a reaction mechanism based on carbocation pathway was derived to describe the product selectivity observed with HFER during 1-butene oligomerization at low reaction temperature.

2.2 Experimental

2.1.1 Catalyst Synthesis

MCM-22 was synthesized based on published protocols [38]. For a typical synthesis, 0.92 g $NaAlO_2$ and 0.60 g NaOH pellets were dissolved in 124.2 g DI H_2O. To this solution, 7.61 g hexamethylenimine and 9.23 g SiO_2 were added under vigorous stirring and was maintained for 30 min. The resulting gels were then introduced into a 100 mL autoclave equipped with a Teflon liner and heated at 423 K for 7 days under 350 rpm magnetic stirring. The autoclave was then cooled naturally to room temperature, and the white solid was filtered then washed with DI H_2O following by drying at 353 K overnight. The sample was then calcined in stagnant air at 853 K for 3 h. Based on this method, 3.50 g of MCM-22 catalyst can be obtained from each batch.

ZSM-23 was synthesized according to the method reported by Ernst, *et al* [39]. For a typical synthesis, 0.14 g NaOH pellets and 7.28 g pyrrolidine were dissolved in 12.0 g DI H_2O. Afterwards, 4.20 g $Al(NO_3)_3 \cdot 9H_2O$ was added to the solution under stirring. 49.42 g of Ludox (Sigma Aldrich, 40 wt.% SiO_2 in H_2O) was then added to the mixture and stirred for a few minutes. The solution was charged into a 100 mL autoclave equipped with a Teflon linear and stirred at 453 K for 50 h. The autoclave was then cooled down naturally to room temperature. The white solid was filtered, washed with DI H_2O and dried at 353 K overnight. To obtain crystalline structure, the solid was calcined under stagnant air at 853 K for 3 h.

Mordenite was synthesized based on published protocols [40]. For a typical synthesis, 4.64 g NaOH pellets and 2.72 g $NaAlO_2$ powder were dissolved in 16.93 g DI H_2O. 24.00 g Ludox (Sigma Aldrich, 40 wt.% SiO_2 in H_2O) was then added to the solution under stirring. The mixture was stirred for 2 h under room temperature at 350 rpm, and then transferred into the 300 mL Parr reactor with a Teflon liner. The autoclave was kept at 443 K for 4 days without stirring. Afterwards, the autoclave was cooled down naturally to room temperature and the white solid was filtered and washed with DI H_2O. After drying at 353 K overnight, the solid was calcined in stagnant air at 853 K for 3 h.

The other commercially available zeolite catalysts were purchased from Zeolyst.

2.1.2 Catalyst Characterization

The crystalline structure of the as-synthesized zeolite was analyzed through powder x-ray diffraction. The measurements were taken between $2\theta = 5^o$ and $2\theta = 45^o$ with Rigaku Rapid II diffractometer with a Mo K_α source at 50 kV and 50 mA and a total exposure time of 20 min. The crystallite phase identification was performed with JADE 9 software. For a better comparison with literature, the patterns were then converted to Cu-XRD based on the momentum equation: $Q = \frac{4\pi sin\theta}{\lambda}$, where Q, θ and λ represent the momentum, diffraction angle and the x-ray wavelength.

Brunauer – Emmett – Teller (BET) and Langmuir surface areas were calculated from nitrogen adsorption data at 77 K obtained with an ASAP 2020 system (Micromeritics). Prior to the measurements, the sample was degassed under vacuum at 523 K for 12 h. The external surface area and micropore volume were calculated by the *t*-plot method.

Thermogravimetric analysis (TGA) was conducted with approximately 20 mg of each sample in the temperature range of 318 – 973 K with a heating rate of 10 K/min under a constant O_2 (or N_2) flow at 100 mL/min using TA instruments Q500 system. The samples were purged with O_2 (or N_2) at 318 K for 1 h prior to the analysis.

The amount of carbon formed on the used catalysts was determined with a total organic carbon (TOC) analyzer (Shimadzu TOC-5000A). During the TOC measurement, the temperature was held at 1173 K in flowing oxygen. The deposited carbon content was calculated by subtracting the amount of carbon on the fresh catalyst from that of the used catalyst.

2.1.3 Reactor and Analytical Setup

A schematic representation of the fixed-bed reactor system is described in Figure 2.1. 1-Butene oligomerization was carried out in a stainless-steel tubular flow reactor, in a down-flow arrangement, heated by a Lindberg/blue M (TF55030A-1; Thermo Scientific) furnace. The reactor was 30.5 cm in length with an inner diameter of 8.46 mm. A uniform temperature profile along the catalyst bed was achieved by inserting an aluminum heating block into the void space between the furnace and the tubular reactor. The temperature was monitored by a K-type thermocouple contacted directly into the aluminum block. For catalytic activity measurements, 0.5 – 4.0 g of catalyst without diluents was loaded into the reactor, and held in place by quartz wool plugs. Void spaces on both ends of the tubular

reactor were filled with glass beads (710 – 1180 μm, Aldrich). The catalyst was pelletized and sieved to obtain a uniform diameter of 420 – 841 μm. Before reaction, the pre-calcined catalyst was pretreated *in-situ* under flowing helium (150 mL/min) at 773 K for 2 h at a heating rate of 4 K/min to remove adsorbed water. After the pretreatment, the furnace was cooled to 373 K and the reactor system was pressurized to reaction pressure with a back pressure regulator. The gas phase olefin feed composed of 2% 1-butene in helium (Airgas) was fed into the reactor system with a mass flow controller (SLA 5850, Brook Instrument), and the liquid phase olefin feed was fed into the system through a high-pressure syringe pump (500D, Teledyne Isco) (99.9% 1-butene Matheson). Nitrogen (UHP, Airgas) was used as an internal standard. A chilled 75 mL stainless-steel gas-liquid separator was used to collect liquid products at the bottom of the reactor at 268 K and reaction pressure. A 50 mL glass pressure tube was installed after the back-pressure regulator to condense any residual liquid products at 0.1 MPa and 268 K. Online gas chromatography (GC; Shimadzu, 2014) was used to analyze the reactor gas effluent. N_2 and CH_4 in the gas phase were analyzed with a thermal conductivity detector (TCD) with a combination of Hayesep R (Supelco, Catalog No. 12085-U) and Shincarbon (Restek, Catalog No. 19808) packed column. The injection port and the detector were held at 473 K and 523 K, respectively. The column pressure was 300 kPa with helium as carrier gas. Hydrocarbons in the range of C1 to C6 in the gas phase were analyzed with a flame ionization detector (FID) (RT®-Alumina BOND/Na_2SO_4, Restek, Catalog No. 19756). Both the injection port and the detector were held at 473 K. The column flow rate was 7.91 mL/min using helium as carrier gas. The following GC oven temperature program was employed: The temperature was held at 318 K for 1 min, ramped to 453 K at 10 K/min, and held at 453 K for 41 min. The liquid product collected in the gas-liquid separators was drained periodically into a sampling vial. The sampling vial was precooled to 194.5 K and preloaded with 0.5 wt.% heptane in hexane solution to suppress volatilization of the liquid products. The liquid products were analyzed with comprehensive two-dimensional gas chromatography-mass spectroscopy (GC × GC – MS) with both an FID (Agilent, 7890B) and a mass selective detector (MSD; Agilent, 5977A). A flow modulator (CFP; Agilent, G3487A) was installed to split the flow into two columns. Two capillary columns, DB-17 (Agilent, Catalog No. 121-1723) and CP-Sil 5 CB (Agilent, Catalog No. CP7700), were coupled in series with the CFP. The first and second dimension column flow rates were 0.7 mL/min and 25 mL/min, respectively, and both using H_2 as carrier gas. For all experiments, both the first and second dimensions were operated in constant flow mode. For each analysis, 0.5 - 1.0 μL of liquid sample was injected. The injection port and the detector were held at 473 K and 523 K, respectively. The following GC × GC oven

temperature program was used: The temperature was held at 303 K for 1 min, ramped to 523 K at 5 K/min, and held at 523 K for 5 min. GC × GC processing was done with GC – Image 2.3b data visualization software (Zoex Corporation), as shown in Figure 2.2. All of the detected peaks were quantified using GC-FID. Unknown species were identified by their mass spectra and retention indices.

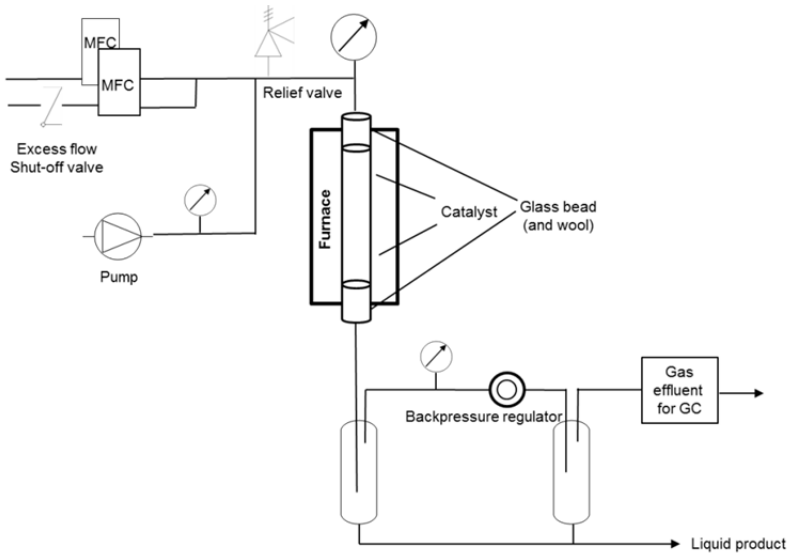

Figure 2.1 Schematic description of the down-flow fixed-bed reactor system.

Conversion was calculated as moles of feedstock reacted per moles of feedstock fed into the system. The butene isomers (*trans*-2-butene and *cis*-2-butene) were grouped together and considered as the non-converted feed based on total C4 olefin conversion. Product selectivity was calculated as carbon moles of product produced per carbon moles of feedstock reacted within the system. Yield of the products was calculated by carbon moles of product divided by carbon moles of feedstock fed into the system. Product distribution was defined as the ratio of carbon moles of a specific product divided by the total carbon moles of corresponding categories (olefin, paraffin, aromatic/naphthalene, cycloalkane, etc.).

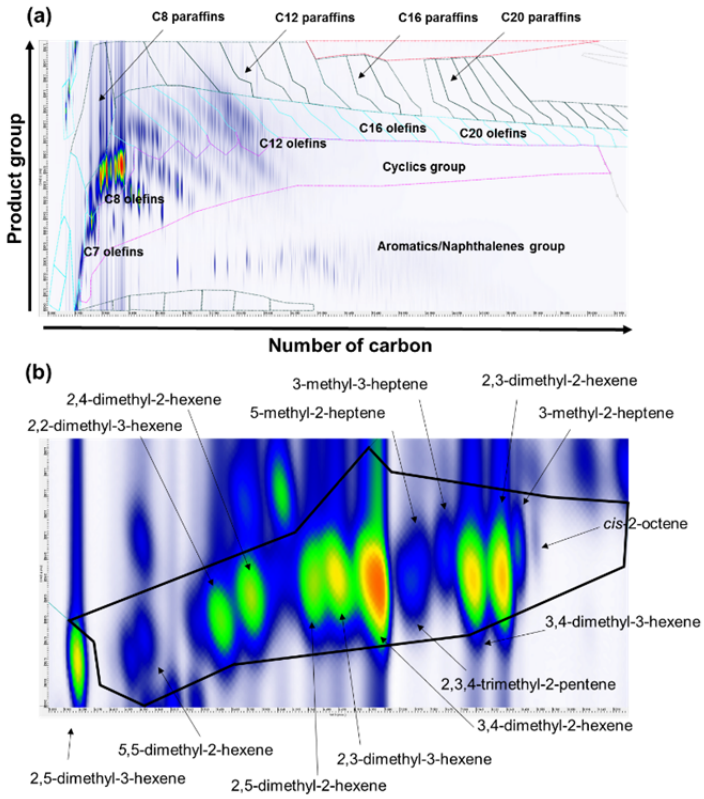

Figure 2.2 Separation and identification of (a) entire products and (b) C8 olefins with 2-dimensional gas chromatography (2D-GC).

2.2 Results and Discussion

2.2.1 Catalyst Characterization

The XRD pattern of the as-synthesized and calcined MCM-22 is shown in Figure 2.3. The measured XRD profile matches perfectly with the standard, indicating the successful synthesis of MCM-22 structure with high phase purity.

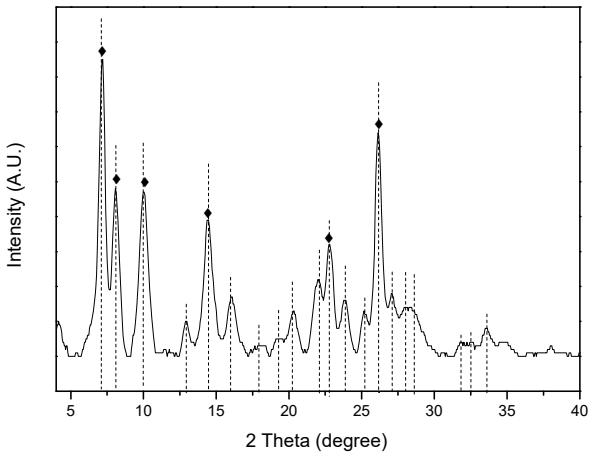

Figure 2.3 Converted (Cu)-XRD pattern for as-synthesized MCM-22. The dotted lines indicate the XRD reference peaks for a standard MCM-22 crystalline structure. The peaks labelled with a diamond symbol represent the matched peak with the highest intensities.

The XRD patterns of two batches of as-synthesized and calcined ZSM-23 are shown in Figure 2.4. The XRD profiles of both samples match the standard reference very well, indicating the successful and reproducible synthesis of ZSM-23 zeolite structure.

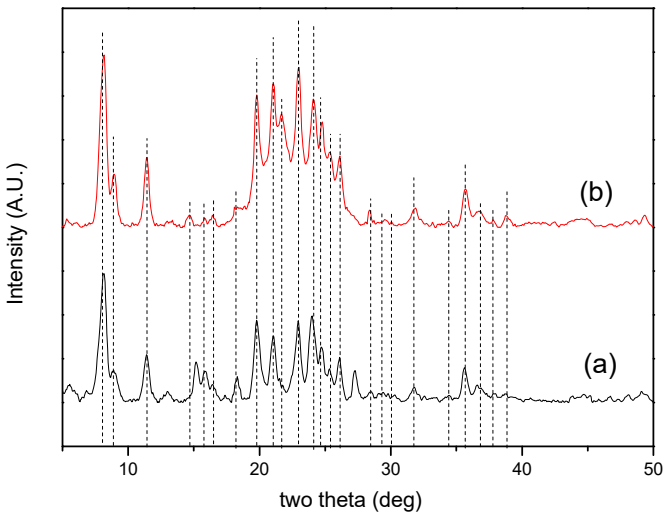

Figure 2.4 Converted (Cu) – XRD patterns for two batches of calcined ZSM-23 synthesized on (a) 9/5/2013 and (b) 9/13/2013. Both were synthesized following the same procedures described in the experimental section. The dotted lines represent the XRD peak for a standard ZSM-23 structure.

The XRD pattern of the as-synthesized mordenite as compared to that obtained from the commercial mordenite (Zeolyst) is depicted in Figure 2.5. The XRD profile of the as-synthesized mordenite matches that of the commercial sample very well, indicating the successful synthesis of mordenite based on the previously described procedure.

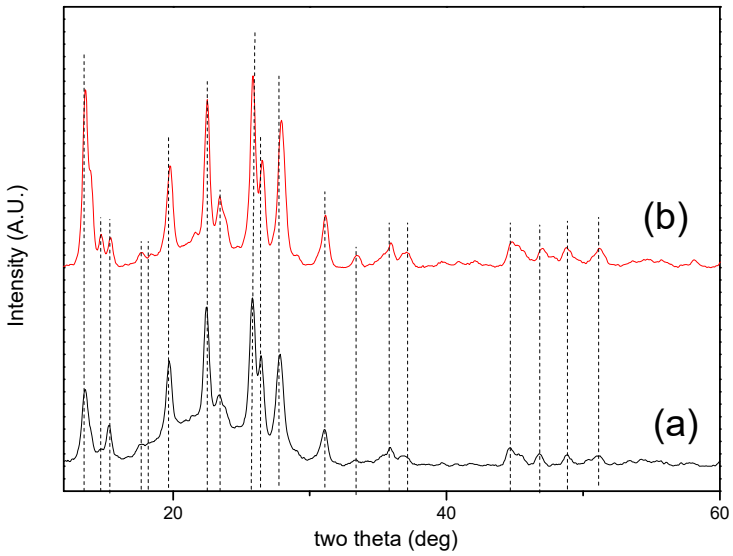

Figure 2.5 Converted (Cu) – XRD of (a) commercial mordenite CBV21A and (b) as-synthesized mordenite. The dotted lines are plotted to guide the eye.

2.2.2 1-Butene Oligomerization with H-ferrierite

The effect of reaction temperature on the gas-phase oligomerization of 1-butene was studied at 6.9 bar over H-ferrierite. The C4 olefin conversion (the conversion of linear C4 olefins) increased with reaction temperature (Figure 2.6). No butene isomers or other products were detected during the initial two hours of reaction at 373 K. Control experiments to determine system residence time at relevant reaction conditions show product detection in less than 20 min TOS. This transient period was associated with the time to fill the zeolite micropores. After the transient period, the C4 olefin conversion stabilized and then slowly decreased with time-on-stream.

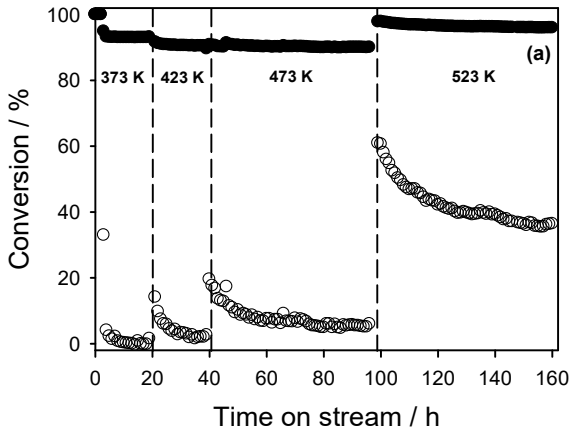

Figure 2.6 1-Butene conversion (●) and C4 olefin conversion (○) as a function of time-on-stream and reaction temperature for oligomerization of 1-butene at low 1-butene partial pressure. Reaction condition: 2.0 mol% 1-butene in helium, $WHSV_{1\text{-butene}} = 0.03\ h^{-1}$; $P_{total} = 6.9$ bar, $P_{1\text{-butene}} = 0.14$ bar.

Table 2.1 shows the butene distribution with respect to reaction temperatures. As reaction temperature increased, the 2-butene selectivity decreased, whereas the isobutene selectivity increased. 1-Butene undergoes isomerization to produce *cis*-2-butene and *trans*-2-butene [41]. Thermodynamic equilibrium between *cis*-2-butene, *trans*-2-butene and 1-butene was rapidly reached at all temperatures studied. This is consistent with the work of Sels and co-workers [42]. *Trans*-2-butene then undergoes skeletal isomerization to produce isobutene [41]. The ratio of *trans*-2-butene to *cis*-2-butene decreased from 2.2 to 1.7 as reaction temperature increased. Isobutene production, which involves skeletal alteration, was not in equilibrium with *trans*-2-butene. This is consistent with the work of Lemos *et al* [43].

The product selectivity was strongly dependent on reaction temperature as shown in Table 2.1. The carbon balances were between 96.9-99.2%. The gaseous products were C2-C8 olefins and C1-C5 paraffins along with butene isomers. A small amount of liquid products which included C5-C19 olefins, C7-C20 paraffins, aromatics, and cycloalkanes was collected at temperatures above 473 K. A trace amount of C2 olefin was detected with a selectivity of less than 0.5%. Most of the olefins (75.6-90.0%) were C8 olefins at temperatures below 423 K. No C9-C20 olefins at temperatures below 423 K were detected. The C8 olefin selectivity decreased with increasing reaction temperature, while the C3 and C5-C7 olefin selectivity increased.

Table 2.1 Effect of reaction temperature on 1-butene oligomerization at low pressure (6.9 bar). Reaction conditions: 2.0 mol% 1-butene in helium, $WHSV_{1\text{-butene}}$ = 0.03 h^{-1}; P_{total} = 6.9 bar, $P_{1\text{-butene}}$ = 0.14 bar [a.b].

Reaction temperature (K)	373	423	473	523
Reaction time (h)	19	39	95	160
C4 olefin conversion (%)	1.5	2.6	5.1	36.4
Apparent deactivation rate constant (k_d)	3.77	0.70	0.38	0.15
Butene distribution (%)				
1-butene	7.3	11.1	11.0	6.6
cis-2-butene	29.1	30.5	28.8	15.0
trans-2-butene	63.5	55.9	50.8	25.3
iso-butene	0.1	2.5	9.4	53.0
Olefin selectivity (%)	62.1	67.0	68.2	55.4
Olefin distribution (%)				
C2-C3	0	0	2.0	11.6
C5-C7	10.0	7.6	7.6	36.5
C8	90.0	92.4	74.9	39.5
C9-C11	0	0	4.6	8.0
C12	0	0	7.1	3.7
C13-C15	0	0	3.1	0.8
C16	0	0	0.5	0
C17-C19	0	0	0.2	0
C20	0	0	0	0
Paraffin selectivity (%)	34.3	32.6	24.2	19.5
Paraffin distribution (%)				
C2-C4	100	100	78.2	51.3
C5-C7	0	0	2.8	2.0
C8	0	0	2.8	15.7
C9-C11	0	0	5.1	15.6
C12	0	0	2.7	5.1
C13-C15	0	0	5.8	9.7
C16	0	0	1.0	0.5
C17-C19	0	0	1.6	0
C20	0	0	0.1	0
Aromatic selectivity (%)	0	0	3.1	2.0
Cycloalkane selectivity (%)	0	0	5.1	6.2
Carbon balance in gas phase (%)	98.4	99.2	100.4	92.8

[a] Product distribution (%) = (the carbon moles in the product)/(the sum of carbon moles in the product group) × 100 %.
[b] Product selectivity (%) = (the carbon moles in the product)/(the carbon moles in the converted C4 olefins) × 100 %.

The only paraffin products observed at temperatures below 423 K were C4 products. Boronat et al. found that hydride transfer of olefin feedstock is a primary reaction in the presence of Brønsted acid sites [44]. The C4 paraffin selectivity decreased 2.2 times with increased temperature from 473 K to 523 K. The hydrogen transfer of

oligomerization products led to an increase of the C8-C20 paraffin, aromatic, and cycloalkane selectivity with increasing reaction temperature.

The deactivation rate constant was calculated according to Levenspiel's model [45, 46] for independent deactivation assuming a second-order deactivation via the power-law equation as shown by Equation 2.1. Second-order deactivation was found to be the best fit of our data for all conditions tested. In Equation 2.1, r_d represents deactivation rate, a is the fractional remaining activity at time t, and k_d is the deactivation rate constant. The deactivation rate constant decreased 25 times as the reaction temperature increased from 373 K to 523 K, as shown in Table 2.1. This is probably because higher temperatures are needed to desorb the butene oligomer products from the catalysts pores.

Equation 2.1 $-r_d = -\mathrm{d}a/\mathrm{d}t = k_d a^2$

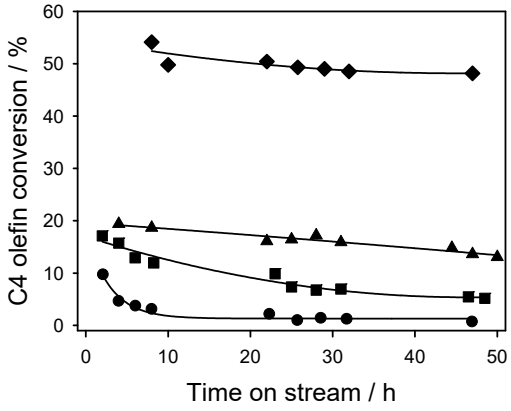

Figure 2.7 C4 olefin conversion as a function of time on stream: effect of 1-butene partial pressure: 14.2 bar (●), 32.2 bar (■), 42.9 bar (▲), 62.7 bar (◆). Reaction condition: WHSV1-butene = 3.17 h-1; Ptotal = 62.7 bar, T = 423 K.

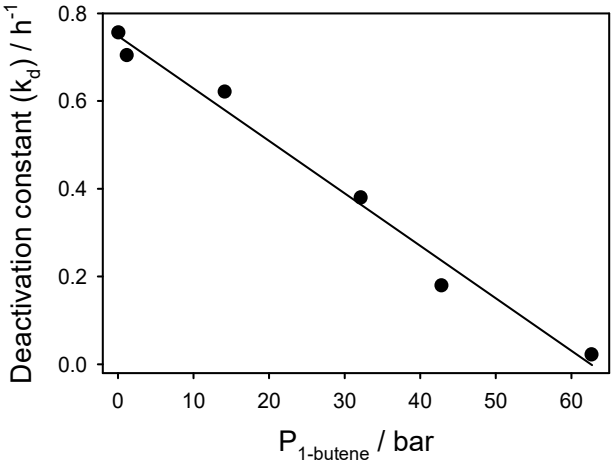

Figure 2.8 Apparent deactivation rate constants (k_d) for C4 olefin oligomerization as a function of 1-butene partial pressure. Reaction condition: Ptotal = 62.7 bar, T = 423 K.

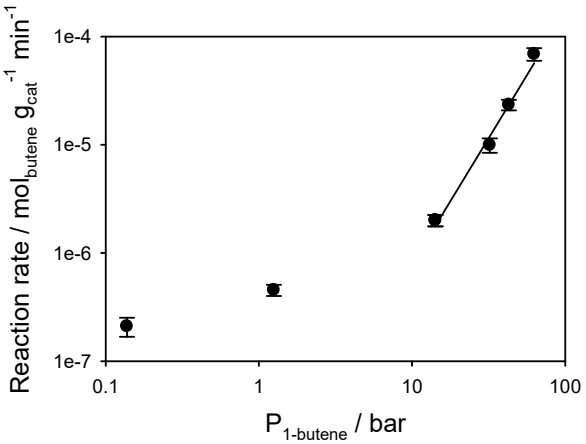

Figure 2.9 C4 olefin reaction rate as a function of 1-butene partial pressure. Reaction condition: Ptotal = 62.7 bar, T = 423 K.

The effect of 1-butene partial pressure at 423 K is shown in Figure 2.7-2.9. The inlet partial pressure of 1-butene was varied by suing helium as a balance. The total pressure was held constant at 62.7 bar. The critical temperature and pressure of 1-butene are 419.6 K and 40.2 bar [47]. Thus, we are above the critical temperature and above the critical pressure at some of the conditions in Figure 2.7. The C4 olefin conversion increased from 1.2 to 49.2 with increasing 1-butne partial pressure from 14.2 to 62.7 bar. At 14.2 bar, the catalyst deactivated rapidly during the initial 10 h on stream. The rate of deactivation decreased with increasing 1-butene partial pressure.

The deactivation rate constant was inversely proportional to 1-butene (and thus total C4) partial pressure as shown in Figure 2.8. For example, assuming second-order deactivation, the deactivation rate constant decreased 36.3 times (from 0.75 h^{-1} to 0.02 h^{-1}) as the 1-butene partial pressure increased from 0.14 bar to 62.7 bar. Decreasing the temperature from 423 K to 373 K, where 1-butene is in the liquid phase, caused a 3.8-fold increase in the rate of deactivation, as shown in Figure 2.10. These results show that the transition from the butene subcritical to supercritical state either removes coke or inhibits its formation. These results are consistent with those of Fan *et al*. [48] who observed that 90% of the initial activity of a spent H-ZSM-5 catalyst that had been used for ethylene oligomerization at 573 K and 55 bar was restored by treatment in supercritical n-pentane for 3 h.

The rate of butene conversion was second order with respect to 1-butene partial pressure in the near-critical region at 423 K as shown in Figure 2.9. This is consistent with the work of Gee and Williams who reported that the dimerization of linear olefins in the range of C8 to C18 was second order in olefin [49]. For butene, in the partial pressure of 0.14-1.25 bar the catalyst deactivation made it difficult to determine the exact reaction order in butene. We can make a rough estimation of the reaction order to be approximately 0.4 with respect to butene (from the data in Figure 2.9) assuming that we have made accurate measurements of catalyst activity with deactivation.

One way of diminishing the deactivation of the zeolite catalyst is to operate at a relatively low temperature (423 K) and at near-supercritical (i.e. conditions slightly above or below the critical point) butene conditions. Under these conditions, butene has the appropriate transport properties to effectively extract heavy hydrocarbons from the catalyst pores [50, 51].

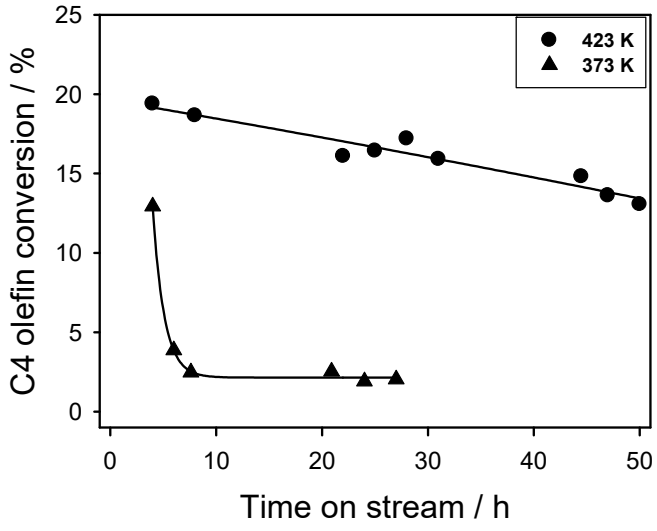

Figure 2.10 C4 olefin conversion as a function of time-on-stream and temperature. Reaction condition: $P_{1\text{-butene}}$=42.9 bar, $WHSV_{1\text{-butene}}$=0.03 h-1; P_{total}=62.7 bar.

The effect of weight hourly space velocity (WHSV) on 1-butene oligomerization at 423 K and 62.7 bar (supercritical conditions) is shown in Figure 2.11, Table 2.2 and Table 2.3. At least three samples were collected at each WHSV at regular intervals to ensure steady state was reached. The C4 olefin conversion increased with decreasing space velocity. As the WHSV increased from 0.18 to 3.17 h^{-1}, the olefin selectivity increased from 76.8% to 92.4%. An olefin selectivity >90% was maintained at WHSV of 9.5 and 49.7 h^{-1}. The paraffin selectivity markedly decreased from 12.6% to 4.7% with increasing WHSV from 0.18 to 1.06 h^{-1} and continued to decrease with increasing WHSV until a minimum of 0.7% was reached at 49.7 h^{-1}. Only trance amount of aromatics and cycloalkanes were detected at a space velocity of 0.18 h^{-1}, but their selectivities increased to 2.4% and 1.7% as the WHSV increased to 50 h^{-1}.

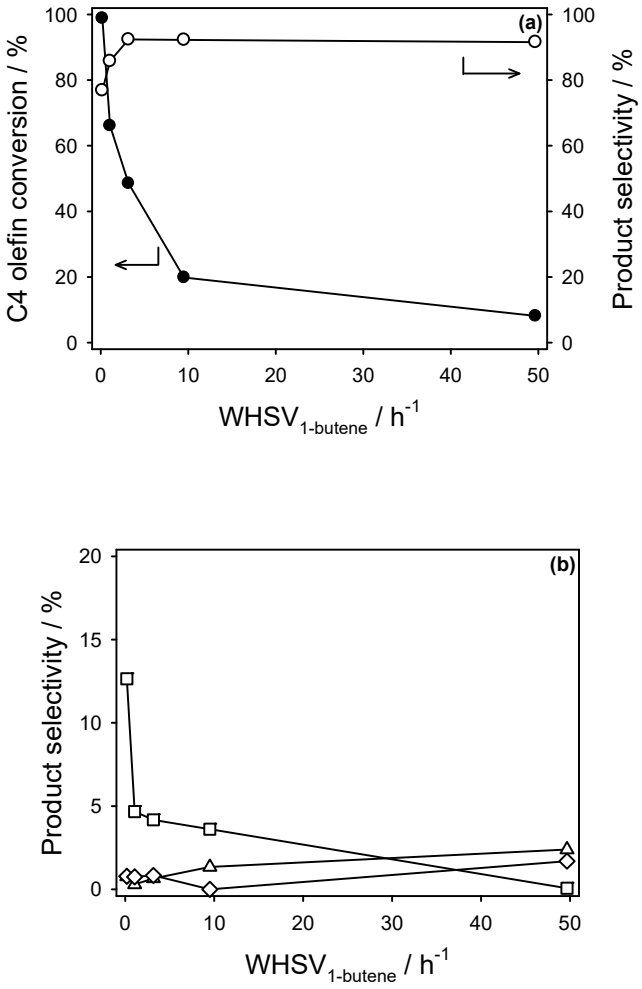

Figure 2.11 (a) C4 olefin conversion (●) and olefin selectivity (○) as a function of weight hourly space velocity (WHSV). (b) Paraffins (□), aromatics (△), and cycloalkanes selectivity (◇) as a function of WHSV. Reaction condition: Ptotal = 62.7 bar, P1-butene = 62.7 bar, T = 423 K.

The product selectivity as a function of WHSV is shown Table 2.1. Only trace amounts of isobutene were detected at 98.9% C4 olefin conversion. We did not detect C2-C4 olefins or C2-C4 paraffins under these conditions. The C5-C7 olefin selectivity was 1.1-2.0%, indicating that cracking of C8 olefins is minimized under supercritical condition. At a space velocity of 49.7 h^{-1}, C8 olefins were the predominant olefin product, accounting for 88.8% of total olefin products. As space velocity decreased from 49.7 h^{-1} to 0.18 h^{-1}, the C8 olefin selectivity decreased from 88.8% to 15.1%, whereas the C12, C16, and C20 olefin selectivity increased from 9.0% to 59.6%. Similarly, the selectivity toward C9-C11, C13-C15, and C17-C19 olefins increased from 0.3% to 24.1% with decreasing WHSV.

Similar patterns were also observed with C5-C15 paraffins. These results reveal a partial and increasing contribution .

Table 2.2 1-Butene oligomerization at supercritical 1-butene conditions as a function of weight hourly space velocity (WHSV) (Reaction condition: Ptotal = 62.7 bar, P1-butene = 62.7 bar, T = 423 K)[a,b]

WHSV (h^{-1})	0.18	1.06	3.17	9.51	49.7
Reaction time (h)	51	50	47	4	1
C4 olefin conversion (%)	98.9	66.1	48.5	19.3	8.1
Butene distribution (%)					
1-butene	11.7	12.9	12.8	13.3	15.5
cis-2-butene	27.2	28.5	28.4	28.4	28.2
trans-2-butene	55.9	58.5	58.8	58.3	56.2
iso-butene	5.1	0	0	0	0
Olefin selectivity (%)	76.8	85.8	92.4	92.3	91.6
Olefin distribution (%)					
C2-C3	0.0	0.0	0.0	0.0	0.0
C5-C7	1.1	1.8	2.0	1.6	1.9
C8	15.1	59.4	69.2	82.6	88.8
C9-C11	7.1	6.6	4.9	1.9	0.3
C12	21.8	20.7	17.7	12.0	8.7
C13-C15	9.2	2.3	1.0	0.1	0.0
C16	20.8	5.7	3.8	1.6	0.0
C17-C19	7.8	1.4	0.6	0.1	0.0
C20	17.0	2.0	0.8	0.1	0.3
Paraffin selectivity (%)	12.6	4.7	4.2	3.6	0.1
Paraffin distribution (%)					
C2-C4	0.0	0.0	0.0	0.0	0.0
C5-C7	6.7	4.5	5.6	4.7	0.0
C8	53.8	76.0	73.3	60.7	100
C9-C11	31.3	16.7	17.4	29.3	0.0
C12	4.6	1.5	2.6	4.9	0.0
C13-C15	3.6	1.3	1.2	0.3	0.0
C16	0.0	0.0	0.0	0.0	0.0
C17-C19	0.0	0.0	0.0	0.0	0.0
C20	0.0	0.0	0.0	0.0	0.0
Aromatic selectivity (%)	0.8	0.3	0.7	1.3	2.4
Cycloalkane selectivity (%)	0.8	0.8	0.8	0	1.7
Carbon balance (%)	91.2	94.4	99.1	99.5	99.7

[a] Product distribution (%) = (the carbon moles in the product)/(the sum of carbon moles in the product group) × 100 %.
[b] Product selectivity (%) = (the carbon moles in the product)/(the carbon moles in the converted C4 olefins) × 100 %.

of selective oligomerization-cracking-realkylation by H-FER with decreasing WHSV. Iglesia reported that high molecular weight olefins are susceptible to cracking reactions than light olefins [52, 53].

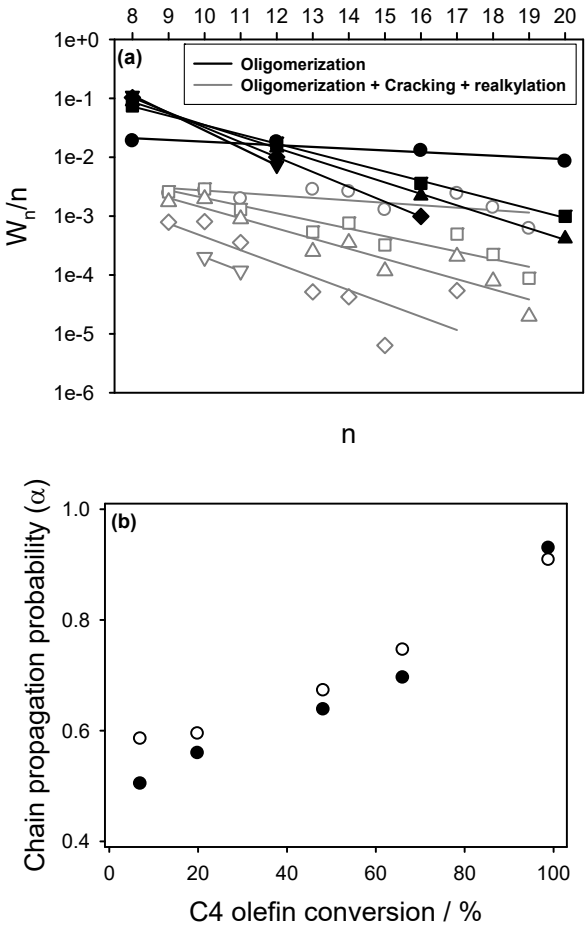

Figure 2.12 (a) Olefin molecular weight distributions at a WHSV1-butene of 0.18 h^{-1} (●, ○), 1.06 h^{-1} (■, □), 3.17 h^{-1} (▲, △), 9.51 h^{-1} (◆, ◇), and 49.7 h^{-1} (▼, ▽) for oligomerization products (C8, C12, C16, and C20) (open) and oligomerization-cracking-realkylation products (C9-C11, C13-C15, C17-C19) (filled). (b) chain propagation probability (α) for oligomerization products (C8, C12, C16, and C20) (●) and oligomerization-cracking-realkylation products (C9-C11, C13-C15, and C17-C19) (○) as a function of C4 olefin conversion. Reaction condition: P1-butene = 62.7 bar, Ptotal = 62.7 bar, T = 423 K.

Table 2.3 Distribution of octenes at supercritical 1-butene conditions as a function of WHSV. (Reaction condition: P_{total} = 62.7 bar, $P_{1\text{-butene}}$ = 62.7 bar, T = 423 K)[a]

WHSV (h^{-1})	0.18	1.06	3.17	9.51	49.7
C8 olefin distribution (%)					
2-methyl-1-heptene	0.0	0.0	0.3	0.0	1.9
2-methyl-3-heptene	0.9	0.0	0.5	0.8	1.4
3-methyl-2-heptene	0.9	0.6	0.9	1.6	2.8
3-methyl-3-heptene	0.9	0.8	0.8	1.0	2.0
5-methyl-2-heptene	0.0	0.0	0.2	1.0	0.0
2,2-dimethyl-3-hexene	3.5	4.9	3.8	1.8	1.1
2,3-dimethyl-2-hexene	19.3	13.7	11.9	10.5	10.5
2,3-dimethyl-3-hexene	7.0	12.7	13.9	13.8	12.5
2,4-dimethyl-2-hexene	19.3	6.7	5.1	5.4	5.3
2,5-dimethyl-2-hexene	19.3	7.5	6.4	5.5	4.6
2,5-dimethyl-3-hexene	0.9	0.4	0.2	0.1	0.0
3,4-dimethyl-2-hexene	14.9	37.3	41.2	43.7	42.8
3,4-dimethy-3-hexene	7.0	13.3	13.6	14.4	15.1
5,5-dimethyl-2-hexene	3.5	0.6	0.2	0.0	0.0
2,4,4-trimethyl-1-pentene	0.0	0.0	0.5	0.0	0.1
2,3,4-trimethyl-2-pentene	2.6	1.6	0.6	0.3	0.0

[a] Product distribution (%) = (the carbon moles in the product)/(the sum of carbon moles in the product group) × 100 %.

Figure 2.12 shows a semilog plot that represents the oligomerization and oligomerization –cracking-realkylation products in Table 2.2. These products followed the Schulz-Flory chain growth model, as described in Equation 2.2, where n is the hydrocarbon chain length, W_n is the weight fraction of hydrocarbon products of length n, and α is the chain growth probability. In this study, we have applied the Schulz-Flory chain growth model to the observed olefin product distribution. Schulz-Flory distribution is commonly employed to model polymer and polyolefin chain distribution [54-56]. The oligomerization (C8, C12, C16, C20 olefins) and oligomerization-cracking-realkylation (C9-C11, C13-C15, and C17-C19 olefins) products also followed the Schulz-Flory model as shown in Figure 2.12. Oligomerization-cracking products such as C5-C7 olefins did not follow Schulz-Flory distribution and are not reported. The chain growth probability increased from 0.50 to 0.93 with increasing C4 olefin conversion from 8.1% to 98.9%.

Equation 2.2 $\frac{W_n}{n} = \alpha^{n-1}(1-\alpha)^2$

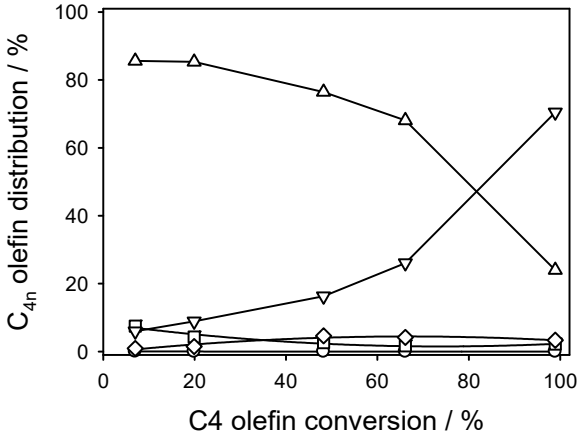

Figure 2.13 C_{4n} (n=2-6) olefin distribution of linear- (○), mono-branched- (□), di-branched- (△), tri-branched- (◇), and greater than tri-branched-olefins (▽) a function of C4 olefin conversion. Reaction condition: P_{total} = 62.7 bar, $P_{1\text{-butene}}$ = 62.7 bar, T = 423 K.

The degree of branching in the olefin products was a function of butene conversion as shown in Figure 2.13. Only trace amounts of straight-chain alkenes were produces independent of butene conversion. Over 80% of the oligomer products were di-branched olefins at conversions less than 20%. The degree of branching in the products increased as the overall conversion increased. We did not individually identify each of the C12-C20 olefin isomers through GC×GC – MS due to lack of standard chemicals for those olefins. As the di-branched olefin selectivity increased, the selectivity to highly branched olefins also increased. The other branched olefins include above trimethyl- and methyl-ethyl-species. The mono-branched olefin selectivity decreased while higher branched olefin selectivity increased with increasing C4 olefin conversion. The direct correlation between olefin branching and C4 olefin conversion is consistent with a carbon-based mechanism of oligomerization.

The distribution of C8 olefin isomers is summarized in Table 2.3. The C8 olefin products include 91.9-94.7% dimethyl hexenes at various C4 olefin conversions. The methyl-heptene selectivity decreased from 8.1% to 2.7%, while the trimethyl-pentene selectivity increased from 0.1% to 2.6% with increasing C4 olefin conversion. A trace of linear octenes was detected with a selectivity of less than 0.1%. Near equilibrium of the C8 double bond isomers was achieved.

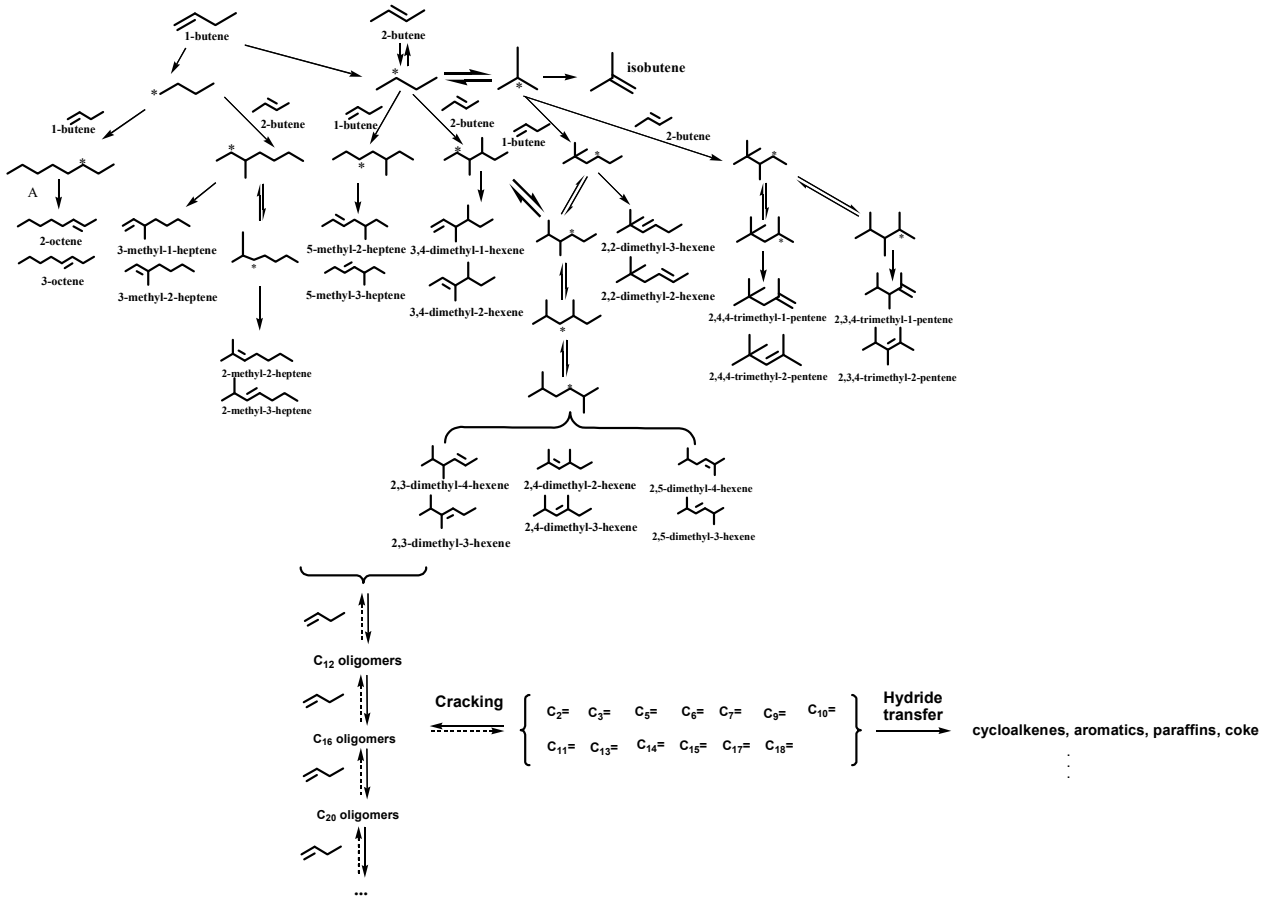

Figure 2.14 Major reaction pathway for 1-butene oligomerization with H-FER.

The major reaction pathway for 1-butene oligomerization is depicted in Figure 2.14. This pathway involves acid-catalyzed reactions: (1) oligomerization, (2) (skeletal) isomerization, (3) hydrogen transfer, (4) cracking, and (5) alkylation [57]. According to the assumption that the heats of adsorption for olefin adsorption in zeolites vary linearly with carbon number [58], the products with larger carbon numbers are more likely to be re-adsorbed and undergo secondary reaction such as hydrogen transfer, cracking, and isomerization [51]. 1-Butene underwent double bond and skeletal isomerization to from trans- or cis-2-butene and isobutene, respectively. Based on Marovnikov's rule [59], reactions involving a primary carbocation were unlikely to take place; thus, the amount of linear octenes and 3-methyl-heptenes were minimal. Most of the products were formed through secondary carbocations. At a low C4 olefin conversion, 3,4-dimethyl hexenes and 2,3-dimethyl hexenes were predominant products in the mixture of C8 olefin products. The dimerization products then underwent further methyl and hydride shift, thus forming additional C8 isomers, which were in equilibrium at 423 K. As C4 olefin conversion increased, the 3,4-dimethyl hexene selectivity decreased, whereas the selectivity toward 2,4-dimethyl hexenes and 2,5-dimethyl hexenes

increased. The 2,3 dimethyl hexene selectivity increased a little with C4 olefin conversions. The selectivity data illustrate that the formation of 2,3-dimethyl hexenes is favored over the 2,4 and 2,5 dimethyl hexene isomers during a skeletal alteration of 3,4-dimethyl hexenes, even at low C4 butene conversions. Most of 2,2-dimethyl hexenes were probably formed from the initial skeletal isomerization of 2-butene to isobutene followed by addition of 1-butene isobutene since the equilibrium composition of those compounds was significantly low for 2-butene conversion. The combination of isobutene and 2-butene yielded 2,4,4-trimethyl-pentene and 2,3,4-trimethyl-pentene which were observed in low selectivities.

2.3 Conclusions

MCM-22, ZSM-23 and Mordenite can be synthesized following the published protocols based on hydrothermal method. The XRD patterns of the as-synthesized samples confirmed the purity of the phases. 1-Butene oligomerization was conducted over H-FER to investigate the effect of reaction temperature and 1-butene partial pressure at low temperature ranges (373 - 523 K). 1-Butene was in equilibrium with *trans*-and *cis*-2-butene under all reaction conditions tested. During the reaction, the catalyst deactivated due to the deposition of heavier hydrocarbons inside of the zeolite micropores. The deactivation rate was a function of temperature and 1-butene partial pressure. The deactivation rate constant decreased 25 times with increasing temperature (373 – 523 K) at low 1-butene partial pressure (0.14 bar). The C8 olefin selectivity was maximized at low temperatures (below 473 K). At temperatures above 473 K, cracking and hydride transfer reactions occurred leading to an increase in the selectivities to paraffins, aromatics, and non-C4 multiple olefins.

The catalytic activity was proportional to 1-butene partial pressure with an apparent reaction order of 2.1 ∓ 0.1 at pressures from 14.2 – 62.7 bar. The deactivation rate constant decreased 36.3 times with increasing 1-butene partial pressure (0.14 – 62.7 bar). During the reaction at supercritical 1-butene conditions (62.7 bar and 423 K), the products followed a Schulz – Flory chain growth distribution. The chain growth probability decreased with increasing C4 olefin conversion. A reaction pathway was derived to describe the products observed from 1-butene oligomerization over H-FER. Butenes initially underwent dimerization to produce 3,4-dimethyl-2-hexene and 3-methyl-heptene. Then, both C8 olefins underwent a series of skeletal isomerizations (methyl shifting). The skeletal isomerization products were in equilibrium at 423 K. The isomerization of C=C double bonds was in equilibrium for

C4 olefins and C8 olefins. Most of the heavier olefins (above C12) were highly branched (above trimethyl- and methyl-ethyl-species).

Although the shape selectivity induced by various unmodified zeolite frameworks is capable of achieving a precise control of the oligomer carbon chain length, they are not sufficient in producing linear oligomers from light olefins with high selectivity. Modified zeolite frameworks, such as by the method of surface poisoning [60, 61] and ion exchange [19] could achieve a noticeable amount of linear oligomer selectivities, frequently around 30%. A high selectivity of straight chain oligomers however, could be achieved based on transition metal catalyzed reaction as discussed in the chapter that follows.

CHAPTER 3 CoO_X/N-C Catalysts: Production of Linear Octenes

Zhuoran Xu, Joseph P. Chada, Dongting Zhao, Carlos A. Carrero, Yong Tae Kim, Devon C. Rosenfeld, Jessica L. Rogers, Steven J. Rozeveld, Ive Hermans, George W. Huber. Production of Linear Octenes from Oligomerization of 1-Butene over Carbon-Supported Cobalt Catalysts. *ACS Catalysis*, 2016, 6, 3815-3825.

3.1 Introduction

The studies of zeolite catalyzed light olefin oligomerization in Chapter 1 have ruled out the likelihood of using a Brønsted acid-containing catalyst to obtain a high selectivity of straight-chain oligomers. For Chapter 3 and the chapters that follow, we will focus on some supported transition metal catalysts for selective production of straight-chain oligomers from light alkenes.

The industrial production of linear alpha olefins is from the oligomerization of ethylene through organometallic catalysis, such as the Shell Higher Olefin Process (SHOP) (Ni complex) and the catalytic Ziegler process (triethyl-aluminum) [8, 62]. Complexes of Co, Fe and Cr are reported to catalyze α-olefin oligomerization yielding a distribution of linear alpha olefins that range from C4 to polyethylene from a highly purified feed stream [13, 63, 64]. It's important to state that these catalysts produce mixtures that follow the Schultz-Flory distribution. Although several other systems have been studied for alpha olefin oligomerization, they tend to produce branched products. Solid heterogeneous catalysts have several advantages over homogeneous catalysts including: recyclability, the ability to handle olefins containing more impurities, the ability to better control the olefin chain growth, and no co-catalyst is required for activation.

Solid acid catalysts, including zeolites and solid phosphoric acids, have been investigated for olefin oligomerization [18, 26, 65-67]. These catalysts primarily produce branched olefin oligomers along with paraffins and cycloalkenes. Some researchers have observed low selectivities of linear octenes (31-37%) from butene oligomerization over Co, Na, Ca-Y and HNaNi-ZSM-5 [20, 68] at a conversion between 70-90% and 65%, respectively. However, the production of olefins over Brønsted acid catalysts primarily forms branched species due to the higher stability of the internal (secondary and tertiary) carbocation *vs*. the primary carbocation required for linear olefin formation. Production of linear octene using acid catalysts requires the formation of primary carbocations. We have previously studied 1-butene oligomerization on H-ferrierite and observed that the predominant products are dimethyl-hexenes, which are derived from secondary carbocation transition states [18].

Supported nickel oxide and cobalt oxide have also been used for oligomerization of short olefins such as ethylene, propylene, butene and hexene into longer chain olefins. Chauvin *et al*. reported that $NiCl_2/Al_2O_3$ after calcination at 500 ℃ in air was able to oligomerize propylene in liquid phase with 97.4% conversion and 18% *n*-hexene selectivity

with the rest of the products being mono- and di-methyl branched dimers [69]. The low selectivity of linear hexenes were reported to be due to Lewis- and Brønsted- acid sites induced by the residual chloride ions [69]. A later patent reported that alkali metal doped NiO supported on metal oxides produced *n*-octenes at 25% selectivity from butene oligomerization between 180 and 210 ℃ [70].

Highly dispersed metallic nickel and cobalt supported on carbon supports synthesized with various techniques displayed a unique hierarchical structure, and were demonstrated to have high activity, selectivity and stability in a variety of hydrogenation reactions, such as the hydrogenation of chloronitrobenzenes and nitroarenes, and the 1-octene hydroformylation [71-74].

Schultz et al. demonstrated that cobalt oxide on carbon catalysts were selective for dimerization of propylene, 1-butene and 1-hexene at 150℃ into linear olefins with selectivity of 52, 65, and 83% respectively [21, 75]. The catalysts were prepared by impregnating activated carbon with cobalt nitrate solution, with the carbon wetted with NH4OH both before and after the impregnation. The authors hypothesized that the active site was a cobalt hydride (Co(II)-H) species, as determined by a chemical titration method using wet techniques, formed after the addition of NH4OH during catalyst synthesis. The authors reported that the cobalt hydride species are thermally sensitive and are destroyed by heating at moderate temperatures (275-350℃). The authors used catalytic hydrogenation followed by GC to identify the compounds in the product mixture. Hydrogenation of these products prior to GC analysis removes the ability to confirm the formation of olefin products, or to identify the location of the double bond.

As discussed in Chapter 2, only trace amount of straight chain oligomers was observed from 1-butene conversion with H-Ferrierite, and the production of highly branched oligomers is favored due to the existence of Brønsted acid sites. In this chapter 1-butene oligomerization over cobalt on carbon catalysts will be discussed, including the identification and quantification of all of the products by 2-D GC, assessing catalyst stability in a continuous flow reactor and identifying the catalytically active site through the use of advanced characterization tools.

3.2 Experimental

3.2.1 Catalyst Preparation

Cobalt on carbon catalysts were prepared by impregnating 10.00 g of sieved activated carbon (Norit, Darco MRXm-1721, BET surface area: 600-800 m^2/g, 250-600 μm particle size) with a cobalt nitrate solution composed of

9.32 g $Co(NO_3)_2 \cdot 6H_2O$ (Sigma Aldrich) in 11.65 mL DI water. CoO_X/N-C-XXX was prepared by treating the carbon with 9.10 mL of 30% NH_4OH solution at room temperature for 0.5 h prior to cobalt impregnation. After the cobalt impregnation, the sample was then dried overnight on a hot plate at 130 ℃. Another 12.5 mL of 30% NH_4OH solution was added drop wise onto the sample and the sample was dried overnight on a hot plate at 130 ℃. XXX represents the pretreatment temperature for the catalyst. The catalyst preparation scheme is described in Figure 3.1 below.

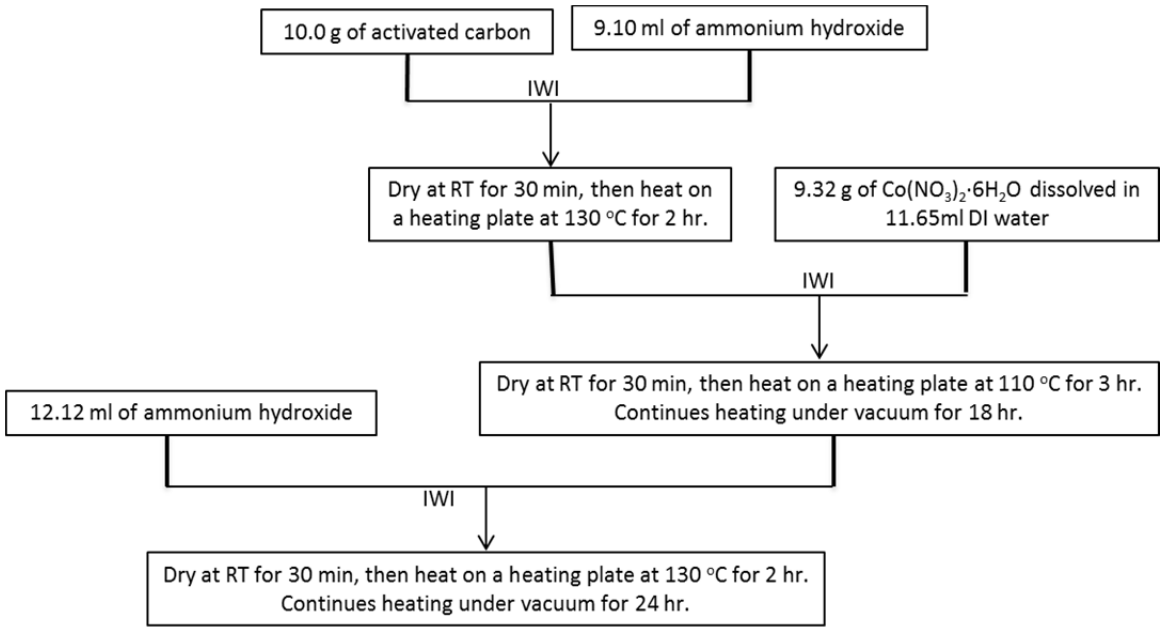

Figure 3.1 The synthesis scheme of catalyst CoO_X/N-C prior to pretreatment.

3.2.2 Catalyst Characterization

Powder X-ray diffraction (pXRD) patterns were collected with a Rigaku Rapid II diffractometer with Mo K_α source from 2^o to 45^o using a total exposure time of 30 min. Samples were packed in glass capillaries with 0.8 mm diameter and 0.01 mm thickness. Phase identification and crystallite size estimation were carried out using JADE 9 software. The Co_3O_4 crystallite size was calculated from the broadness of the cobalt spinel (311) peak at 2θ=16.79°. Samples for XRD were pretreated in flowing helium at 150 mL/min with 5.5 ℃/min ramp rate and held at a specified temperature for 2 h before the XRD measurements.

Atomic compositions for Co, H, C and N of the pretreated catalysts were determined by Galbraith Laboratories (Knoxville, TN). Thermogravimetric analysis (TGA) of the catalysts was performed with a TA instrument Q500 system. For these experiments, approximately 20 mg of sample was loaded onto a Pt pan in 80 mL/min N_2 flow with 10 ℃/min ramp rate from room temperature to 100℃ and held for 30 min, and then ramped to 800℃.

The Raman spectra were obtained with a dispersive Renishaw InVia Raman spectrometer equipped with 785, 514, and 325 nm (excitation) lasers. For this study, all measurements used a 2400 l mm^{-1} grating with an efficiency of approximately 100% at 514 nm. For *in situ* Raman studies an Olympus LMPlanFLN objective with 50× magnification and a working distance of 10.6 mm was used. The Raman was calibrated daily to an internal Si standard at 520.7 cm^{-1}. The spectra were taken with a range of 200-1200 cm^{-1} and a dispersion of 1.36565 cm^{-1} $pixel^{-1}$. *In situ* measurements were taken with a fully open aperture and a 20 s exposure time, with two accumulations. Typically, 5-10 mg of sample was placed into a Linkam CCR1000 cell. The temperature was controlled by a Linkam T95-HT system and the heating ramp was kept at 5.5 °C min^{-1}, same as that during pretreatment in the continuous flow reactor. A flow rate of 10 mL min^{-1} He (Airgas, UHP) was used for *in situ* pretreatment of the catalyst. The spectra used in this study were taken at various temperatures during the *in situ* pretreatment. Raman spectra of Co_3O_4, CoO and $Co(NO_3)_2$ bulk materials were taken at room temperature using a Leica N Plan EPI objective with 20× magnification and a working distance of 1.15 mm. The background was first subtracted from each spectrum and the resulting spectra were normalized to the area of the carbon signal at 1600 cm^{-1}.

X-ray absorption spectroscopy (XAS) measurements were taken at beamline 10-BM of the Advanced Photon Source (APS) at Argonne National lab (Lemont, IL). Co/C samples were crushed and diluted with boron nitride (Sigma-Aldrich). Self-supporting pellets were pressed inside a 4 mm I.D. stainless steel cylindrical sample holder. Sample weights were calculated to give an edge step of ~1. To allow for measurement without exposure to atmospheric conditions, the stainless steel holder was sealed in a 1” O.D. Kapton-windowed quartz tube fitted with Swagelok valves. The sealed sample was pretreated in a tube furnace while the sample tube was continually purged with He. After pretreatment, valves on the pretreatment tube were sealed and the samples were placed in the x-ray beam. Samples pretreated at 230℃ and 270℃ were analyzed without exposure to air. Samples pretreated at 350℃, 550℃ and cobalt standards were exposed to air at RT prior to analysis. XAS measurements of the Co K-edge (7.709 keV) were collected in transmission mode. X-ray absorption was measured with gas ionization chambers before and

after the sample holder. Energy calibration was performed with a Co reference foil after the sample chamber. Oxidation states were quantified by comparison of the x-ray absorption near edge structure (XANES) with the experimental standards. Co/C samples were fit with a linear combination of Co foil, CoO, and Co3O4 in the range of -30 to +20 eV from the Co edge energy.

The TEM images were obtained using a JEOL 2010F field emission gun (FEG) transmission electron microscope (TEM). The TEM was operated at an accelerating voltage 200 keV. Conventional TEM images were recorded using a Gatan multi-scan digital camera (Model Ultrascan 1000).

3.2.3 Catalytic Measurement

1-Butene oligomerization reactions were carried out in a down-flow fixed-bed reactor with the liquid product analyzed by a comprehensive two-dimensional gas chromatograph-mass spectrometer (2D-GC-MS) as described in our earlier work [18]. The C4 compounds in the liquid or gas products were analyzed *via* conventional gas chromatography (GC-FID, Shimadzu). Skeletal composition of the product mixture was separately verified by hydrogenating the liquid product prior to analysis by 2D-GC-MS. Approximately 100 mg of Pd/C catalyst was packed into the GC liner for hydrogenation. Only two C8 products were observed after hydrogenation, which are 3-methyl-heptane and n-octane, respectively; and all the detectable hydrogenated C12 products were branched species. The thermodynamic equilibrium composition calculations were based on Benson group thermodynamic data from Alberty and Gehrig [76] by assuming that pressure has little effect on the change of the physical property of the compounds. The equilibrium concentrations were solved by setting the change of Gibbs free energy to zero (G353k(i)=0) for isomerization reaction between the isomers. The following standards were tested for our product analysis: 1-octene, trans-2-octene, cis-2-octene, 2-methyl-1-heptene, 2-methyl-2-heptene, trans-2-methyl-3-heptene, trans-6-methyl-3-heptene, 2,3-dimethyl-2-hexene, 2,3-dimethyl-3-hexene, 2,3,4-trimethyl-2-pentene, 2,4,4-trimethyl-2-pentene (Sigma-Aldrich), cis-2,5-dimethyl-3-hexene (Pfaltz & Bauer) cis-3-octene, trans-3-octene, cis-4-octene, trans-4-octene, 3-methyl-2-heptene, 3-methyl-3-heptene, 5-methyl-2-heptene, 5-methyl-3-heptene, 3,4-dimethyl-2-hexene (ChemSampCo). For all the catalytic testing, 0.5 g of the catalyst particles were packed into the tubular reactor without diluents. The catalysts were pretreated in 150 mL/min flow of helium with 5.5 ℃/min ramp rate and held at the pretreatment temperature for 2 h before the reactor was cooled to reaction temperature. 1-Butene (99.9%, Matheson) was fed into the reactor at reaction pressure (450 psig) through a high-pressure syringe pump

(500D, Teledyne Isco). The liquid samples were collected at atmospheric pressure in a 50 mL glass pressure tube pre-chilled in dry ice filled with approximately 10 g of 0.5 wt% heptane in hexane solvent. During liquid sample draining, the volatilization of a small amount of hydrocarbon products was inevitable which could lead to a below 100% carbon balance. The variation of weight hourly space velocity (WHSV=hourly mass liquid feed flow rate (g/h)/catalyst mass (g)) was achieved by adjusting the butene flow rate at the inlet. After reaction, the spent catalysts were recovered from the reactor and exposed to the air before XRD characterization.

The butene conversion was calculated according to Equation 3.1. Butene consumption rate was calculated according to Equation 3.2. When calculating the kinetics values, butene isomers including 1-butene, *trans*- and *cis*-2-butene were grouped together and considered to be non-converted feed. The number of chain branches (NCB) was calculated according to Equation 3.3. Total C4 dimer distribution, total linear octene distribution were calculated using Equation 3.4 and Equation 3.5, respectively.

Equation 3.1 Butene conversion (%) = (mols of carbon in the detected products)/(mols of carbon in the feed butene) × 100%

Equation 3.2 Butene consumption rate ($mol_{butene}/mol_{Co}/h$) = (butene inlet flow rate × butene conversion)/(mol cobalt in the catalyst)

Equation 3.3 NCB = [0 × linear octene distribution (%) + 1 × methyl-heptene distribution (%) + 2 × dimethyl-hexene distribution (%)]

Equation 3.4 Total C4 dimer distribution (%) = (the carbon moles in the C8 olefins)/(the sum of carbon moles in all the detected products) × 100%

Equation 3.5 Total linear octene distribution (%) = (moles of linear octene)/(moles of total C8 olefins) × 100%

3.3 Results and Discussion

3.3.1 Oligomer Product Selectivity

The 2D-GC reveled the cobalt-catalyzed butene oligomerization reactions only produces longer chain olefins (Figure 3.2a). Over 94% of the non-C4 products were butene dimers for all catalysts used in this study as shown in Figure 3.2b. Additional products were branched C12 olefins. A small amount of C16 olefins (0.3% selectivity) was observed for the CoO_X/N-C-230 catalyst run at the lowest WHSV (0.25 h^{-1}). C8 isomer identification was carried out by matching the location of the product trace in the 2D-GC image with that of standards. The 2D-gas chromatogram of a typical product distribution is shown in Figure 3.2. Figure 3.2a shows the overall 2D-GC

template and Figure 3.2b shows the zoomed in region for the C8 olefins along with the assignment of each peak. Hydrogenation of our product mixture and analysis with Pd/C showed that our products only contained n-octenes and methyl-heptenes corroborating our assignments made using the 2D-GC. The *trans* and *cis* isomers of 3-octene and 4-octene were not distinguishable. The only methyl-heptene isomers that we observed were 5-methyl-heptenes and 3-methyl-heptenes.

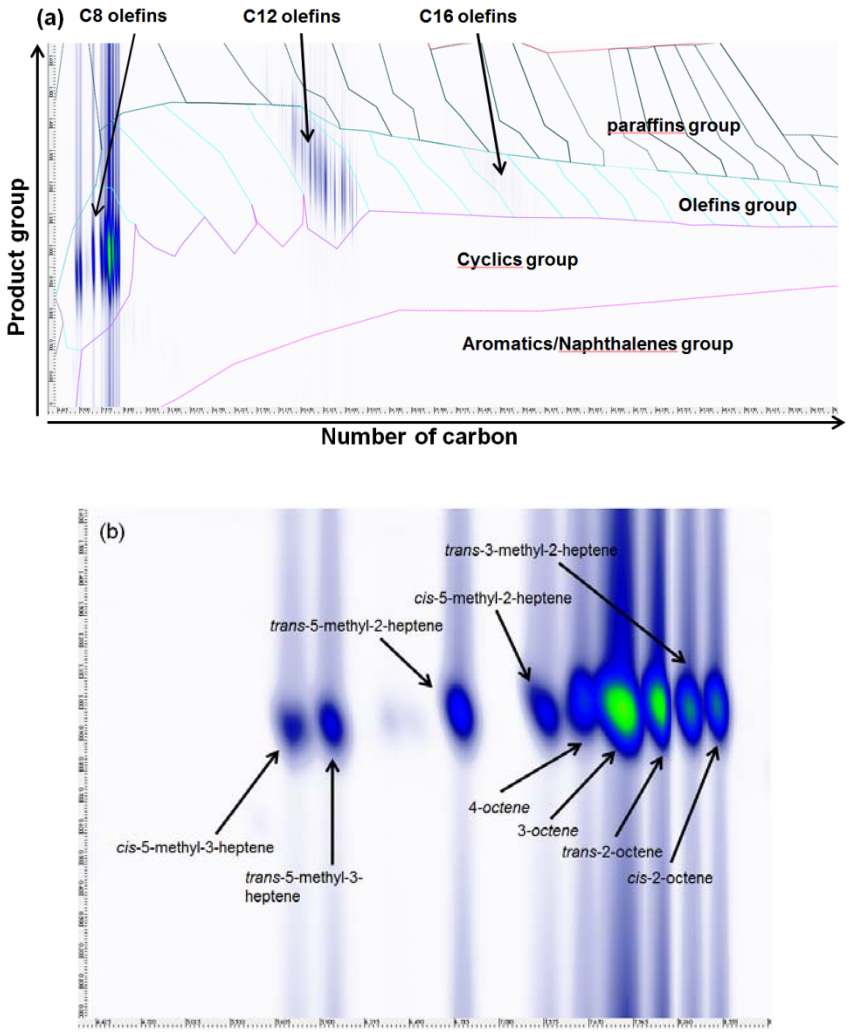

Figure 3.2 2D-GC image of (a) all potential C8-C20 products and (b) butene dimerization products assignment for the run over CoO_X/N-C-230 at 0.25 h^{-1} WHSV and 27 h time on stream for 1-butene conversion at 80 ℃, 450 psig.

Table 3.1 Average product selectivity for butene oligomerization (reaction conditions: 80 ℃, 450 psig).

Catalyst	CoO_X/N-C-230			CoO_X/N-C-270			CoO_X/N-C-350	
WHSV(hr^{-1})	14.14	0.71	0.25	14.14	0.71	0.25	14.14	0.71
TOS/h	40	94	37	40	91	35	40	75
Conversion (%)	9.77	11.42	29.00	3.94	5.74	21.4	1.27	6.74
Total C4 dimer selectivity (%)	98.5	96.6	94.4	98.7	96.6	97.6	99.6	97.6
Total C12 selectivity (%)	1.5	3.4	5.3[a]	1.3	3.4	2.3[b]	0.4	2.4
Specific C4 dimer distribution(%)								
cis-2-octene	12.3	7.1	6.9	11.6	6.0	12.8	7.7	5.3
trans-2-octene	17.7	19.7	19.8	17.3	16.9	17.6	24.7	16.4
cis/*trans*-3-octene	52.9	45.4	43.9	52.5	42.5	54.7	46.1	39.6
cis/*trans*-4-octene	1.3	5.3	7.7	1.4	8.7	2.2	5.4	13.4
cis-5-methyl-3-heptene	1.7	2.2	1.8	2.2	2.7	1.5	1.6	1.0
trans- 5-methyl-3-heptene	1.9	2.5	2.7	2.0	2.9	2.2	2.0	3.2
trans-3-methyl-2-heptene	3.3	9.8	9.6	4.9	12.3	3.6	5.6	12.7
trans-5-methyl-2-heptene	2.6	4.0	4.3	3.2	4.6	2.7	3.4	5.0
cis-5-methyl-2-heptene	6.1	4.0	3.2	5.9	3.4	2.8	3.3	2.8
NCB	0.16	0.23	0.21	0.18	0.26	0.14	0.16	0.25
Total linear octene distribution (%)	84.2	77.5	78.4	82.8	74.1	87.2	83.9	74.7
Carbon balance (%)	90.4	103.2	98.3	89.4	90.3	104.2	96.5	103.6

[a] C_{16} olefin was also observed with 0.3% selectivity.
[b] C_{16} olefin was also observed with 0.1% selectivity.

As shown in Table 3.1 between 77 to 90% of the products were linear octenes, which is higher than the previous studies (about 65%) [21]. Only minor amounts of 1-octene (less than 1%) were observed. At low WHSV the linear octene products in decreasing abundance were 3-octene > trans-2-octene> cis-2-octene > 4-octene. The 3-octene and cis-2-octene distribution decreases and the 4-octene distribution increases with conversion. It is likely that the C8 products tend to approach equilibrium of octene isomers (Table 3.2) at higher conversion. Aside from linear octenes, all four catalysts produced trans-3-methyl-2-heptene, *trans*- and *cis*-5-methyl-3-heptene, and *trans*- and *cis*-5-methyl-2-heptene. No alpha methyl-heptene products were detected. The octene product distribution is similar among the four different catalysts.

Table 3.2 Experimental and equilibrium Linear Octene distribution (reaction conditions: 80 ℃, 450 psig)

	CoO_X/N-C-230			Equilibrium
WHSV(h^{-1})	14.14	0.71	0.25	
Conversion (%)	9.77	11.42	29	
1-octene	0	0	0	0.83
cis-2-octene	14.61	9.16	8.81	8.49
trans-2-octene	21.02	25.42	25.29	35.25
cis/trans-3-octene	62.83	58.58	56.07	34.76
cis/trans-4-octene	1.54	6.84	9.83	20.67
cis-2-octene/trans-2-octene	0.69	0.36	0.35	0.24

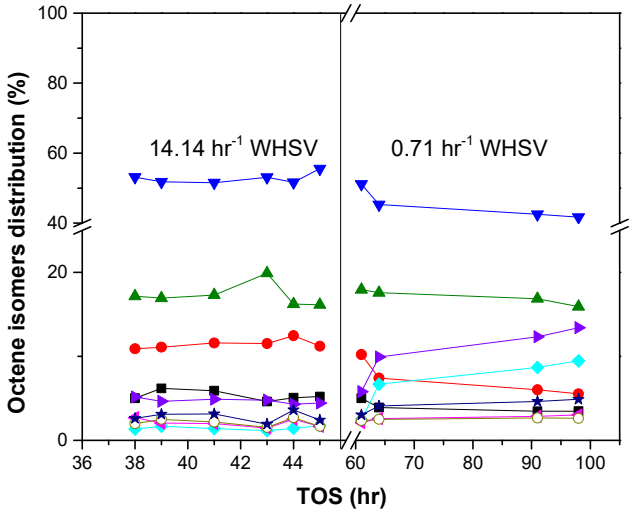

Figure 3.3 Octene isomers distribution with time on stream over CoO_X/N-C-270, including: (▼) trans-3-octene, (▲) trans-2-octene, (●) cis-2-octene, (■) cis-5-methyl-2-heptene, (►) 3-methyl-2-heptene, (◆) trans-4-octene, (◄) trans-5-methyl-3-heptene, (○) cis-5-methyl-3-heptene and (★) trans-5-methyl-2-heptene at 80℃ and 450 psig.

Figure 3.3 shows the octene product distribution as a function of time on stream for CoO_X/N-C-270. The octene distribution was nearly constant at 14.14 h^{-1} WHSV even though the butene conversion was slightly decreasing during this time. At higher conversion (0.71 h^{-1} WHSV), the selectivity of linear octenes, except *trans*-4-octene, decreases and the selectivity of *trans*-3-methyl-2-heptene increases with time on stream. Similar trends were observed for all the other catalysts including CoO_X/N-C-230 (Figure 3.4) and CoO_X/N-C-350 (Figure 3.5).

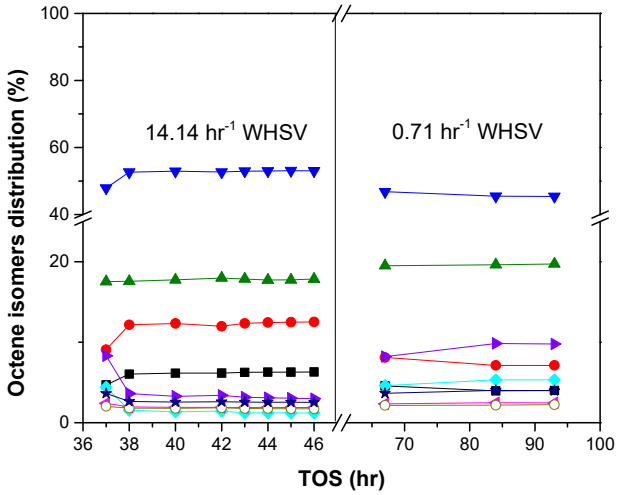

Figure 3.4 Octene isomers distribution with time on stream over CoO_X/N-C-230, including: (▼) trans-3-octene, (▲) trans-2-octene, (●) cis-2-octene, (■) cis-5-methyl-2-heptene, (►) 3-methyl-2-heptene, (◆) trans-4-octene, (◄) trans-5-methyl-3-heptene, (○) cis-5-methyl-3-heptene and (★) trans-5-methyl-2-heptene at 80℃ and 450 psig.

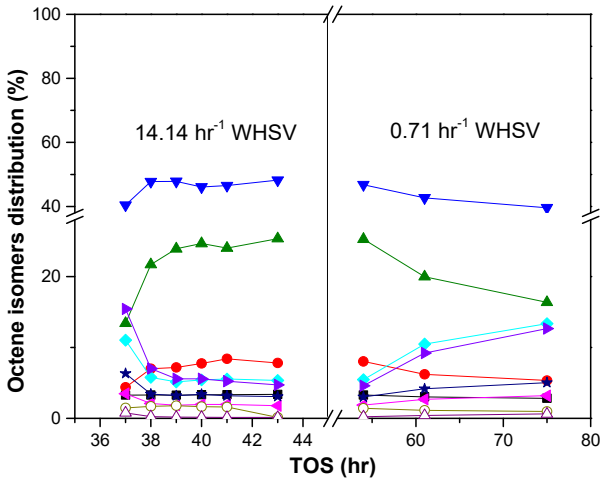

Figure 3.5 Octene isomers distribution with time on stream over CoO_X/N-C-350, including: (▼) trans-3-octene, (▲) trans-2-octene, (●) cis-2-octene, (■) cis-5-methyl-2-heptene, (►) 3-methyl-2-heptene, (◆) trans-4-octene, (◄) trans-5-methyl-3-heptene, (○) cis-5-methyl-3-heptene and (★) trans-5-methyl-2-heptene at 80℃ and 450 psig.

The hydrocarbon selectivity we determined is fairly consistent with the analyses of Shultz *et al.* who reported a hydrogenated mixture composition of 65.3% n-octane, 34.4% 3-methyl-heptane and 0.3% 3,4-dimethyl-hexane at 13.6% 1-butene conversion [21]. Key differences are that we did not observe the formation of dimethyl hexene and the selectivity to linear octene was 8.8-21.9% higher in our study. The observed linear octene selectivity was also

higher compared to the ion-exchanged zeolites (below 40%) [20, 68]. Unlike olefin oligomerization with homogeneous catalysts no 1-octene was detected [13, 62-64].

3.3.2 Catalytic Activity Measurements

The effect of pretreatment on the catalytic activity was studied by activating the catalyst at different temperatures in helium. Figure 3.6a and Figure 3.6b compare the butene consumption rate of CoO_X/N-C-230, CoO_X/N-C-270, CoO_X/N-C-350 and CoO_X/N-C-550 catalysts at 14.14 h^{-1} and 0.71 h^{-1} WHSV, respectively. All catalysts were tested by the following reaction sequence: 0.71 h^{-1} WHSV for approximately 36 h, then 10 h of operation at 14.14 h^{-1} WHSV, followed by 40 h of operation at 0.71 h^{-1}. Faster catalyst deactivation was observed if the catalyst was tested starting at the higher WHSV (Figure 3.7).

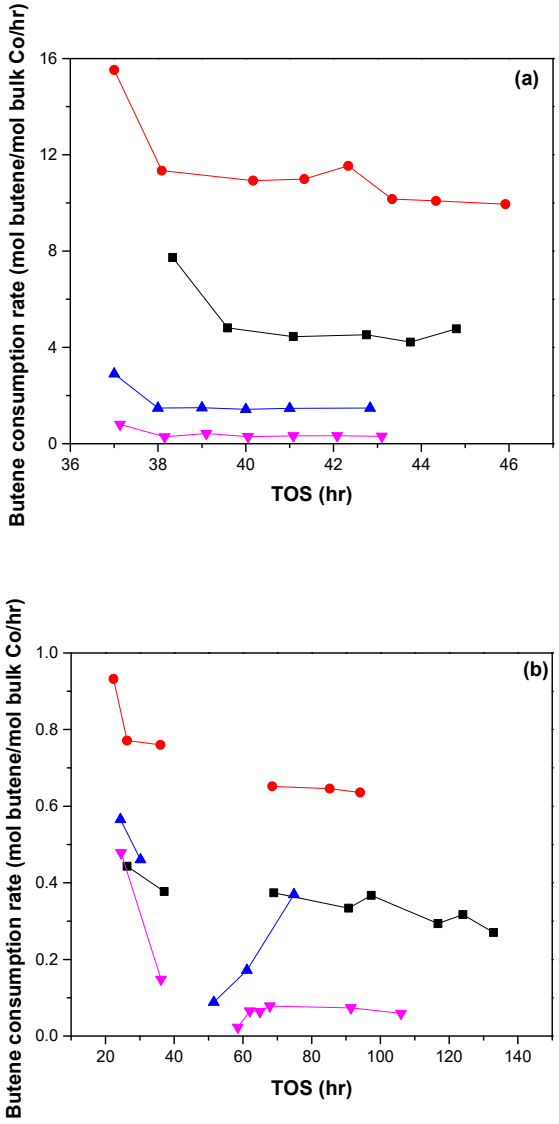

Figure 3.6 Butene consumption rate as a function of time on stream for (●) CoO_X/N-C-230, (■) CoO_X/N-C-270, (▲) CoO_X/N-C-350 and (▼) CoO_X/N-C-550, at (a) 14.14 h^{-1} WHSV and (b) 0.71 h^{-1} WHSV. Reaction condition: 1-butene feed, 450 psig, 80 ℃.

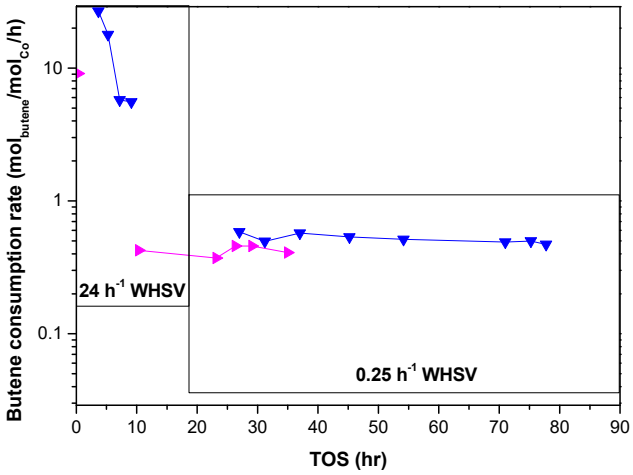

Figure 3.7 Catalyst activity for (▼) CoO_X/N-C-230 and (►) CoO_X/N-C-270 vs TOS at 24 h^{-1} and 0.25 h^{-1} WHSV.

Average butene conversion, deactivation rate and average butene consumption rate for each catalyst are summarized in Table 3.3 at both space velocities. At 14.14 h^{-1} WHSV, the activity of the catalysts decreased with increasing pretreatment temperature. It is worth noting that by lowering the pretreatment temperature from 270 to 230 ^{o}C, the reaction rate doubled. A steady catalytic performance was observed for each catalyst after the first sampling point. The average rate for each catalyst decreased at a lower WHSV of 0.71 h^{-1} (Figure 3.6b). CoO_X/N-C-230 is the most active catalyst at both 14.14 (Figure 3.6a) and 0.71 h^{-1} WHSV. A slow deactivation was observed at the higher WHSV with CoO_X/N-C-230 while no deactivation was observed with the other catalysts. At the lower WHSV a much slower deactivation rate was observed.

Table 3.3 Average reaction rates and deactivation rates for 1-butene oligomerization. Reaction condition: 1-butene feed, 450 psig, 80 ℃, 14.14 h^{-1} WHSV and 0.71 h^{-1} WHSV.

	14.14 h^{-1} WHSV			0.71 h^{-1} WHSV		
Catalyst	Average butene conversion (%) [a]	Deactivation rate at steady state (h^{-2}) [b]	Average rate (mol_{butene}/ mol_{Co}/h) [c]	Average butene conversion (%) [a]	Deactivation rate (h^{-2}) [b]	Average rate (mol_{butene}/ mol_{Co}/h) [c]
CoO_X/N-C-230	10.11	0.19±0.07	10.78	13.10	$(3.20\pm0.89)\times10^{-3}$	0.73
CoO_X/N-C-270	5.08	-	5.08	6.06	$(1.26\pm0.23)\times10^{-3}$	0.35
CoO_X/N-C-350	1.50	-	1.71	6.02	N.A.	0.33
CoO_X/N-C-550	0.36	-	0.39	2.20	$(3.53\pm1.51)\times10^{-3}$	0.12

[a,c] Mathematical average of the data taken with TOS shown in Figure 3.6a (14.14 h^{-1}) and Figure 3.6b (0.71 h^{-1}).
[b] The value of the slope caculated from Figure 3.6a except for the first sampling point.
[c] The value of the slope calculated from Figure 3.6b, accounting for all the data points collected.

The butene distribution is shown in Figure 3.8 for CoO_X/N-C-230. At the higher WHSV these products were not in thermodynamic equilibrium with 1-butene being the main butene isomer. The three butene isomers deviate further from their equilibrium compositions with increasing time-on-stream. At 0.71 h^{-1} WHSV the butene isomers were in thermodynamic equilibrium as shown in Figure 3.8b. Schultz *et al.* also observed isomerization of 1-butene to *cis*- and *trans*-2-butene during 1-butene dimerization in a batch reactor [21], with the butene isomers compositions close to their equilibrium (10.6% 1-butene, 31.1% *cis*-2-butene and 58.2% *trans*-2-butene).

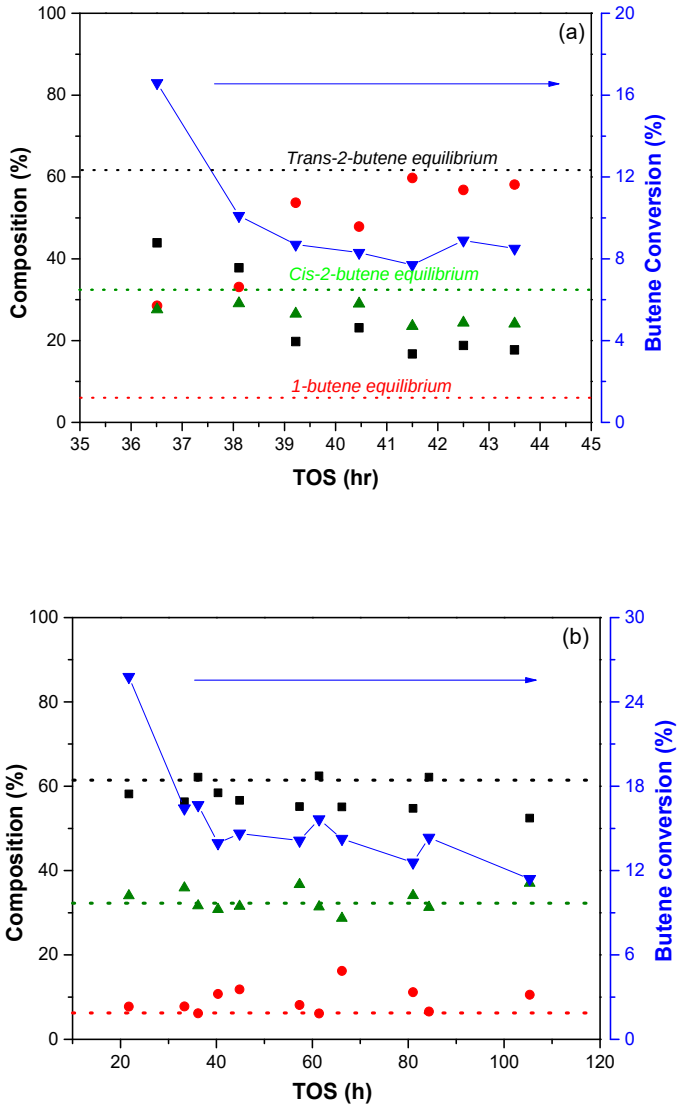

Figure 3.8 Total butenes conversion (▼) and C4 olefin distribution as a function of time on stream: (■) *trans*-2-butene, (●) 1-butene, (▲) *cis*-2-butene, and butene distribution equilibrium (dotted lines) at 80℃, 450 psig, 1-butene feed at (a) 14.14 h^{-1} WHSV (b) at 0.71 h^{-1} WHSV over CoO_X/N-C-230.

The absence of heat and mass transport limitations were verified by commonly-accepted calculations for heterogeneous catalysts systems [77]. Heat effects due to interphase, interparticle and intraparticle heat transport were evaluated. The heat of reaction (42 kJ/mol) was determined from the heat of formation of reactants and products at reaction temperature. An activation energy (Ea) of 70 kJ/mol was used based on the work of Toch *et al.* for ethylene oligomerization [78]. The heat transfer coefficient (300 $Wm^{-1}K^{-1}$) for the liquid-phase was determined by assuming a stagnant hydrocarbon film. The thermal conductivity of the catalyst was estimated to be the same as

the carbon support (0.1 $Wm^{-2}K^{-1}$). An energy balance on the heat generated and removed showed a negligible temperature rise between the bulk phase and the catalyst surface.

For mass transfer effects, it was assumed that diffusion within the porous support or interparticle mass transport would be the limiting regime. The Weisz-Prater criteria was evaluated to ensure the absence of concentration gradients within the catalyst particles. In the absence of an absolute value for the diffusivity of liquid-phase 1-butene through its oligomer products, the diffusivity was estimated to be within the range of liquid systems (8×10^{-6} cm^2/s). The concentration of 1-butene at the surface of the particle was conservatively estimated to be 80% of the concentration in the unreacted stream. Based on the calculations (Table 3.4), the reaction is not limited by transport phenomena for the data collected in this paper [79].

Table 3.4 Mass and heat transfer evaluation.

	Formula	Computed Values		Target
		14.14 h^{-1} WHSV	0.71 h^{-1} WHSV	
Interphase heat	$\frac{\lvert\Delta H\rvert r''' r_p}{hT_b} < 0.15\ \frac{RT_b}{E}$	7.8×10^{-3}	1.0×10^{-4}	$<1.1\times10^{-2}$
Interparticle heat	$\frac{\lvert\Delta H\rvert r''' r_p^2}{k_e T_w} < 0.4\ \frac{RT_w/E}{\left[1+8\left(\frac{r_p}{R_0}\right)Bi_w\right]}$	1.4×10^{-2}	1.8×10^{-4}	$<1.6\times10^{-2}$
Intraparticle heat	$\frac{\lvert\Delta H\rvert r''' r_p^2}{\lambda T_s} < 0.75\ \frac{RT_s}{E}$	1.4×10^{-2}	1.8×10^{-4}	$<3.1\times10^{-2}$
Interphase mass	$\frac{r_{obs}R_p}{C_B k_D}$	1.1×10^{-5}	1.4×10^{-7}	<0.15
Intraparticle mass	$\frac{r_{obs}R_p^2}{C_s D_{eff}}$	0.4	5.3×10^{-3}	<0.6

Nomenclature: ΔH-heat of reaction, r'''-rate per catalyst volume, r_p-radius of particles, T_b-bulk fluid temperature, h-convective heat transfer coefficient, k_e-effective thermal conductivity, λ-effective thermal conductivity, Bi-Biot number, E-activation energy, R_p-radius of particles, C_B-concentration in bulk fluid, C_S-concentration at catalyst surface, k_D-mass transfer coefficient, D_{eff}-effective diffusivity.

3.3.3 Catalyst Characterization

Table 3.5 shows the elemental analysis and Co_3O_4 crystallite size for the fresh and spent catalysts. All catalysts and the activated carbon contained nitrogen. The nitrogen comes from three potential sources: undecomposed cobalt nitrate, activated carbon support, and NH_4OH. Similar amounts of nitrogen are observed on the spent catalyst (CoO_X/N-C-270) demonstrating that nitrogen is not lost from the catalyst during reaction.

Table 3.5 Elemental analysis and crystallite size estimation of fresh and spent catalysts. (Spent catalyst values are put in parenthesis when available).

Catalyst Code	Elemental Analysis (wt%)			Co_3O_4 Crystallite size (nm) by XRD [a]
	Co	C	N	
CoO_X/N-C-230	13.20	51.83	1.24	7.2±0.2 (6.2±0.2)
CoO_X/N-C-270	12.30 (13.20)	63.41 (56.90)	1.64 (1.76)	6.4±1.6 (5.4±0.2)
CoO_X/N-C-350	12.3	54.61	1.37	5.7±0.2 (5.8±0.2)
CoO_X/N-C-550	15.4	58.31	1.41	N.A.
CoO_X/N-C-270	-	71.22	0.96	-
Activated carbon	-	65.59	0.60	-

[a] The number in the bracket specifies the particle size for the corresponding spent catalyst. The errors were estimated by JADE software.

X-ray diffraction identified three phases on all catalysts (except for CoO_X/N-C-550) as shown in Figure 3.9: graphite (largest 2θ peak at 12.15°), Co_3O_4 (largest 2θ peak at 16.79°) and CoO (largest 2θ peak at 19.26°). An extra high intensity peak was observed over CoO_X/N-C-550 at 2θ=19.90°. This peak is metallic cobalt. The Co_3O_4 crystallite size calculated by Scherrer's equation with the peak at 16.79° was shown to be between 5-8 nm (Table 3.5). The Co_3O_4 crystallite size for CoO_X/N-C-550 could not be obtained from this data. HRTEM images of CoO_X/N-C-270 (Figure 3.10) exhibit overlapping cobalt oxide particles supported on carbon, with a particle size ranging from 5 to 10 nm. The Co_3O_4 particle size was not measured using HRTEM due to the overlapping cobalt oxide particles. The Co_3O_4 crystallite size calculated by XRD showed a slight decrease with increasing pretreatment temperature. The XRD results of the used catalysts showed similar cobalt phase composition, with no distinguishable change in Co_3O_4 crystallite size (Figure 3.11) compared to the fresh catalysts. Some of the changes of crystallite size may not be observable with XRD because small (< 4nm) Co_3O_4 crystallite sizes are not detected with this method [80]. No leaching occurred with the spent catalyst as there was no change in the XRD patterns or the cobalt weight loading for the fresh and spent catalysts.

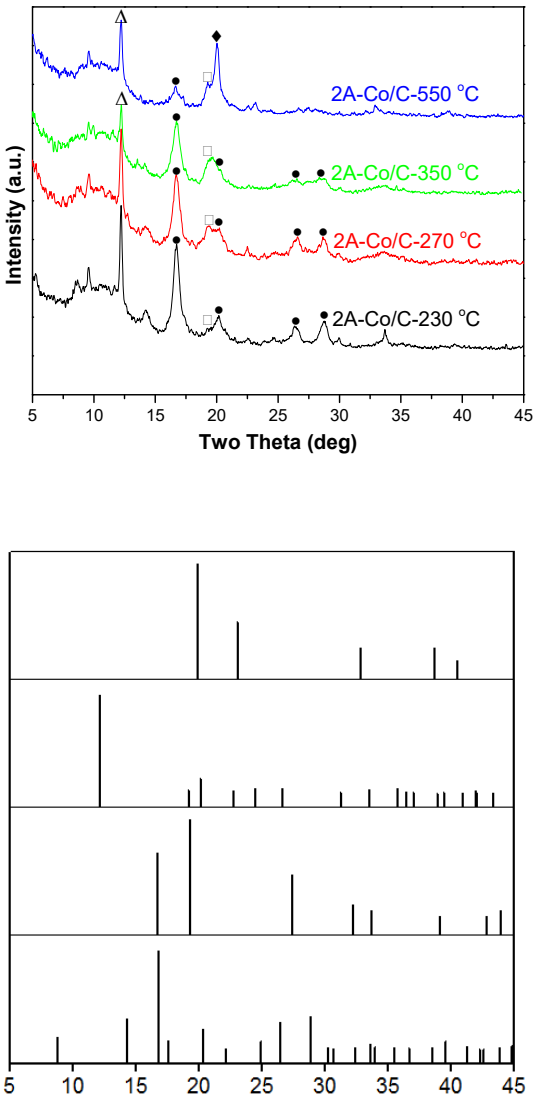

Figure 3.9 Mo-XRD of CoO_X/N-C catalysts pretreated at different temperatures, with characteristic peaks of △ graphite, ●Co_3O_4, □CoO, ◆Co.

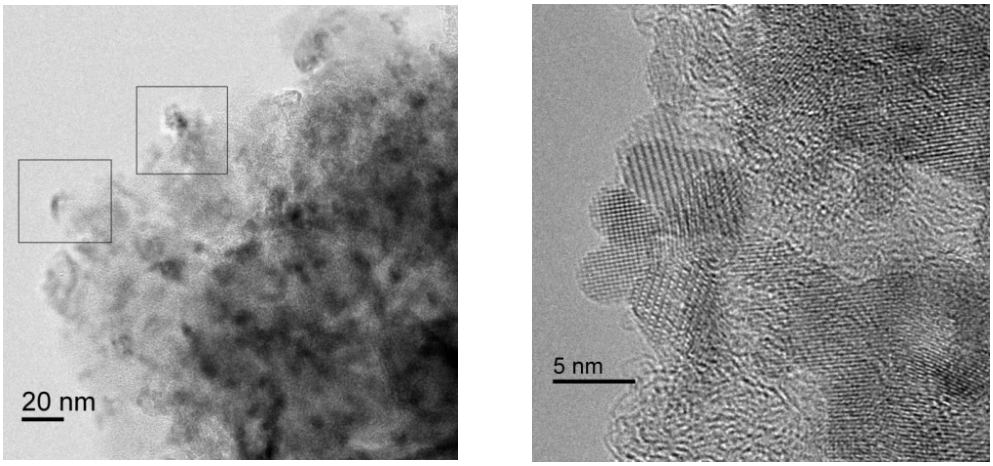

Figure 3.10 HRTEM image for CoO_X/N-C-270. Left: overlapping cobalt oxide particles. Right: zoomed-in image showing the lattice fringes of the cobalt particles.

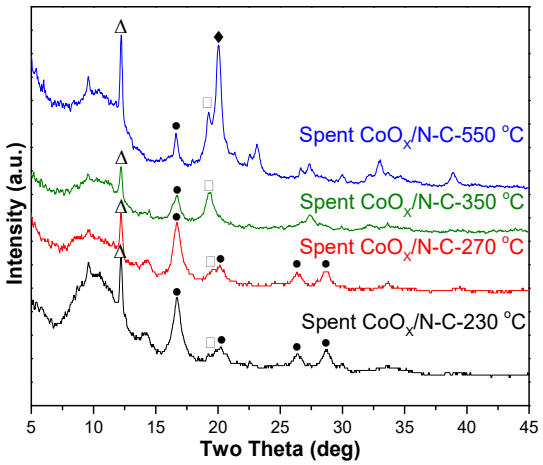

Figure 3.11 Mo-XRD patterns of the spent catalysts, with characteristic peaks of △graphite, ●Co_3O_4, □CoO, ◆ Cubic Co.

The *in situ* Raman spectra of the CoO_X/N-C catalyst during pretreatment are shown in Figure 3.12. Spectrum (a) shows characteristic peaks of Co_3O_4 bulk material at 481, 519, 621 and 690 cm^{-1}, whereas spectrum (b) shows CoO bulk material characteristic peaks at 517 and 684 cm^{-1}. Characteristic peaks of bulk $Co(NO_3)_2$ at 740, 1034, 1321 and 1442 cm^{-1} are present in the spectrum (c). Due to the highly intense Raman spectra for the bulk materials, spectra (a) and (c) are divided to 1/2 intensity. The spectrum (d) shows that at room temperature, before pretreatment, a mixture of $Co(NO_3)_2$ and cobalt oxides coexist on the catalyst surface. Raising the temperature from 25 to 150 °C leads to a decrease in the intensity of the $Co(NO_3)_2$ peaks at 740 and 1034 nm^{-1} (d-f), and to the

emergence of new Raman signals at 481 and 690 cm^{-1} (g), indicating the decomposition of the $Co(NO_3)_2$ precursor and the formation of Co_3O_4 and CoO. The decomposition temperature of the precursor observed by Raman (f) is about 50 ^oC lower than that obtained by TGA (Figure 3.16). This indicates that cobalt oxides on the catalyst surface reduce at a lower temperature than in the bulk [81]. Since the characteristic peaks of CoO (broad signal at 517 and 684 cm^{-1}) and Co_3O_4 (481, 519 and 690 cm^{-1}) overlap, the precise composition of cobalt oxide on the catalyst surface cannot be determined. The signal intensity of CoO at 684 cm^{-1} is much lower and broader than Co_3O_4 [82]. By monitoring the decrease and, more importantly, the broadening of the peak (Figure 3.13), the change of the CoO content can be qualitatively observed. As temperature increases from 150 to 550℃ ((f)-(n)), the peak at 690 cm^{-1} decreases and broadens, suggesting less Co_3O_4 and an increased CoO content.

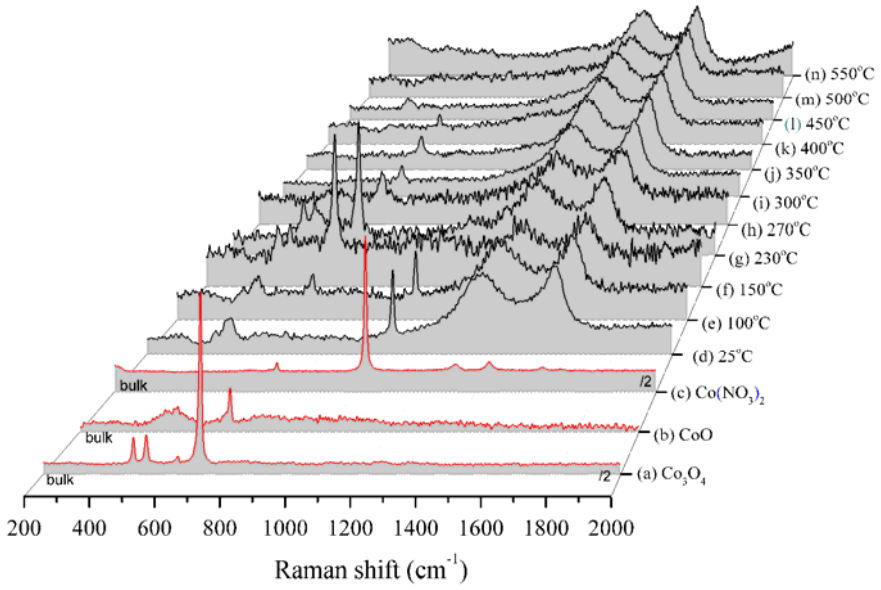

Figure 3.12 *In-situ* Raman spectra of cobalt nitrate, Co_3O_4, CoO, and CoO_X/N-C pretreated at different temperatures. Helium flow = 20 mL/min.

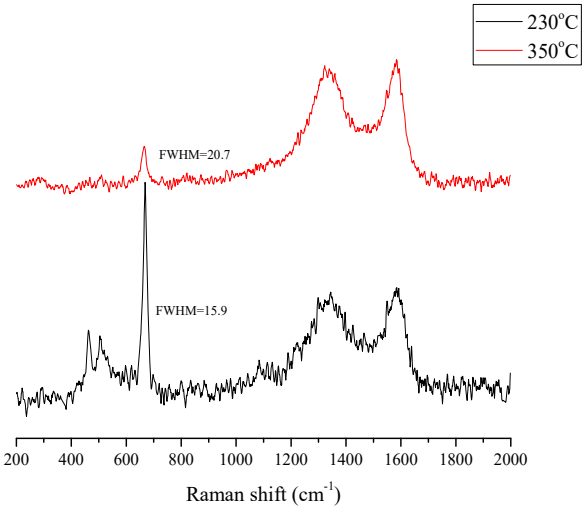

Figure 3.13 Comparison of CoO_x signal at 690 cm^{-1} during pretreatment at 230 ℃ and 350 ℃.

The composition of the cobalt phases was further investigated with XANES. Figure 3.14 shows the XANES spectra of CoO_X/N-C pretreated in helium at different temperatures. The catalysts pretreated at 230 and 270 °C were analyzed immediately after helium pretreatment without being exposed to the air. The cobalt standards and the catalysts pretreated at 350 and 550 ℃ were exposed to air at room temperature before analysis. The phase compositions of these different catalysts after linear combination fitting are summarized in Table 3.6. CoO_X/N-C-230 and CoO_X/N-C-270 showed similar XANES to a Co_3O_4 standard (Figure 3.15), while CoO_X/N-C-350 and CoO_X/N-C-550 curves clearly shifted to a lower edge energy, as shown in Figure 3.14. The gradual reduction to metallic cobalt is apparent with samples pretreated at higher temperatures and observable as a large pre-edge feature and decreasing edge peak or “white line”. There is a clear trend of decreasing oxidation with increasing pretreatment temperature.

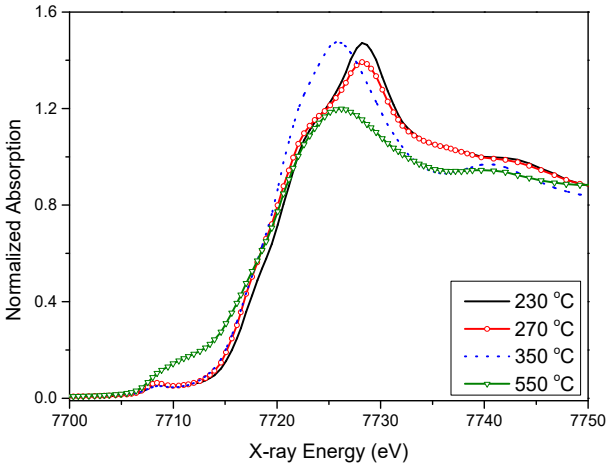

Figure 3.14 XANES spectra of fresh CoO_X/N-C catalysts pretreated at different temperatures.

Table 3.6 XANES fitting results.

Sample	Edge Energy (eV)	XANES fit wt%			Co(III) /Co(II)
		CoO	Co	Co_3O_4	
CoO_X/N-C-230	7720.7	27.5	-	72.5	1.64
CoO_X/N-C-270	7720.1	32.0	-	68.0	1.32
CoO_X/N-C-350	7720.5	61.7	-	38.3	0.39
CoO_X/N-C-550	7720.5	40.1	36.2	23.7	0.37
CoO	7720.1	-	-	-	
Co_3O_4	7724.2	-	-	-	
Co	7708.2	-	-	-	

The ratio of Co(III)/Co(II) for each sample was calculated based on XANES fitting results and is summarized in Table 3.6. Co_3O_4 contains both Co(II) and Co(III) in the molecular formula of $Co_2O_3 \cdot CoO$. The Co_3O_4 content decreases with an increasing pretreatment temperature. Metallic cobalt starts to form when the pretreatment temperature is 550 ℃. As shown in Table 3.3, the catalyst activity decreases with increasing pretreatment temperature, suggesting the Co_3O_4 phase is probably the more active phase.

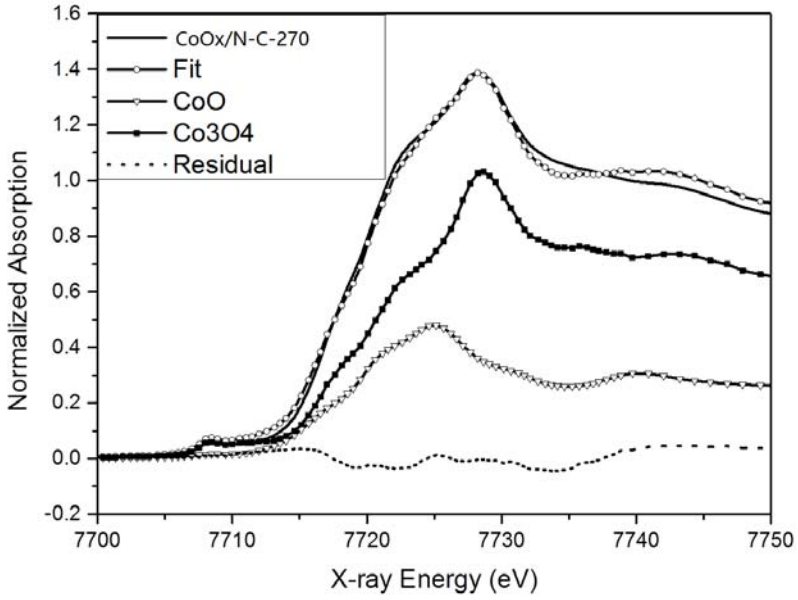

Figure 3.15 Fitted XANES spectra for CoO_X/N-C-270 showing weighed spectra, linear combination fit, and residual difference between the fit and the data.

Figure 3.16 Shows the TGA analysis of the non-pretreated catalysts in flowing N_2. The CoO_X/N-C catalyst showed two weight loss peaks at 208 ℃ and 621 ℃. The peak at 208 ℃ can be assigned to the complete decomposition of cobalt nitrate [83, 84]. The weight loss at 621℃ is caused by the reduction of Co_3O_4 to a lower oxidation state (metallic cobalt or CoO), as indicated by XRD and XAS.

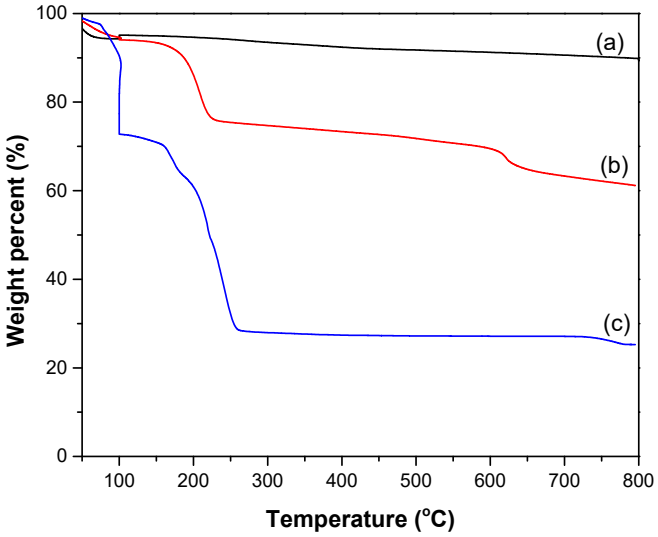

Figure 3.16 TGA analysis of (a) ammoniated carbon (no weight loss); (b) CoO_X/N-C (18.61 wt% loss at 208℃, 6.11 wt% loss at 621℃); (c) cobalt precursor: $Co(NO_3)_2{\cdot}6H_2O$ (total 73.76 wt% loss between 100 and 254℃) in N_2 with 10℃/min ramp rate.

From the analysis of XRD, *in situ* Raman, TGA and XAS results, a cobalt phase change occurs with an increasing pretreatment temperature in an inert gas. The first step is the complete decomposition of $Co(NO_3)_2{\cdot}6H_2O$ to Co_3O_4 which occurs at around 208 ℃ [85, 86]. However, Co_3O_4 is not the only cobalt oxide being formed even at temperature as low as 230 ℃. CoO could be formed either as a by-product from cobalt nitrate decomposition, or from the reduction of Co_3O_4 by the carbon support. With an increasing pretreatment temperature, more Co_3O_4 is converted to CoO, followed by a further reduction of CoO to Co when the temperature reaches 550 ℃. We plan on exploring the nature of cobalt oxide formation and subsequent high temperature reduction in the future.

3.3.4 Discussion on Reaction Pathway

A proposed reaction pathway for butene dimerization over cobalt–on carbon catalyst is shown in Figure 3.17. Schultz *et al.* proposed that a cobalt hydride species is the active catalytic site and mediates the olefin oligomerization [21, 75]. Our methods of analysis of the catalyst show that the cobalt particles (surface and bulk) are

principally composed of CoO and Co_3O_4. Demonstrating the presence of Co-H through direct characterization has thus far remained elusive. However, as suggested by recent studies on homogeneous cobalt complex catalysts for olefin oligomerization, cobalt hydride was frequently described as the active center generated upon activation of a Co(II) species [17, 87]. Our proposed pathway is based upon our spectroscopic characterization, catalytic performance and kinetic data, especially the olefin product mixture. While the potential role of cobalt hydride species cannot be neglected and could be responsible for olefin isomerization, the classical Cossee olefin coordination, insertion and β-H elimination pathway for 1-butene dimerization would produce 3-methylidene heptane and 3-methylidene-4-methyl-hexane, which we do not observe [88]. Additionally it would be expected that under high olefin concentration or fast kinetics for coordination and insertion, a Cossee pathway would produce a Schultz-Flory distribution of oligomers. The active site in our current study is thereby described as a Co oxide phase in general without further clarification, and the investigation of the active site would be a subject of the future study.

The first step in this mechanism is 1-butene adsorption onto the cobalt site. The adsorbed 1-butene can then undergo double bond isomerization to form adsorbed *cis*-2-butene or *trans*-2-butene. As demonstrated in Figure 4, the distribution of 1-butene, *trans*-2-butene and *cis*-2-butene is in equilibrium at longer residence time. Both 1-butene and 2-butene can be bonded to the cobalt center through σ-donating and π-accepting interactions between the olefin ligand and the metal, forming a stable metal-olefin complex [88]. Dimerization occurs via olefin oxidative coupling forming a metallacyclopentane. Our cobaltacyclopentane based pathway has precedence in selective ethylene tri-and tetramerization mediated by chromium [89]. The dimerization can take place in the manner of either head to head or head to tail coupling, thus generating different C8 olefin isomers. The metallacyclopentane then undergoes β-hydrogen shift followed by reductive elimination, yielding the corresponding C8 olefins products, while recovering cobalt in its original oxidation state.

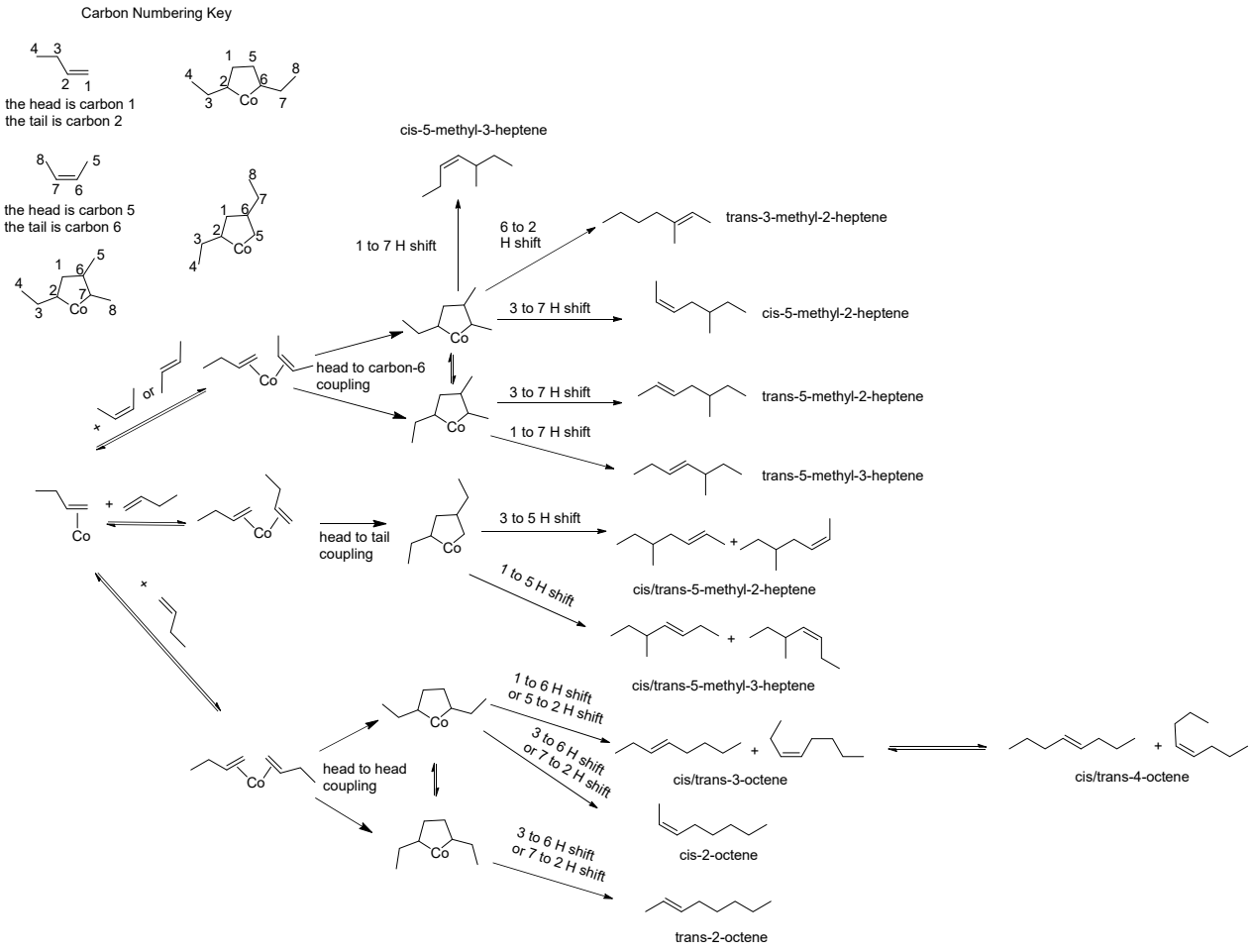

Figure 3.17 Proposed reaction pathway for butene coupling on cobalt oxide on carbon catalyst.

Linear octenes including *cis/trans*-3-octene and *cis/trans*-2-octene can be formed *via* head to head coupling of two 1-butenes. *Cis/trans*-4-octene can then be formed by double bond shift from *cis/trans*-3-octene. Table 3.2 shows the experimental and equilibrium linear octene distribution. The equilibrium distribution of 1-octene is less than 0.83% and no 1-octene could be detected in our product. The 3-octene and *cis*-2-octene are greater than their equilibrium composition at the lowest conversion suggesting that these are the primary products produced by dimerization of the 1-butene. The *cis*-2-octene/*trans*-2-octene ratio is greater than the equilibrium calculated ratio. As residence time increases the products move towards the equilibrium distribution but did not reach equilibrium.

It is proposed that the branched butene dimers including *cis/trans*-5-methyl-2-heptene and *cis/trans*-5-methyl-3-heptene can be produced in two ways: head to carbon-6 coupling between 1-butene and 2-butene, and head to tail coupling between two 1-butenes. We are currently unable to determine the extent to which the two pathways are

operational. *Trans*-3-methyl-2-heptene however, is exclusively produced from head to carbon-6 coupling between 1-butene and 2-butene. Table 3.7 shows the experimental and equilibrium distribution of the methyl heptene species. The thermodynamic terminal-methyl-heptene distribution was less than 1 percent and none of these species were detected in our experiments. The thermodynamic distribution of 3-methyl-3-heptene was 11.5% and no 3-methyl-3-heptene was observed. This indicates that the catalyst cannot isomerize the double bond of the 3-methyl-2-heptene product. The ratio of *cis*/*trans*-5-methyl-3-heptene was 3 times higher than the equilibrium composition but this ratio went towards equilibrium as residence time increased. The ratio of *cis*/*trans*-5-methyl-2-heptene was 10 times higher than the equilibrium ratio but decreased to 3 times with increasing residence time. The ratios of *cis*-5-methyl-3-heptene/*cis*-5-methyl-2-heptene and *trans*-5-methyl-3-heptene/*trans*-5-methyl-2-heptene were 30% and 60% higher than their equilibrium values at the highest conversion, respectively.

Table 3.7 Experimental and equilibrium methyl-heptene distribution (Reaction conditions: 80 ℃, 450 psig).

	CoO_X/N-C-230			**Equilibrium**
WHSV(hr^{-1})	14.14	0.71	0.25	
Conversion (%)	9.77	11.42	29	
cis-5-methyl-3-heptene	10.9	9.8	8.3	3.4
trans- 5-methyl-3-heptene	12.2	11.1	12.5	14.4
trans-3-methyl-2-heptene	21.2	43.6	44.4	33.0
trans-5-methyl-2-heptene	16.7	17.8	19.9	29.4
cis-5-methyl-2-heptene	39.1	17.8	14.8	7.0
3-methyl-3-heptene	0	0	0	11.5
4-methyl-1-heptene	0	0	0	0.7
3-methyl-1-heptene	0	0	0	0.5
cis/*trans* -5-methyl-3-heptene	0.89	0.88	0.67	0.24
cis/*trans* -5-methyl-2-heptene	2.35	1.00	0.74	0.24
cis-5-methyl-3-heptene/ *cis*-5-methyl-2-heptene	1.85	0.41	0.33	0.21
trans-5-methyl-3-heptene/ *trans*-5-methyl-2-heptene	0.73	0.63	0.63	0.49

The abundance of linear octene isomers in the product mixture and the low abundance of 1-butene in the product gas indicate that the reaction between two terminal olefins is faster than the reaction between an internal olefin and a primary olefin. The equilibrium ratio between a primary and internal olefin decreases with increasing size of the

olefin. For example, the equilibrium concentration of 1-butene in butenes isomers is 6.2% while the equilibrium concentration of 1-heptene is less than 0.8%. The absence of C16 and longer olefin products further suggests that the extended chain growth after butene dimerization is prohibited due to the low 1-octene concentration in the mixture, and that the coupling between two internal olefins does not occur. Such features imply that cobalt oxide on carbon catalyst is highly selective for terminal olefin coupling, and could be used as a potential catalyst to make internal linear oligomers with a targeted carbon chain length. Additional studies are underway to enhance our understanding of the active site and transient species.

3.3.5 CoO_X/N-C Catalyst Modification

1. The effect of base treatment on carbon support

It has been hypothesized that the addition of ammonia hydroxide both before and after cobalt impregnation onto the carbon support could have several effects on the state of the active catalytic surface. The PH of the impregnation solution can have profound influence on the catalytic properties, as shown by Bae *et al*. in their work about the Co/γ-alumina catalyst for Fischer-Tropsch synthesis [90], where the solution PH influenced the particle size distribution over γ-alumina support. On an activated carbon support specifically, the surface functional groups can be modified which could affect the adsorption of a reactant molecule, or the formation of various metal sites [91, 92]. To investigate the base treatment effect on the catalytic activity, three catalysts were prepared and tested under the same reaction conditions: non-treated carbon support (CoO_X/C), NH_4OH treated carbon support (CoO_X/N-C), and NaOH treated carbon support (CoO_X/NaOH-C). The NaOH and NH_4OH volume and usage are the same as mentioned in the experimental section previously in this chapter. 1-Butene conversion was then carried out at 80 ℃, 450 psig and 14.14 h^{-1} WHSV, and the oligomer formation rate in the unit of $mol_{carbon}/mol_{Co}/h$, where mol_{Co} represents the overall mole of cobalt in the bulk material with time-on-stream (TOS) is demonstrated below. The CoO_X/N-C catalyst showed 2-3 times higher oligomer formation rate compared to CoO_X/NaOH-C, whereas the non-base treated carbon supported catalyst CoO_X/C showed significantly lower activity.

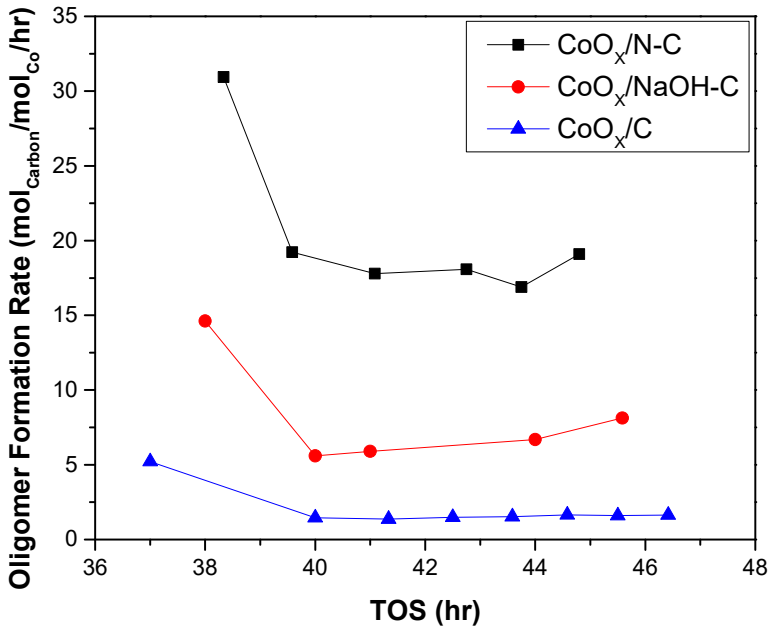

Figure 3.18 Rate of oligomer formation for different bases treated carbon support. Reaction condition: 80 ℃, 450 psig, WHSV=14.14 h^{-1}. All catalysts were pretreated at 270 ℃ in helium.

A detailed octene product distribution comparing the effect of NH_4OH and NaOH treatments is tabulated in Table 3.8. At a similar WHSV of 0.24-0.25 h^{-1}, the oligomer yield (or overall butenes conversion defined in this work) for NH_4OH treated catalyst was twice as high as the NaOH treated catalyst during 1-butene conversion. At a lower oligomer yield of 10.3%, the NaOH treated catalyst achieved a total linear octene distribution of 84.8%. This result is similar to the catalyst pretreated at 230 ℃, where 84.2% total linear octene distribution was achieved at an oligomer yield of 9.77% (

Table 3.1). The base treatment does not change the selectivity feature of the current catalyst, but rather affects the catalytic activity.

Table 3.8 Octene product distribution comparing NH_4OH and NaOH treated catalysts pretreated at 230 ℃ for 2 hr in flowing helium.

Catalyst	CoO_X/N-C	CoO_X/NaOH-C
WHSV(hr^{-1})	0.25	0.24
TOS/hr	37	36
Butenes conversion(%) [a]	29.0	10.3
Total octene distribution(%)	94.2	97.9
Specific C8 olefins distribution(%)		
1-octene	3.21	3.56
cis-2-octene	6.90	11.32
trans-2-octene	19.85	19.69
trans-3-octene	43.90	48.33
trans-4-octene	7.75	3.74
trans-2-methyl-3-heptene	2.69	2.27
2-methyl-1-heptene	0.00	0.00
3-methyl-2-heptene	9.57	5.67
4-methyl-3-heptene	0.00	0.00
5-methyl-2-heptene	0.00	0.00
2,3-dimethyl-2-hexene	0.00	0.00
2,3-dimethyl-3-hexene	0.00	0.00
2,4-dimethyl-2-hexene	4.31	3.57
2,4-dimethyl-3-hexene	0.00	0.00
3,4-dimethyl-2-hexene	0.00	0.00
3,4-dimethyl-3-hexene	1.83	1.85
3,5-dimethyl-2-hexene	0.00	0.00
2,3,4-trimethyl-2-pentene	0.00	0.00
NCB	0.25	0.19
total linear octene selectivity [b]	76.88	84.82
total linear octene distribution[c]	81.61	86.64
Total linear octene yield	22.29	8.74

[a] Butenes conversion (%) = (mols of carbon in the detected products)/(mols of carbon in the feed butene)×100%
[b] Octene selectivity (%) = (mols of carbon in octene)/(mols of carbon in total detected products)× 100%
[c] Total linear octene distribution (%) = (mols of linear octene)/(mols of total octene)×100%

The NH_4OH treatment has also resulted in the change of the metal reduction behavior. A temperature-programmed reduction (TPR) measurement was measured with the catalyst synthesized with and without NH_4OH treatment, and the result is depicted in Figure 3.19.

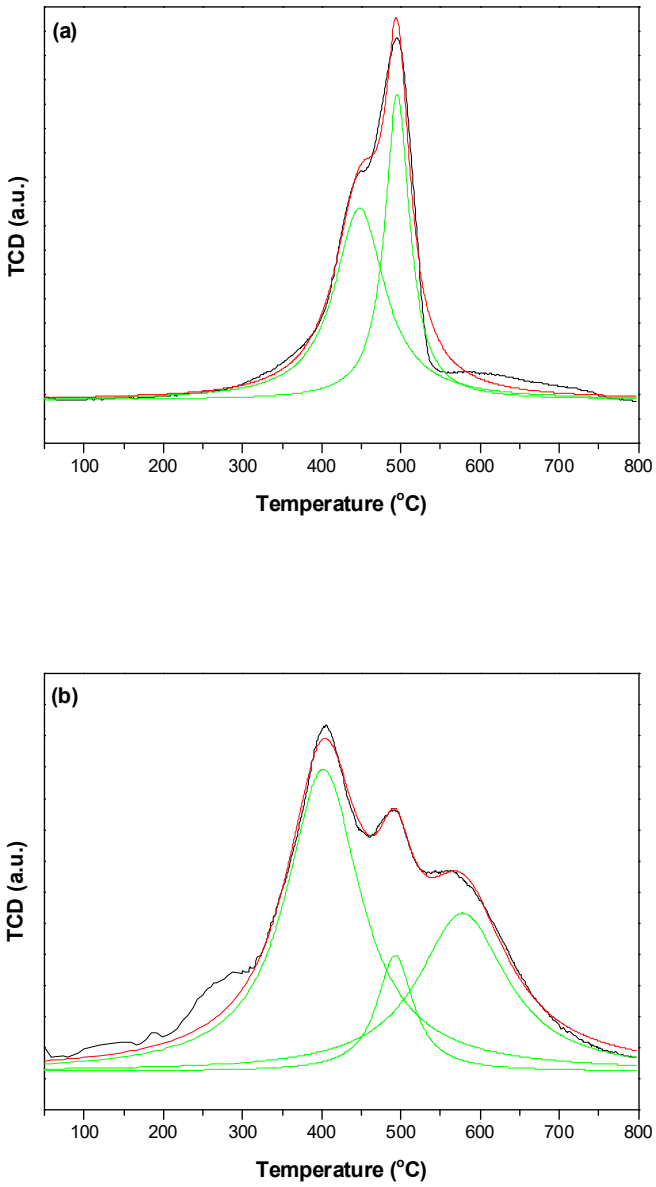

Figure 3.19 TPR analysis of the catalysts after pretreatment in helium at 230 ℃ in helium. The TPR profile of the non-ammonia treated catalyst (CoO_X/C) is depicted in (a) and the TPR profile of the ammonia treated catalyst (CoO_X/N-C) is depicted in (b).

The NH_4OH treatment of the carbon support has introduced N in the functional groups aside from providing a basic PH.

Table 3.9 shows the composition of N and Co as determined by ICP. NH_4OH does increase N composition and supports the theory that a Co-N interaction could increase activity. NaOH enhancement is not related to N

composition, as its N level is similar to the support and non-NH_4OH treated catalysts. However, the N content on the treated catalyst can also arise from the incomplete decomposition of cobalt nitrate. The role of N addition to the catalyst and the effect of the catalyst activity enhancement is subject to future studies.

Table 3.9 N and Co composition as determined by ICP. The experiments were conducted by Galbraith lab.

Catalyst [b]	**Cobalt Loading wt.%**	**N/Co at.% ratio** [a]	**N at.%** [a]
CoO_X/N-C	12.3	0.56	1.56
CoO_X/NaOH-C	9.73	0.42	0.87
CoO_X/C	14.3	0.27	0.78
N-C	0	-	0.83

[a] The value is calculated based on the atomic (molar) basis.
[b] All the catalysts were pretreated at 270 ℃ in flowing helium for 2 hr.

2. The effect of metal precursor

On a similar front, it has been determined that the cobalt on carbon catalyst is sensitive to the cobalt precursor used during synthesis. Figure 3.20 compares the activity of CoO_X/N-C synthesized from cobalt nitrate and cobalt acetate. The amount of the cobalt metal precursor was chosen to ensure the same cobalt loading in both cases. The catalyst synthesized with cobalt nitrate showed significantly higher activity compared to the catalyst synthesized with cobalt acetate.

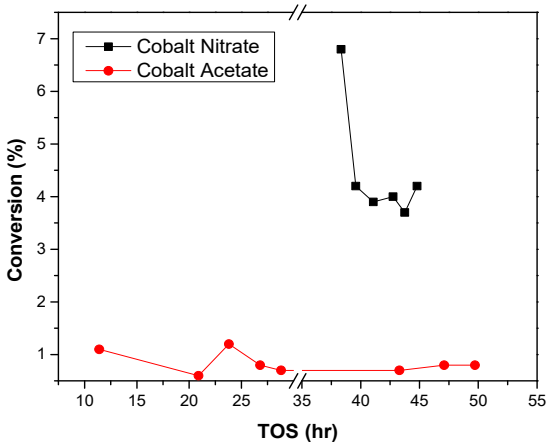

Figure 3.20 Conversion (oligomer yield) with TOS for different cobalt precursors. Reaction conditions: 80 ℃, 450 psig, WHSV=0.11 h^{-1}.

3. The effect of the addition of solid acid catalysts

A physical mixture of as-synthesized CoO_X/N-C with two solid acid catalysts: γ-Al_2O_3 and SiO_2-Al_2O_3 at different ratios were studied with the aim of improving catalytic activity. γ-Al_2O_3 possesses both Lewis and Brønsted acidity with predominantly Lewis acid site catalysis [93], whereas SiO_2-Al_2O_3 has catalysis features involving Brønsted acid sites [94]. Figure 3.21 compares the total butenes conversion over three different mixtures with the pure CoO_X/N-C catalyst. All the catalysts were packed and pretreated at 270 ℃ prior to the reaction. The reaction temperature and pressure were kept at 80 ℃ and 450 psig, respectively. The ratios reported in the figure is based on mass fraction. The 1:1 mixture of CoO_X/N-C and SiO_2-Al_2O_3 demonstrated the highest oligomer yield of about 95% at 0.40 h^{-1} WHSV. At steady state, the 1:1 mixture with γ-Al_2O_3 did not show any enhancement in activity compared to pure CoO_X/N-C, and the selectivity towards linear octene products remains almost unchanged. When comparing activity, it appears that the addition of SiO_2-Al_2O_3 is effective in improving the conversion. However, the 10:1 mixture showed a relatively faster deactivation compared to pure CoO_X/N-C.

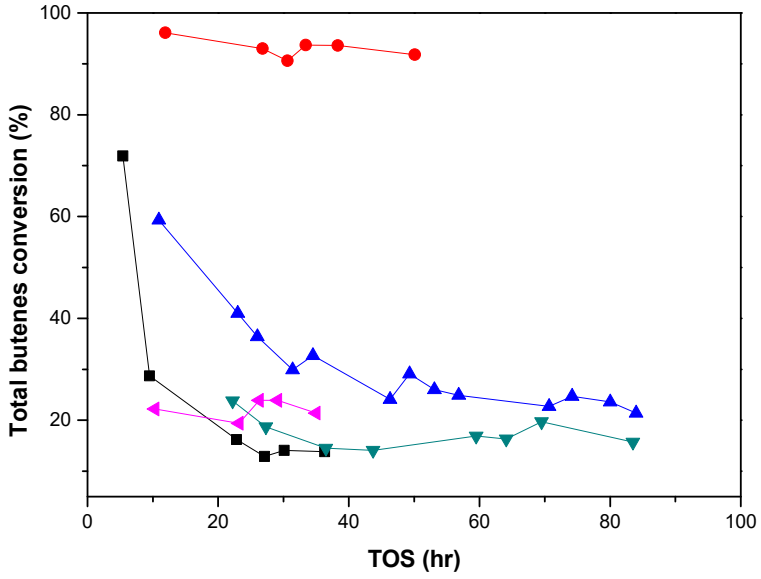

Figure 3.21 1-butene conversion activity comparison of 1:1 mixture with γ-Al2O3 at 0.40 h^{-1} WHSV (■), 1:1 mixture with SiO_2-Al_2O_3 at 0.40 h^{-1} WHSV (●), 10:1 mixture with SiO_2-Al_2O_3 at 0.22 h^{-1} WHSV (▲), pure CoO_X/N-C at 0.04 h^{-1} WHSV (▼), and pure CoO_X/N-C at 0.25 h^{-1} WHSV (◀).

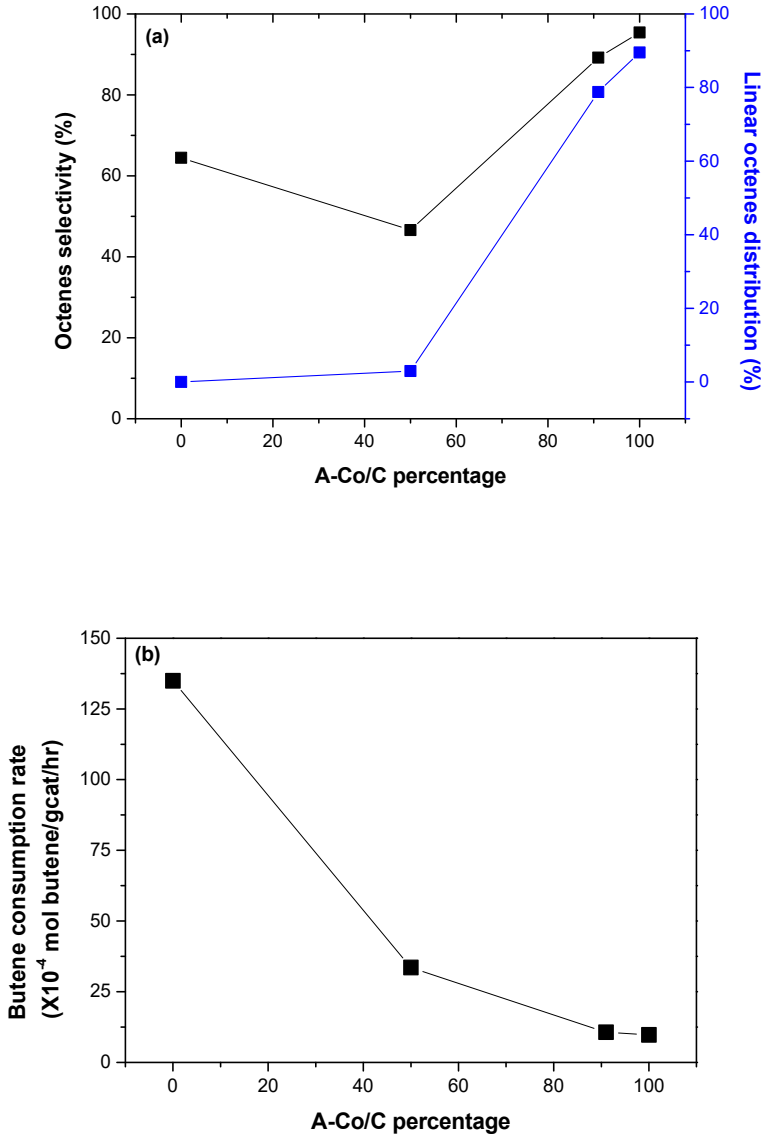

Figure 3.22 Top: overall octene product selectivity and linear octene distribution with various CoO_X/N-C compositions mixed with SiO_2-Al_2O_3. Bottom: butene consumption rate with various CoO_X/N-C compositions mixed with SiO_2-Al_2O_3.

The selectivity and activity of the CoO_X/N-C & SiO_2-Al_2O_3 mixtures as depicted in Figure 3.22 indicate that the addition of SiO_2-Al_2O_3 increased the activity for 1-butene oligomerization with an increased yield of branched octene products. This result implies that the Brønsted acidity brought in from SiO_2-Al_2O_3 catalyzes more 1-butene conversion based on a carbocation reaction pathway that produces more branched oligomers. The physical mixture

studies of CoO_X/N-C with the solid acid catalysts showed that the kinetic results obtained are due to the additive effects from both the cobalt site and the Brønsted acid sites.

4. The effect of carbon support

Both active carbon and carbon black have been used as catalyst support in various applications [95, 96]. Carbon as a catalyst support has combined the advantage of offering high BET surface area (200-2000 m^2/g) and hydrothermal stability. The difference in the physical properties and surface chemistry of the carbon support could influence the dispersion and surface composition of the supported nanoparticles, thus affecting the catalytic performance. For example, Karanjkar *et al.* have observed a two orders-of-magnitude higher rate in hydrogenolysis of tetrahydropyran-2-methanol with a Vulcan XC-72 (VXC) carbon supported bimetallic RhRe catalyst as compared to that supported with a Norit Darco 12X40 (NDC) carbon. The authors concluded that the bimetallic particles on the former are relatively uniform in composition whereas those on the latter are composed of either tiny Rh-rich particles or larger bimetallic particles with a higher than design Re content. The particles formed on the NDC carbon were proven to be inactive for the hydrogenolysis reaction [97]. Cobalt oxide supported on both carbon supports were synthesized and tested for 1-butene conversion to investigate the effect of different surface functional groups on the carbon support have on oligomerization.

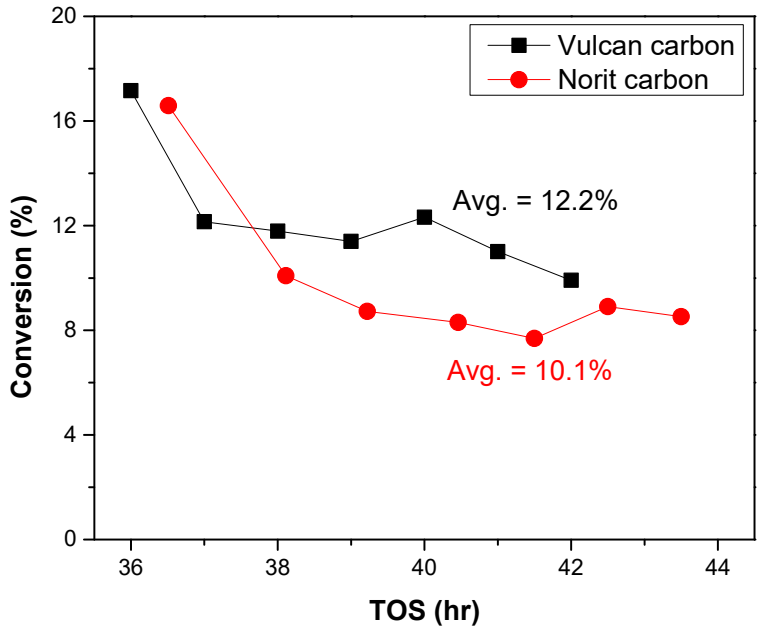

Figure 3.23 1-butene conversion over CoO_X/N-C supported on (■) VXC and (●) NDC. Reaction conditions: 80 ℃, 450 psig, 14.1 h^{-1} WHSV. The average total butenes conversion for each catalyst is calculated and listed in the figure.

The activity of the CoO_X/N-C supported by both carbons is compared and demonstrated in Figure 3.23. The difference in the activity observed with both catalysts is within error. The result suggested that the carbon matrix and surface structure do not have an effect on the catalytic performance for the CoO_X/N-C catalyst during light olefin oligomerization.

5. *The effect of weight hourly space velocity*

The activity of the CoO_X/N-C catalyst was tested at various weight hourly space velocities in the range between 0.04 and 24.67 h^{-1}. The WHSV is adjusted by varying the total catalyst loading in the fixed-bed reactor. The consumption rate is evaluated based on the total gram of cobalt loaded into the reactor and plotted together with average conversion against WHSV and shown in Figure 3.24. There is no strict positive correlation between the WHSV and the conversion, especially when below 0.25 h^{-1} WHSV was achieved. In order to achieve 0.04 h^{-1} WHSV, 13.11 g catalyst was packed into a ½" tube. A significant pressure drop was observed at 0.25 h^{-1} WHSV,

where mass and heat transfer limitation were more likely to occur. The highest total butenes conversion achieved by varying the WHSV is thus limited to 25%.

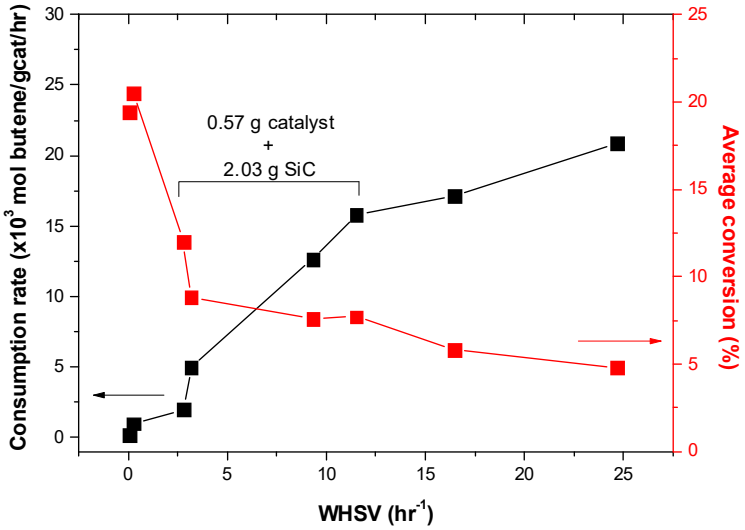

Figure 3.24 1-Butene consumption rate together and average total butenes conversion with WHSV.

3.4 Conclusions

Cobalt oxide on carbon catalysts have greater than 80% selectivity towards linear octenes for 1-butene oligomerization. The 1-butene undergoes double bond isomerization to form an equilibrium mixture with *trans*- and *cis*-2-butene at high conversion. The main linear oligomers from butene conversion with a decreasing order of distribution are 3-octene > 2-octene > 4-octene. These internal linear octenes are formed from head to head coupling of two 1-butene molecules. The linear octenes approach equilibrium with increasing conversion. All the methyl-heptene products can be formed through head to tail coupling of two 1-butene molecules. Trans/cis-5-methyl-2-heptene and trans/cis-5-methyl-3-hetptene can also be formed through the coupling between 1-butene and 2-butene molecules. A detailed reaction mechanism regarding to light olefin conversion with cobalt oxide on carbon catalyst however, is subject to further studies as will be discussed in the chapter that follows. The activity of the catalyst increases with increasing Co_3O_4 content. The cobalt composition change was monitored by in situ Raman and TGA, which shows that cobalt nitrate fully decomposes at about 200 ℃, and forms overlapped Co_3O_4 and CoO particles,

as shown in the XANES, XRD and HRTEM results. XANES result confirms that high pretreatment temperature (550 ℃) in helium partially reduced the cobalt oxide to metallic cobalt, with a decreasing Co_3O_4 content. The cobalt oxide on carbon catalysts described in this chapter are highly selective for terminal olefin coupling and can be used to make internal linear oligomers with a targeted carbon chain length.

The highest oligomer yield that can be achieved by adjusting the pretreatment temperature of the catalyst precursor is 29.00% at a WHSV of 0.25 h^{-1}. The catalyst also suffered from deactivation especially at high WHSVs. The results indicate that the activity and stability of the current CoO_X/N-C catalyst has the potential to be further improved.

The NH_4OH-treated carbon supported cobalt oxide catalyst showed enhanced catalytic activity compared to the NaOH-treated and non-based treated carbon supported cobalt catalyst. The NH_4OH treatment could have introduced two effects: 1) modified the PH of the surface of the carbon support and strengthened the interaction between the metal precursor and the support; 2) introduced N-containing surface functional groups that stabilized the active cobalt species. Cobalt nitrate appears to be the metal precursor that could give the highest catalytic activity. Cobalt acetate showed declined activity under the same synthesis and reaction conditions. The addition of a secondary solid acid catalyst into the CoO_X/N-C did not show any effect on the catalytic performance of CoO_X/N-C. The activity and selectivity of CoO_X/N-C also do not seem to be influenced by the matrix and morphology structure of the carbon support. The catalyst showed potential mass and heat transfer limitation at low WHSV.

CHAPTER 4 CoO_X/N-C-230 Catalyst: Effect of Feedstock

Zhuoran Xu, Dongting Zhao, Joseph P. Chada, Devon C. Rosenfeld, Jessica L. Rogers, Ive Hermans, George W. Huber. Olefin Conversion on Nitrogen-doped Carbon-Supported Cobalt Catalyst: Effect of Feedstock, *Journal of Catalysis*, 2017, 354, 213-222.

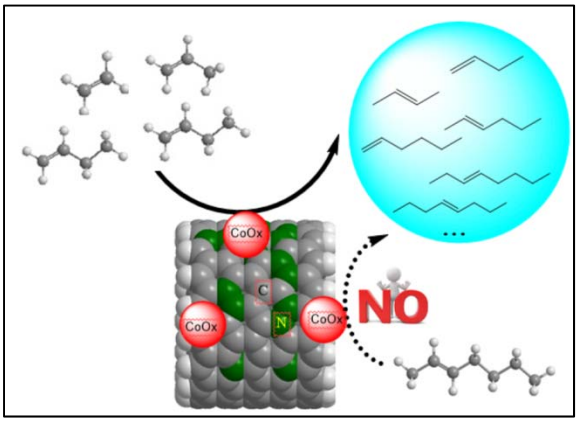

4.1 Introduction

Light (C2 to C6) linear alpha olefins are important building blocks for the synthesis of fuels and chemicals. The IFP-SABIC Alphabutol technology was implemented to produce 1-butene with the world's largest capacity from ethylene dimerization based on homogeneous catalysis [98]. Chevron Phillips Chemical has announced the start-up of world's largest 1-hexene plant in 2014 [6], which adopts an on purpose route to 1-hexene from ethylene trimerization with a chromium based homogenous catalyst. The light olefins are currently largely produced from steam cracking [99], fluid catalytic cracking (FCC) [100] and Fischer-Tropsch synthesis (FTS) [101]. The shale gas revolution has driven ethylene expansions in the North American market with a 70% collapse in the price of ethane between 2012 and 2013 [102]. The catalytic oligomerization of light olefin can be achieved by heterogeneous acid-catalysis which mainly produces branched oligomers suitable as additives for fuels or synthetic lubricants [18, 103], or by homogeneous catalytic systems which mainly produce straight-chain oligomers to make commodity chemicals [104]. Linear oligomers, especially linear alpha olefins (LAO) have a broad range of applications in the production of performance chemicals and plastics such as polybutylene, co-monomers in PE/PP, polyolefin elastomers, plasticizer and detergent alcohols. Olefin oligomerization to LAOs remains one of the few industrial processes that use homogeneous catalysts [7, 62, 105-107]. The technology uses an expensive and difficult-to-handle co-catalyst activator such as methylaluminoxane (MAO) [108], complex catalyst recovery operations, and a highly purified olefin feed stream [109]. Replacing homogeneous catalysts with an efficient heterogeneous analogue that is potentially regenerable, does not require addition of an activator and is resistant to feed impurities could drastically lower the capital and operating costs, and hence improve the competitiveness of the US chemical industry.

Olefin oligomerization has been proposed to proceed through three different classes of mechanisms: carbocation, metallacycle or Cossee-Arlman. A carbocation mechanism is used to describe olefin oligomerization catalyzed by inorganic solid acid catalysts such as H-zeolites and solid phosphoric acid [18, 26, 110]. This pathway involves the formation of a secondary or tertiary carbocation over Brønsted acid sites yielding branched oligomers. The formation of highly linear oligomers catalyzed by transition metal complexes is commonly explained by a metallacycle or Cossee-Arlman mechanism. The metallacycle mechanism begins with olefin coordination followed by formation of metallacyclopentane [111]. The product selectivity is frequently determined by the stability of the intermediate metallacycles. This mechanism was proposed to rationalize the excess amount of 1-hexene product observed during ethylene oligomerization over chromium-based N-heterocyclic carbene (Cr-NHC) catalysts,

through both experimental [111-113] and computational [114] methods. The Cossee-Arlman mechanism involves alkyl migration to a coordinated olefin where the rate constants for chain propagation and chain termination are approximately the same [112]. This mechanism was originally proposed to explain the chain growth for ethylene polymerization over Ziegler-Natta catalysts [1]. It has been lately adopted to explain the product selectivity over transition metal complexes including tridentate cobalt and iron catalysts [112, 115], and cobalt metallocene [116] catalyst. A recent theoretical study also provided evidence to describe the oligomer chain growth on the Ni sites within Ni-containing SSZ-24 zeolite during ethylene oligomerization with a Cossee-type mechanism [117].

Schultz and co-workers proposed that olefin oligomerization for CoO_X/N-C catalysts (pretreated at 543 K) occurs by a Cossee-type mechanism, using ethylene, propylene, 1-butene and 1-hexene as feeds [21, 75, 118]. However, their experiments were not performed in a continuous flow reactor and they did not analyze the location of the C=C bond making it difficult to probe the chain growth. We reported the use of two-dimensional gas chromatography-mass spectrometry (2D-GC/MS) to accurately identify and quantify most of the octene isomers formed in 1-butene oligomerization [119]. Oligomerization with other olefinic feeds, besides 1-butene, could aid in developing a better understanding of olefin oligomerization over CoO_X/N-C.

In the previous chapter, we have proposed that 1-butene oligomerization follows a metallacyle mechanism on nitrogen-doped carbon-supported cobalt oxide (CoO_X/N-C) catalysts [119]. While this mechanism can explain the product distribution for 1-butene oligomerization at low conversion as we will show in this paper a Cossee-type mechanism better explains the product distribution for different olefins over this catalyst at all conversions. The objective of Chapter 4 is to report on the oligomerization of ethylene, propylene, 1-butene, 1-hexene and 1-hexene/internal hexene mixtures with CoO_X/N-C in a continuous flow reactor. This will allow us to develop a more rigorous mechanism for how olefins oligomerize over this catalytic material.

4.2 Experimental Section

4.2.1 Catalyst Preparation

A nitrogen-doped carbon-supported cobalt oxide catalyst (CoO_X/N-C) was prepared as described in Chapter 3. In a typical synthesis, 5.0 g of sieved activated carbon was treated with 4.55 mL 30% NH_4OH solution and dried on a

hot plate in the open air at 403 K for 2 h. A cobalt nitrate solution of 4.66 g $Co(NO_3)_2 \cdot 6H_2O$ in 5.83 mL deionized water was then added onto the treated carbon support to achieve a cobalt loading of 13 wt.%. After drying at 403 K overnight, the catalyst was treated with 12.5 mL 30% NH_4OH solution. Finally, the catalyst was dried overnight at 403 K. The carbon-supported cobalt oxide catalyst was pretreated at 503 K for 2 h in helium without air exposure before being exposed to the olefin substrate for oligomerization testing. Catalyst characterization (including elemental analysis, XRD, *in-situ* Raman and XANES) can be found in Chapter 3.

NH_4-ferrierite (NH_4-FER; SiO_2/Al_2O_3 = 20, CP914C) was purchased from Zeolyst. The NH_4-FER catalyst was used directly for terminal/internal hexene mixture synthesis without any pretreatment.

4.2.2 Catalyst Characterization

Powder X-ray diffraction (pXRD) patterns were obtained from Rigaku Rapid II diffractometer with a Mo K_α source with 2θ from 2^o to 45^o and a total exposure time of 20 min. Samples were crushed and packed in glass capillaries with a 0.8 mm diameter and 0.01 mm wall thickness.

Thermogravimetric analysis (TGA) was carried out with a TA instruments Q500 system. Approximately 10 mg of sample was used. Measurements were performed in 50 mL/min N_2 flow with 10 K/min ramp rate from room temperature to 1073 K. The catalyst samples were cooled down after reaction in the reactor under 50 mL/min helium flow till room temperature, and remained in the reactor for at least 12 h before exposure to the air prior to the TGA experiments.

Nitrogen Brunauer-Emmett-Teller (BET) surface areas were obtained at 77 K with ASAP 2020 multiple points system (Micromeritics). Before the measurements, the sample was degassed under vacuum at 423 K for 4 h.

4.2.3 Catalyst Activity and Selectivity

Measurements of reaction rates and product distributions were performed using a down-flow, fixed-bed stainless steel reactor (9.52 mm outer diameter, 1.24 mm wall thickness) loaded with 500 mg of catalyst, with both ends capped with glass beads (Sigma-Aldrich, 425-600 μm) and quartz wool. All experiments were carried out at 353 K and 31 bar total pressure, which was adjusted with helium (Airgas, UHP) using a back-pressure regulator. After a gas-liquid separator maintained at 268 K and reaction pressure, the gas phase products were analyzed with an online

gas chromatograph (GC, Shimadzu) equipped with a Rt®-QS-BOND (Restek) and a flame ionization detector (FID). The liquid products were collected from the separator and analyzed by 2D-GC/MS (Agilent) equipped with both a flame ionization detector (FID) and a mass selective detector (MSD). A more detailed description about the reactor system and the GC operation condition can be found elsewhere [18, 119]. The linear alpha olefin feeds in this study include: ethylene (UHP, Airgas), propylene (99.5% polymer grade, Airgas), 1-butene (99.9%, Matheson) and 1-hexene (97%, Sigma-Aldrich). For all the oligomerization experiments, the catalyst was pretreated in 150 mL/min helium flow, ramped to 503 K with 5.5 K/min ramp rate, and held at 503 K for 2 h. The reactor was then cooled to the reaction temperature (353 K) in helium flow. Reactant conversion was calculated based on Equation 4.1. Product selectivity, product yield, rate and product distribution were calculated based on Equation 4.2-4.5. Weight hourly space velocity is defined and calculated based on Equation 4.6. The overall turnover number (TON) is defined as the moles of carbon in the total observed products per mole of cobalt atom in the catalyst as shown in Equation 4.7.

Equation 4.1 Reactant conversion (%) = $\frac{\textbf{\textit{moles of carbon in the detected products}}}{\textbf{\textit{moles of carbon in the feed}}} \times 100\%$

Equation 4.2 Product selectivity (%) = $\frac{\textbf{\textit{moles of reactant converted to a specific or a group of product}}}{\textbf{\textit{moles of reactant converted}}} \times \mathbf{100}\%$

Equation 4.3 Product yield (%) = Product selectivity × Reactant conversion/100

Equation 4.4 Product distribution (%) = $\frac{\textbf{\textit{moles of carbon in a specific group of product with a carbon number of i}}}{\textbf{\textit{moles of carbon in the product with a carbon number of i}}} \times 100\%$

Equation 4.5 Rate (mol C/h) = Reactant conversion × Feed carbon inlet flowrate

Equation 4.6 Weight hourly space velocity (WHSV, h^{-1}) = $\frac{\textbf{\textit{hourly mass feed flowrate}}}{\textbf{\textit{catalyst mass}}} \times \mathbf{100}\%$

Equation 4.7 Turnover number (mol_{carbon}/mol_{Co}) = $\frac{\textbf{\textit{feed carbon inlet flowrate}} \times \int \textbf{\textit{conversion}} \cdot \textbf{\textit{dt}}}{\textbf{\textit{moles of cobalt atom in the catalyst}}}$

An internal hexene mixture was prepared in a 300 mL stainless steel Parr reactor. For a typical reaction, 500 mg of NH_4-FER was reacted with 80 mL 1-hexene (97%, Sigma-Aldrich) at 473 K, 290 psig with 470 rpm stirring speed overnight. The product was then allowed to cool, and the solid catalyst was removed by vacuum filtration. The product composition was analyzed by 2D-GC/MS.

4.3 Results and Discussion

4.3.1 Conversion of Terminal Olefins

The reaction data during the conversion of ethylene, propylene, 1-butene and 1-hexene at the initial time-on-stream (2 h TOS) is tabulated in Table 4.1. A WHSV of 14.1 h^{-1} was used for all experiments in Table 4.1. Ethylene was diluted with 50% helium, whereas all the other olefins were pure feeds. Reactions with 1-butene and 1-hexene were in the liquid phase, while reactions with propylene and ethylene were in the gas phase. An ethylene feed concentration of greater than 1.62 mol/L led to clogging of the reactor by oligomerization. Initially, ethylene had the highest oligomer yield followed by 1-hexene, propylene and 1-butene. The observed activity order is the result of both the difference in the inlet feed concentration and the intrinsic activity of each olefin feed. The higher overall conversion for 1-hexene compared to 1-butene might be due to the more negative heat of adsorption (1-butene: 7.17 kcal/mol; 1-hexene: 12.3 kcal/mol) of 1-hexene on cobalt oxide [120].

Ethylene and propylene only produced oligomers while 1-butene and 1-hexene produced both oligomers and isomers. The oligomer selectivity for 1-butene and 1-hexene was 19.7% and 19.5%, respectively. At the conditions used in Table 4.1, the butene and hexene isomers were far from equilibrium, as indicated by the $(t/i)_{reaction}/(t/i)_{equilibrium}$ values.

Table 4.1 Oligomerization of ethylene, propylene, 1-butene and 1-hexene over CoOX/N-C at 14.1 h-1 WHSV, 353 K and 31 bar

Feed	Ethylene (gas-phase)	Propylene (gas-phase)	1-butene (liquid-phase)	1-hexene (liquid-phase)
Critical point	282.5 K, 50.6 bar	364.2 K, 45.5 bar	419.3 K 40.0 bar	504 K 31.6 bar
Inlet feed concentration[a] (mol/L)	0.81	1.61	9.22	7.48
Outlet feed concentration[a] (mol/L)	0.53	1.57	4.43	0.47
$(t/i)_{reaction}/(t/i)_{equilibrium}$[b]	-	-	16.83	4.95
Feed conversion (%)	39.36	16.41	53.39	93.80
Oligomer selectivity (%)	100	100	20.58	17.87
Isomer selectivity (%)	-	-	79.42	82.13
Oligomer yield (%)	39.36	16.41	10.99	16.76
Carbon balance (%)[c]	95.1±5.08	96.4±3.52	94.5±4.53	96.5±4.09

[a] The inlet and outlet concentration is reported at the reaction conditions.
[b] The value is calculated from the equation: $(\text{terminal feed/internal feed})_{reaction}/(\text{terminal feed/internal feed})_{equilibrium}$ at the reaction conditions.
[c] Carbon balance was measured and averaged across the entire TOS being tested.

All feeds deactivated the catalyst increasing number of turnovers as shown in Figure 4.1. Propylene showed the most rapid deactivation with a total TON of 250 mol_{carbon}/mol_{Co}, while ethylene reached a conversion of about 20% at TON of 963 mol_{carbon}/mol_{Co}. Propylene is less active in the gas phase than all the other olefin feeds under the reaction conditions. 1-hexene deactivated more rapidly than 1-butene in the liquid phase at much higher TONs at the similar level of overall feed conversions, most likely due to the deposition and accumulation of the hydrocarbon products on the catalyst surface. The pXRD pattern of the spent catalyst showed no variation in the Co_3O_4 phase or Co_3O_4 crystallite size after reaction from the four olefin feeds (Figure 4.2). There were different levels of BET surface area loss observed from the four spent catalysts (Table 4.2), which could be attributed to olefin accumulation that caused catalyst deactivation.

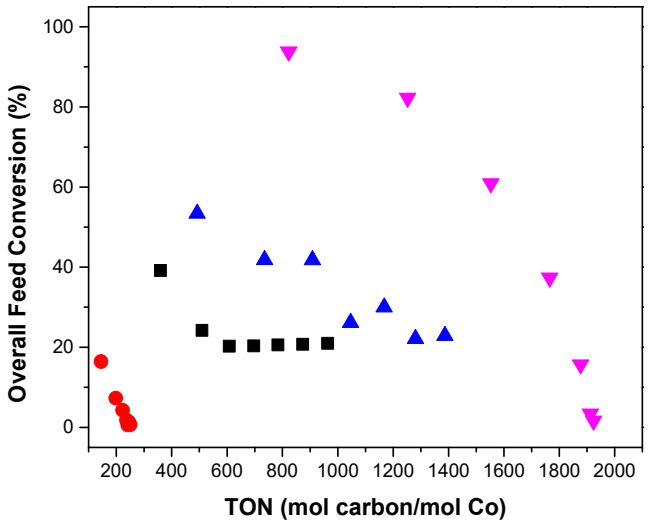

Figure 4.1 Feed conversion of ethylene (■), propylene (●), 1-butene (▲) and 1-hexene (▼) with the number of turnovers (TON). Reaction condition: 353 K, 31 bar, 14.1 h^{-1} WHSV. Ethylene is diluted with helium (50%).

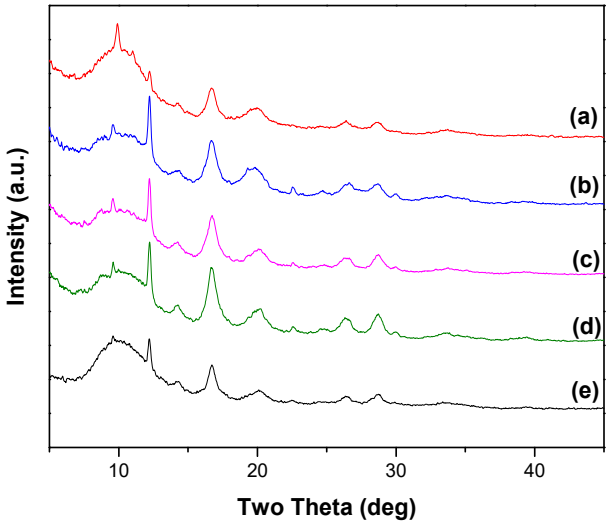

Figure 4.2 PXRD patterns of the spent catalysts after ethylene (a), propylene (b), 1-butene (c), 1-hexene (d) oligomerization reaction together with the fresh catalyst sample (e).

Table 4.2 BET surface area for the fresh and spent catalysts after 8 h TOS.

Sample	BET surface area (m^2/g)
Fresh catalyst	320.8
Spent catalyst after ethylene conversion	19.9
Spent catalyst after propylene conversion	87.8
Spent catalyst after 1-butene conversion	217.6
Spent catalyst after 1-hexene conversion	161.4

The butene and hexene isomer distribution with TON are shown in Figure 4.3. The isomerization of 1-butene and 1-hexene includes double bond shift to form internal olefins. No skeletal isomerization occurred during the reaction. 2-hexene and 3-hexene isomers were inseparable in the 2D-GC and were grouped together. The composition of both 1-butene and 1-hexene deviated from their corresponding equilibrium compositions with increasing TON, which indicates a deactivation of the isomerization activity. At the same time, the oligomer yield declined with TON. No shift of the product selectivity was observed during the reaction. The results imply that the oligomerization and isomerization reaction occurred in parallel and both deactivated in a similar manner.

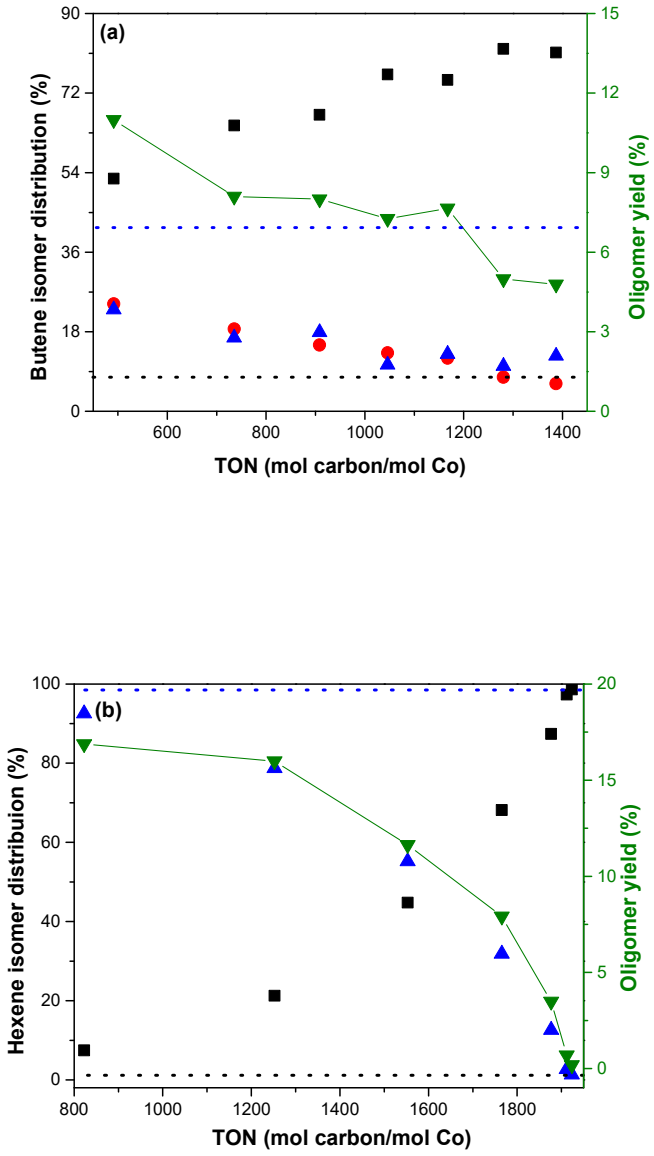

Figure 4.3 Olefin isomer distribution for (a) 1-butene conversion (key: 1-butene (■), *trans*-2-butene (●), *cis*-2-butene (▲), and oligomer yield (▼)) and (b) 1-hexene conversion (key: 1-hexene (■), 2- and 3-hexene (▲), and oligomer yield (▼)). Reaction condition: 353 K, 31 bar, 14.1 h^{-1} WHSV. Equilibrium distribution shown by dotted lines.

4.3.2 Detailed Oligomer Selectivity

The overall product selectivity at early TOS for ethylene and propylene oligomerization is summarized in Table 4.3. After a TON of 607 mol_{carbon}/mol_{Co} was reached at 20% conversion of ethylene the catalyst delivered over 91% overall selectivity to dimers with the most abundant product being 1-butene with 56.1% overall selectivity. The overall 1-butene selectivity increased to 87.0% when the total ethylene conversion decreased to about 10% (Figure 4.4, Table 4.5). At 20% ethylene conversion the trimer products are predominantly linear hexenes (7.1%) with the remaining 0.2% 3-methyl-1-pentene. There are only two types of oligomer carbon chain structures observed for ethylene tetramers: linear octenes and mono branched heptenes (3- or 5-methyl) made in slightly less than 1% overall selectivity. The most abundant tetramer product is 3-octene, followed by 5-methyl-2-heptene. The linear tetramer distribution (linear tetramers divided by total tetramers, Equation 4.4) from ethylene oligomerization is 77.6%.

Table 4.3 Product selectivity for ethylene and propylene oligomerization.

Ethylene oligomerization [a]				**Propylene oligomerization [b]**	
Dimer Products (91.4%)		**Trimer products (7.3%)**		**Dimer products (99.9%)**	
1-butene	56.1	1-hexene	5.3	4-methyl-1-pentene	3.1
trans-2-butene	19.0	2- &3-hexene	1.8	4-methyl-2-pentene	45.8
cis-2-butene	16.3	3-methyl-1-pentene	0.2	1-hexene	5.4
Tetramer (C8 olefin) products (0.9%) (Table 4.4)				2&3-hexene	45.7
Pentamer (C10 olefin) products (0.3%)					
Hexamer (C12 olefin) products (0.1%)					

[a] Ethylene oligomerization reaction condition: 353 K reaction temperature, 31 bar total pressure, 14.1 h^{-1} WHSV, 4.43 h time on stream.
[b] Propylene oligomerization reaction condition: 353 K reaction temperature, 31 bar total pressure, 14.1 h^{-1} WHSV, 2.00 h time on stream.

Table 4.4 Detailed ethylene tetramer product distribution (%) at 4.43 h TOS.

Tetramer products	**Distribution (%)**
1-octene	5.2
cis-2-octene	4.5
trans-2-octene	9.9
3-octene	58.0
cis-5-methyl-3-heptene	0.7
trans-5-methyl-3-heptene	2.2
cis-5-methyl-2-heptene	7.0
trans-5-methyl-2-heptene	10.8
trans-3-methyl-2-heptene	1.7

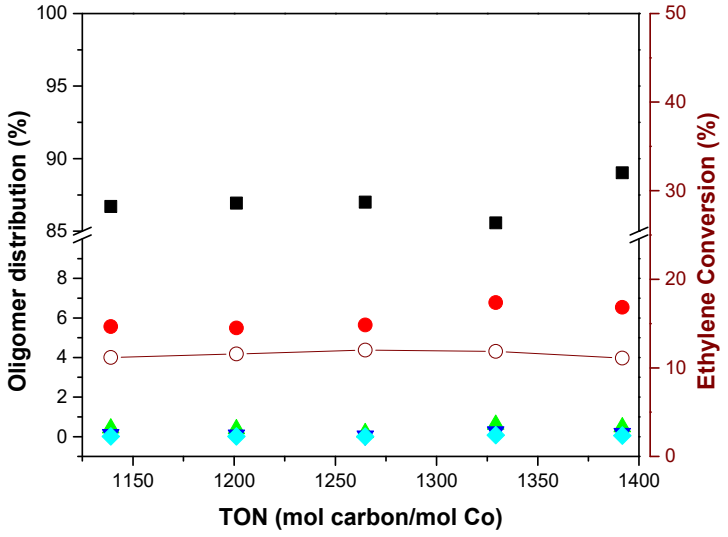

Figure 4.4 Oligomer product distribution with time on stream for ethylene oligomerization including: butene (■), hexene (●), octene (▲), decene (▼) and dodecene (◆), together with ethylene conversion (○) at ethylene conversion around 10%.

Table 4.5 Product selectivity for ethylene oligomerization at around 10% ethylene conversion.

Dimer Products (94.1 %)		**Trimer Products (5.6%)**	
1-butene	87.0	1-hexene	1.6
trans-2-butene	3.3	2- &3-hexene	3.4
cis-2-butene	3.9	3-methyl-1-pentene	0.7
Tetramer Products: 0.2%			

The product distribution from 1-butene and 1-hexene conversion is summarized in Table 4.6. At the current reaction conditions, both 1-butene and 1-hexene were isomerized into linear internal isomers with above 80% selectivity. It should be noted that, during 1-butene conversion, the observed mono-methyl branched dimer products were the same as the tetramer products from ethylene oligomerization, where *trans/cis*-5-methyl-3-heptene, *trans/cis*-5-methyl-2-heptene and *trans*-3-methyl-2-heptene were exclusively observed. During 1-hexene conversion, at least fifteen different C12 dimer species were observed. The most abundant of these C12 species were identified as a mixture of linear internal dodecene (13.1% selectivity) by MS.

Table 4.6 Product selectivity for 1-butene and 1-hexene oligomerization and isomerization.

1-butene oligomerization [a]				**1-hexene oligomerization [b]**			
Butene isomer (79.4%)		**Dimer Products (20.2%)**		**Hexene isomer (82.1%)**		**Dimer products (17.9%)**	
trans-2-butene	42.4	*cis*-2-octene	2.1	2-&3-hexene	82.1	linear	13.9
cis-2-butene	37.0	*trans*-2-octene	3.8			branched	4.0
		3-octene	10.3				
		4-octene	0.6				
		cis-5-methyl-3-heptene	0.4				
		trans-5-methyl-3-heptene	0.4				
		cis-5-methyl-2-heptene	1.1				
		trans-5-methyl-2-heptene	0.6				
		trans-3-methyl-2-heptene	0.9				
		Trimer (C12 olefin) products (0.3%)					

[a] 1-butene oligomerization reaction condition: 353 K reaction temperature, 450 psi total pressure, 14.1 h^{-1} WHSV, 2.10 h time on stream.
[b] 1-hexene oligomerization reaction condition: 353 K reaction temperature, 450 psi total pressure, 14.1 h^{-1} WHSV, 2.00 h time on stream.

Figure 4.5(a) shows the oligomer distribution and ethylene conversion based on TON. Oligomers of carbon number up to twelve were observed in the product stream. The ethylene conversion decreased from 39.2% to 20.3% before 607 mol_{carbon}/mol_{Co} TON. Between 359 and 963 mol_{carbon}/mol_{Co} TON (the 7 h TOS tested), the trimer product increased in distribution from 1.5% to 7.0%, along with a slight increase in the tetramer product compensated by a decrease in the dimer product. A zoomed-in version for a better display of octene, decene and dodecene distribution can be found in Fig S3.

The average oligomer distribution between 607 and 963 mol_{carbon}/mol_{Co} TON from ethylene oligomerization is presented in Figure 4.5(b) based on Schulz-Flory distribution (Equation 4.8), where W_n is the mass fraction of the species with carbon number n, and α represents chain growth probability. The standard error for each data point is negligible (below 0.05) thus is not shown in the figure. A Schulz-Flory distribution was initially applied to describe the formation of hydrocarbon chain formed in a step-wise manner where the insertion or addition of the monomer proceeds with a constant growth probability [121, 122]. Schulz-Flory distribution was seen in light olefin oligomerization processes with nickel, aluminum, aluminum/zirconium or zeolite catalysts [18, 62, 123, 124]. Such oligomerization processes are often described as non-selective where the distribution of the oligomer is closely related to its carbon number. Figure 4.5(b) illustrates that the CoO_X/N-C catalyst was able to oligomerize ethylene based on a non-selective pathway that yields oligomers following Schulz-Flory distribution with a chain growth probability α = 0.37.

The low chain growth probability observed for this catalyst indicates its potential application to produce oligomer-range olefins with up to trimers from ethylene conversion.

Equation 4.8 $\log\left(\frac{W_n}{n}\right) = n\,log\alpha + \beta$

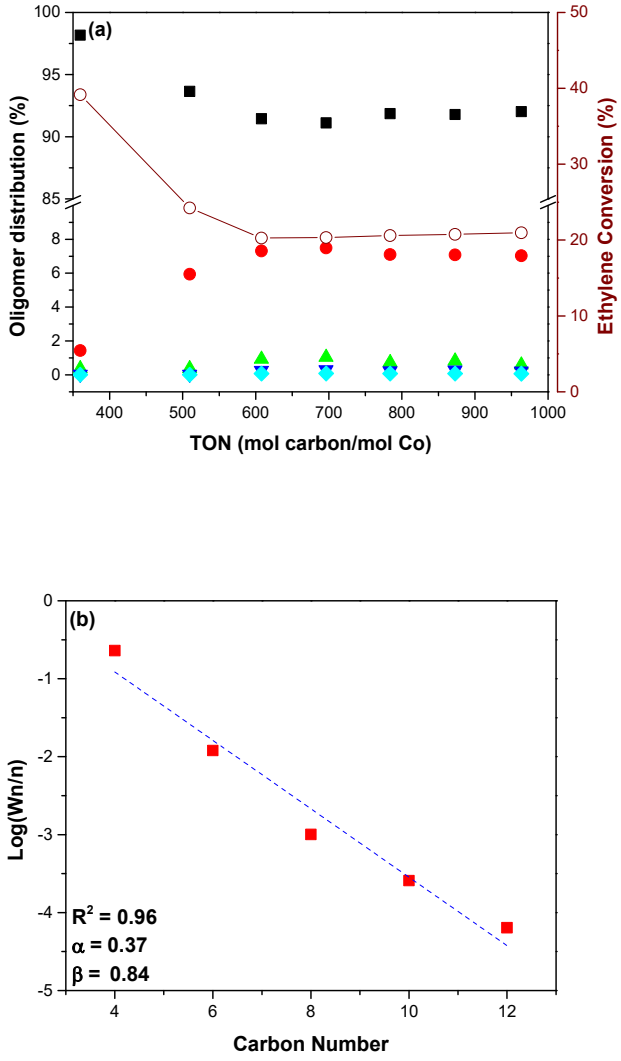

Figure 4.5 (a) Oligomer product distribution with TON for ethylene oligomerization including: butene (■), hexene (●), octene (▲), decene (▼) and dodecene (◆), together with ethylene conversion (○). (b) Fitting of the ethene oligomer average distributionwith Schulz-Flory distribution. Reaction condition: 353 K reaction temperature, 31 bar total pressure, 14.1 h^{-1} WHSV.

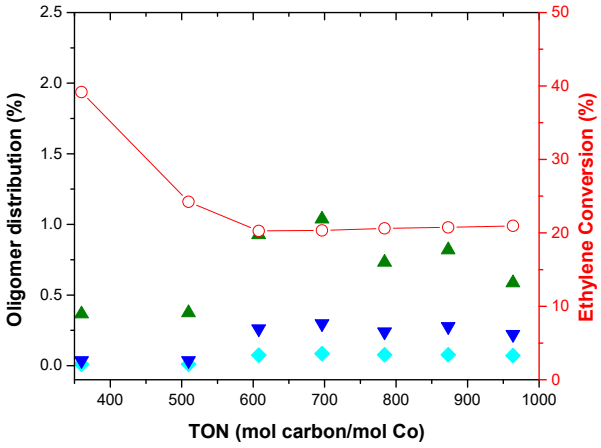

Figure 4.6 A zoomed-in version of Figure 4.5 for a better display of octene (▲), decene (▼) and dodecene (◆) distribution together with ethylene conversion (○) with TON during ethylene oligomerization at ethylene conversion around 20-40%.

The percentage of linear oligomers in the dimerization products, or linear dimer distribution, for the four olefin feeds is shown in Figure 4.7. The linear dimer distribution is defined as the percentage of the linear dimer formed divided by all the dimer products observed (Equation 4.4). The linear dimer distribution from the four feeds did not change with TOS. The dimer products from ethylene oligomerization are 100% linear including 1-butene and *trans*- and *cis*-2-butene. Eighty three percent of C8 olefins from butene oligomerization were linear with the remainder being mono-methyl branched C8 olefins. This result is consistent with our previous study on 1-butene conversion at high WHSV [119]. Similarly, 1-hexene was dimerized to linear C12 olefins with an average linear dimer distribution of 74.34%. The conversion of propylene showed the lowest linear dimer distribution with an average of 46.97%, which is consistent with the work of Shultz *et al*. on propylene oligomerization over CoO_X/N-C catalyst [75].

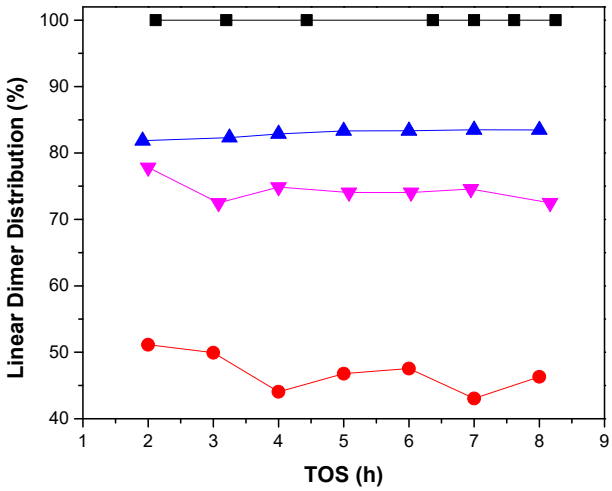

Figure 4.7 The percentage of linear dimers in the dimer products for oligomerization of ethylene (■), propene (●), 1-butene (▲) and 1-hexene (▼). Reaction condition: 353 K, 450 psi, 14.1 h^{-1} WHSV.

Figure 4.8 exhibits the linear oligomer distribution and linear alpha olefin distribution (defined by the percentage of the linear alpha olefin observed over the total amount of oligomers formed with the same carbon number) based on carbon number for ethylene oligomerization. An increasing number of branched oligomers were observed with increasing carbon number, together with a decreasing number of alpha olefin products.

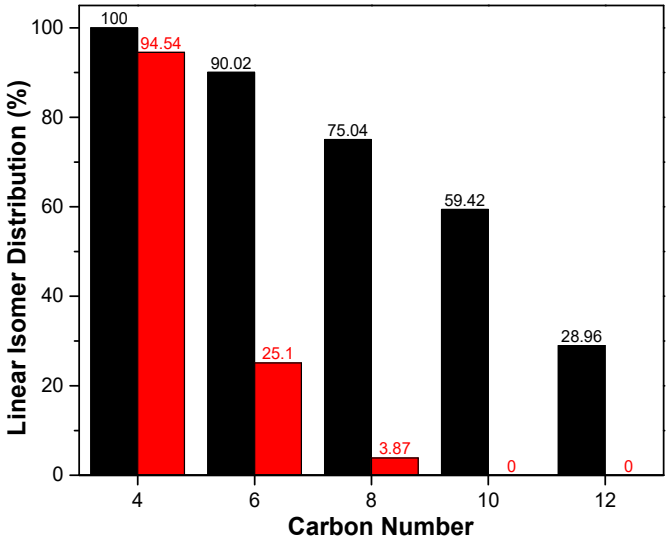

Figure 4.8 Percentage of total linear oligomers (black bar) and linear alpha olefins (red bar) based on the carbon number of the oligomer for ethylene oligomerization. Reaction condition: 353 K reaction temperature, 31 bar total pressure, 14.1 h^{-1} WHSV, 14.4 h TOS.

4.3.3 Conversion of Internal Hexene

The ability of CoO_X/N-C to convert internal olefins was investigated by reacting a feed containing different concentrations of 1-, 2- and 3-hexene (with a 1 wt% 1-heptane tracer) at low WHSV (0.71 h^{-1} or 0.18 h^{-1}) shown in Table 4.7. The mixture of 2- and 3-hexene was prepared by isomerization of 1-hexene as described in Section 4.2.3 and Table 4.8. The 1-hexene conversion was 95% for the pure 1-hexene feed with a 9.35% oligomer selectivity in the first 30 h (Table 4.7). As shown in Figure 4.9, both the 1-hexene conversion and oligomer selectivity decreased with 1-hexene concentration when 2- and 3-hexene were present in the feed. A comparison of the reaction rate of 1-hexene with various concentrations at increasing TONs is depicted in Figure 4.10. The reaction rate did not show a significant decline until an above 1000 TON was reached when internal hexene was absent. The 5% 1-hexene/internal hexene showed the most rapid deactivation with up to 88 mol_{carbon}/mol_{Co} total TON. The catalyst deactivated more rapidly with an increasing concentration of internal hexene in the feed. Nevertheless, the oligomer selectivity was lower for the 12% 1-hexene feed diluted in the pentane solvent (1.25%) than in the 2- and 3-hexene

mixture (4.26%). These experiments indicate that the internal olefin increases the rate of catalyst deactivation possibly by forming olefin deposits in the catalyst pores (Figure 4.11).

Table 4.7 Oligomerization and isomerization activity of internal hexene feeds with various 1-hexene concentrations.

Feed 1-hexene concentration (TOS)		99% (0-30 hr)[e]	99% (45-55 hr)[e]	54% (0-30 hr)[e]	54% (45-55 hr)[e]	12% (0-30 hr)[e]	12% (45-55 hr)[e]	12% (0-30 hr)[d,e]	12% (45-55 hr)[e]	5% (0-30 hr)[f]	5% (45-55 hr)[f]
Inlet Feed concentration (mol/L)	1-hexene	8.04	8.04	4.40	4.40	1.01	1.01	0.90	0.90	0.40	0.40
	2- & 3-hexene	0.04	0.04	3.67	3.67	7.07	7.07	<0.01	<0.01	7.68	7.68
	n-pentane	0	0	0	0	0	0	7.58	7.58	0	0
	n-heptane	0	0	0	0	0	0	0.04	0.04	0	0
Outlet concentration (mol/L)	1-hexene	0.35	1.72	1.08	3.05	0.32	0.78	0.06	0.10	0.25	0.40
	2- & 3-hexene	7.00	5.47	7.70	4.85	7.51	7.26	0.69	0.65	7.81	7.68
	n-pentane	0	0	0	0	0	0	7.78	7.77	0	0
	n-heptane	0	0	0	0	0	0	0.04	0.04	0	0
$(t/i)_{reaction}/(t/i)_{equilibrium}$[a]		3.09	23.76	10.08	39.90	2.65	6.64	5.06	5.06	1.96	3.24
1-hexene conversion (%)		95.53	78.80	75.45	30.60	68.10	22.75	93.74	89.45	37.49	0
Oligomer selectivity (%)		9.35	13.72	4.90	7.29	4.26	1.71	1.25	2.23	0.72	0
Isomer selectivity (%)		90.65	86.28	95.10	92.71	95.74	98.29	98.74	97.77	99.28	0
C12 oligomer yield (%)		8.93	10.81	3.70	2.23	2.90	0.39	1.15	1.95	0.27	0
Linear C12 distribution[b]		73.58	77.80	69.46	77.58	72.76	BDL[c]	69.98	71.77	BDL[c]	BDL[c]

[a] The value is calculated from the equation: $(\text{terminal hexene/internal hexene})_{reaction}/(\text{terminal hexene/internal hexene})_{equilibrium}$.
[b] Linear C12 products distribution in the overall observed C12 oligomer products.
[c] The quantity of the product is below detection limit.
[d] 1-hexene was diluted with pentane solution with 1 wt.% heptane as internal standard.
[e] Reaction condition: 353 K, 31 bar, 0.71 h^{-1} WHSV.
[f] Reaction condition: 353 K, 31 bar, 0.18 h^{-1} WHSV.

Table 4.8 1-Hexene conversion over NH_4-FER catalyst in batch reactor.

Distribuion (%)	Feed	Equilibrium composition [a]	Equilibrium composition [b]	Carbon molar Distribution after reaction [c]
1-hexene	99.52	1.55	4.01	4.81
2-&3-hexene	0.48	98.45	95.99	92.17
Oligomers	0	0	0	3.02

[a] The equilibrium composition is calculated from AspenPlus with Peng-Robinson equation of state. Condition: 353 K, 450 psig.
[b] Condition: 473 K, 290 psig.
[c] Isomerization condition with NH_4-FER at 473 K, 290 psig.

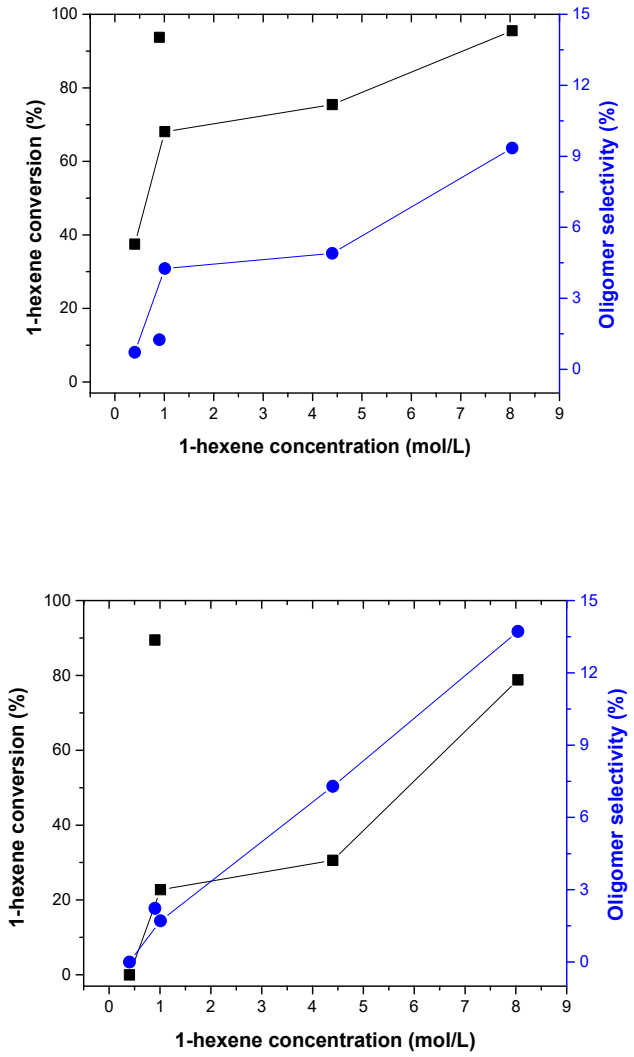

Figure 4.9 Conversion of 1-hexene diluted with 2 and 3-hexene or pentane. 1-hexene conversion (■) and oligomer selectivity (●) for hexene oligomerization at 0-30 h TOS (top) and 45-55 h TOS (bottom). The connected dots represent 1-hexene/internal hexene.

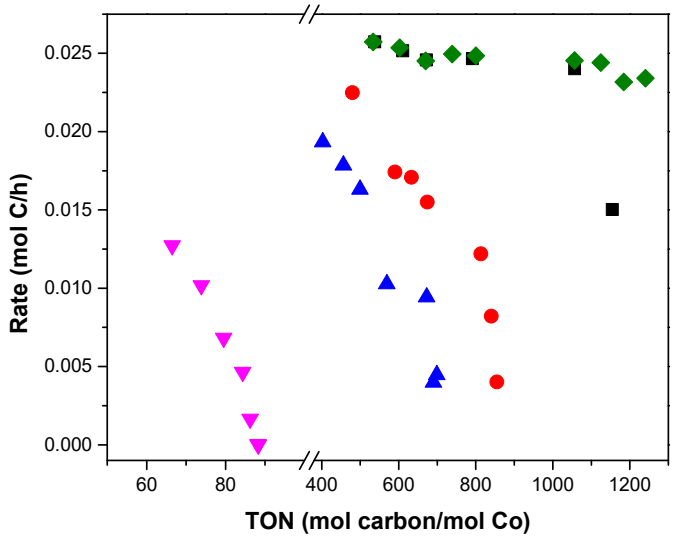

Figure 4.10 1-Hexene consumption rate of 1-hexene and internal hexene mixtures with 1-hexene composition of 99% (■), 54% (●), 12% (▲), 5% (▼) and 12% 1-hexene diluted in pentane (◆) as a function of TON.

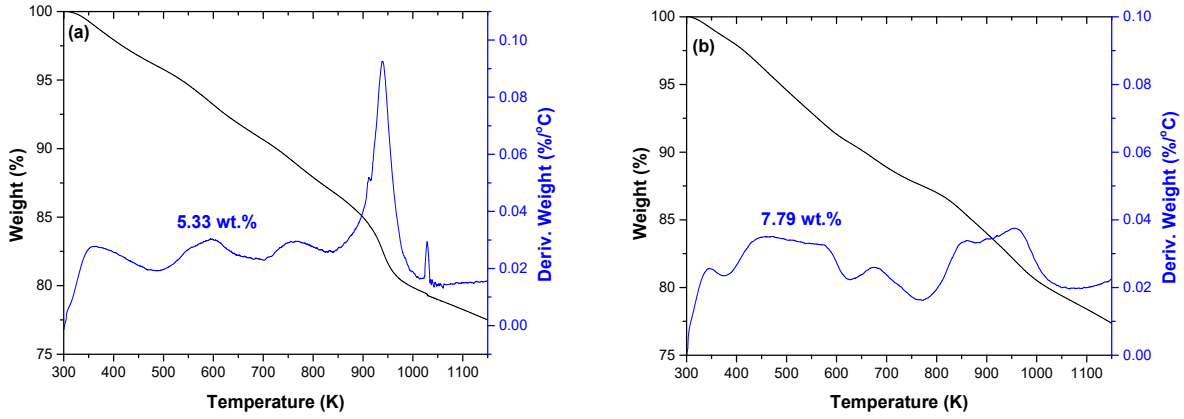

Figure 4.11 TGA profiles for the spent catalyst after reaction with (a) 5% 1-hexene diluted in pentane solution and (b) 5% 1-hexene diluted in 2- and 3-hexene mixture. Black line represents the weight loss; blue line represents the derivative weight loss regarding to temperature. The catalyst (b) showed more weight loss compared to (a) in the temperature range of 400-500 K, which indicates more olefin deposits occurred over the catalyst after the reaction with 2- and 3-hexene present in the feed.

4.3.4 Reaction Mechanism

A comprehensive reaction mechanism describing the catalytic performance of CoO_X/N-C in olefin conversion should explain the following experimental results: (1) an extensive isomerization of terminal olefins into internal

olefins (i.e., 1-butene and 1-hexene feed); (2) a near-equimolar mixture of linear hexene and mono-methyl branched dimer from propylene oligomerization; (3) the most abundant dimer product from 1-butene conversion is 3-octene, followed by 2-octene and 4-octene; (4) ethylene oligomerization produced a Schulz-Flory distribution of oligomers; (5) in our previous work on 1-butene conversion, a Schulz-Flory distribution of oligomers was also observed when the oligomer yield reached 29.0% (Fig S5); (6) the branched C8 oligomers from ethylene oligomerization are the same as the C8 oligomers observed from 1-butene conversion; (7) above 70% of linear C12 oligomers from 1-hexene conversion; and (8) species such as vinylidene and mono-methyl-alpha-heptene were not observed.

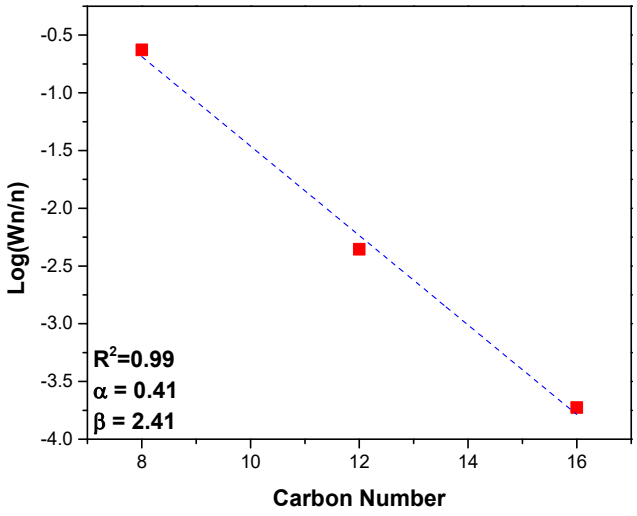

Figure 4.12 Fitting of the product selectivity with Schulz-Flory distribution from 1-butene oligomerization at an oligomer yield of 29.0%.

We have previously used a metallacycle mechanism to describe the products formed from 1-butene conversion on this catalyst [119]. However, this mechanism is found to be inconsistent with our current results. A Schulz-Flory distribution of oligomers was observed with both ethylene and 1-butene when we had oligomer yields of above 20%. This type of distribution indicates that the rate constants for chain propagation and for product release are independent of chain length [111]. When a metallacycle mechanism is operative, the rate of product elimination is highly dependent on the size of the metallacycle, and the oligomer distribution does not follow a Schulz-Flory distribution [111]. For example, in ethylene oligomerization with chromium-based catalysts, 1-hexene is selectively formed due to a highly stable metallacycloheptane species as evidenced by both isotopic labelling experiments [89, 113] and computational [111] methods. A Cossee type mechanism can describe chain growth from a Shultz-Flory

distribution of oligomers. Similarly, Metzger *et al.* have adopted the Cossee-Arlman mechanism to describe the high selectivity of 1-butene from ethylene with a Ni-MFU-4*l* catalyst [23, 125]. Nevertheless, without further evidence regarding the manner of chain propagation, a metallacycle mechanism cannot be completely ruled out with CoO_X/N-C catalyst.

A Cossee type mechanism that accounts for the products observed from ethylene conversion over CoO_X/N-C catalyst is described in Figure 4.13. Linear olefins would be the only products formed if ethylene was the only reactive monomer being incorporated into the growing oligomer. However, linear internal olefin products and mono-methyl branched oligomers were also observed. Our results with 1-butene and 1-hexene demonstrated high overall conversions at the current reaction conditions. It is thus reasonable to assume that the heavier products (1-butene, 1-hexene, 1-octene, etc.) formed directly from ethylene oligomerization could be re-adsorbed and isomerized or incorporated into a growing cobalt-alkyl. For example, 2-butene and 2- and 3-hexene can be formed by the re-adsorption and isomerization of 1-butene and 1-hexene. It should be noted that, the branched C8 oligomer species observed during ethylene tetramerization are the same as the branched C8 oligomer species for 1-butene dimerization though the C8 branched oligomer selectivities are slightly different. It is likely that the formation of the branched C8 oligomers was the result of the reaction between the cobalt-*n*-butyl with 2-butene (forms 3-methyl-2-heptene), and the reaction between a cobalt-*iso*-butyl species formed by 2,1 insertion of 1-butene or insertion of 2-butene with 1-butene via 2,1 insertion (forms 5-methyl-2- and 5-methyl-3-heptene). The insertion of ethylene into a cobalt-*iso*-hexyl species seems unlikely, because no mono-methyl-1-heptene species were observed.

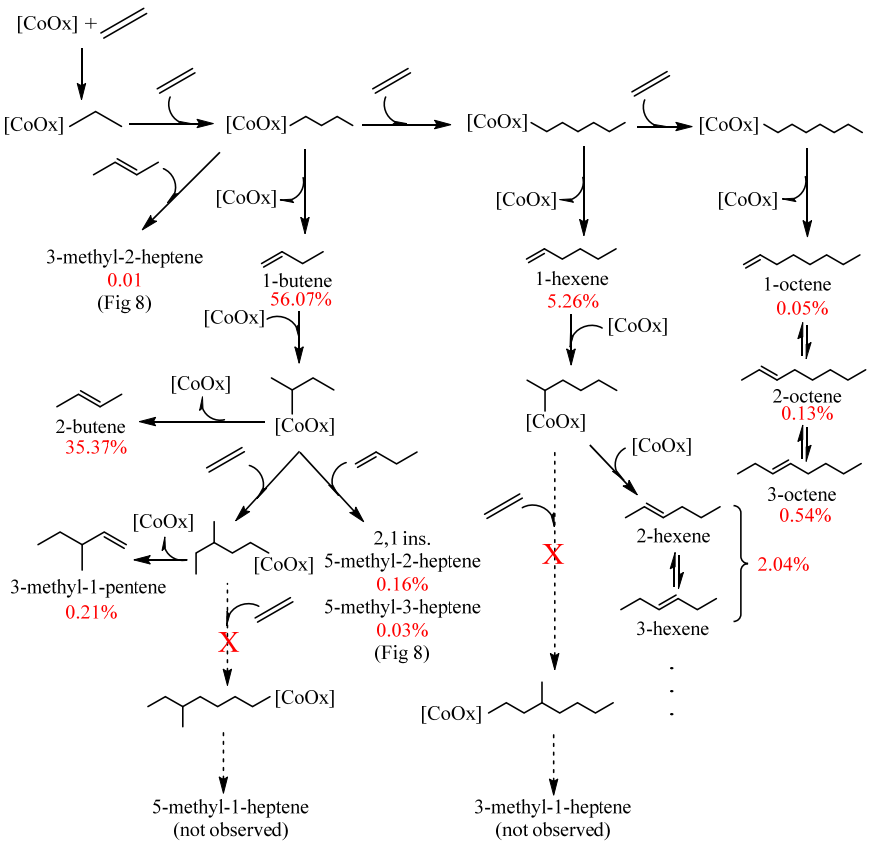

Figure 4.13 Reaction mechanism for the conversion of ethylene over CoO_X/N-C catalyst with products of up to C8. The numbers in red indicate the product selectivity.

Figure 4.14 shows the reaction mechanism for the conversion of linear alpha olefin with greater than 2 carbons over CoO_X/N-C. There are two insertion modes for these olefins: 1,2 insertion and 2,1 insertion. 1,2 insertion involves attachment of 1-butene at the terminal position (α-carbon) onto the cobalt active phase. The 2,1 insertion involves attachment at the secondary position (β-carbon). The 2,1 adsorbed cobalt-*iso*-alkyl species then undergoes a rapid β-H elimination step to give a 2-alkene product, except for during propylene conversion. The remaining cobalt-*iso*-alkyl species could couple with another olefin by a 2,1 insertion mode to give mono-methyl branched olefins. Based on the high selectivity (~80%) of internal isomers of butene and hexene, the β-H elimination step of the cobalt-*iso*-alkyl species is more rapid than the chain propagation step. Less than 5% of the oligomer products were mono-methyl branched oligomers for 1-butene and 1-hexene feeds. The 2,1 adsorbed propylene species undergoes a chain propagation step, without the competition of isomerization, to form 4-methyl-1-pentene and 4-methyl-2-pentene at a relatively high selectivity (47.0%). This explains the high linear dimer distribution observed for 1-butene (82.9%) and 1-hexene (72.5%), but not for propylene (53.0%).

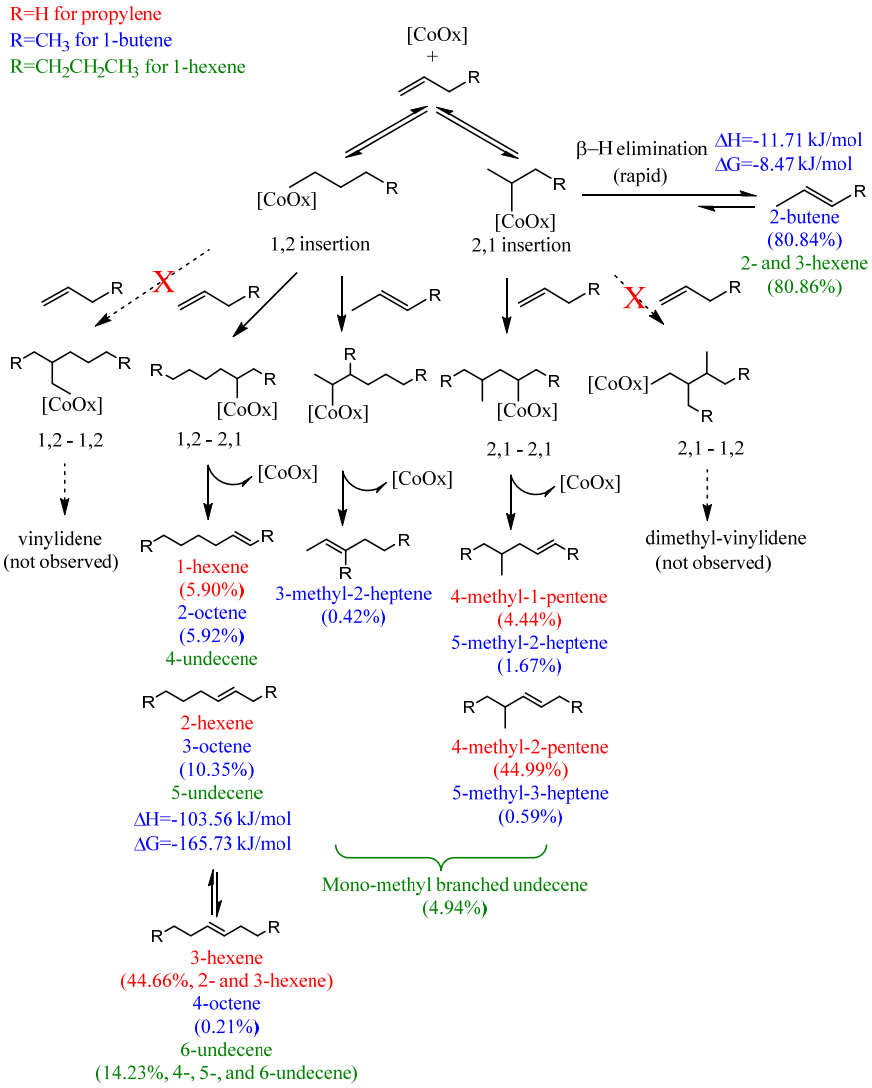

Figure 4.14 Reaction mechanism for the conversion of linear alpha olefins with above two carbon number over CoO_X/N-C catalyst. Color code: red: product selectivity from propylene oligomerization; blue: product selectivity from 1-butene conversion; green: product selectivity from 1-hexene conversion. The dotted arrow represents reaction steps unlikely to occur.

4.4 Conclusions

CoO_X/N-C is active in the oligomerizaiton of ethylene, propylene, 1-butene and 1-hexene. The catalyst is also active for isomerization of 1-butene and 1-hexene. The main product from ethylene oligomerizaiton is 1-butene, and the products follow a Schulz Flory distribution with a low chain growth probability of 0.37. Propylene has the lowest linear dimer selectivity because adsorbed propylene dose not undergo isomerization reaction. A Cossee-type

mechanism can explain the product distribution for the conversion of light LAOs over CoO_X/N-C catalyst. The catalyst is featured by a non-regioselective initial insertion step (1,2 and 2,1 insertion) followed by a regioselective 2,1 insertion. The β – H elimination of the sepcies formed after an intial 1,2 insertion is rapid, resulting in a high isoemr selectivity during 1-butene and 1-hexene conversion. The initial 2,1 insertion also lead to the formation of branched oligomers after a chian propagation step. The linear internal olefin products are selectively formed following a 2,1 – 2,1 inseriton sequence. The β – H elimination step is normally non-selective. The catalyst showed no activity in converting internal hexene into oligomers.

CHAPTER 5 Cr-promoted CoO_X/N-C catalyst: ethylene and 1-butene dimerization

The content in this chapter is adapted from a manuscript currently under review:

Zhuoran Xu, Joseph P. Chada, Lang Xu, Dongting Zhao, Devon C. Rosenfeld, Jessica L. Rogers, Ive Hermans, Manos Mavrikakis, George W. Huber. Ethylene Dimerization and Oligomerization to 1-Butene and Higher Olefins with Chromium-Promoted Cobalt on Carbon Catalyst. *Submitted.*

5.1 Introduction

1-butene, a light linear alpha olefin (LAO), is used in the production of polyethylene, polybutene, butylene oxide, and aluminum alkyls. The production of 1-butene commonly follows two main routes: the separation of crude C4 refinery streams and the dimerization of ethylene [3]. The price of ethane in the US fell by 60 percent from 2011 to 2012 roughly to its fuel equivalent [126, 127] and has remained at a low level ever since. The decline in the cost of ethane and ethylene has caused the increase in interest for dimerization of ethylene to 1-butene and longer olefins. Selective dimerization of ethylene to 1-butene is performed commercially with homogeneous catalyst systems in three different processes. IFP-SABIC has developed the AlphaButol® process with a total 1-butene production capacity of 708,000 metric tons per year (MTPY) [15, 128]. This process operates in the liquid phase using a homogeneous catalyst system comprising $Ti(OBu)_4$ and $AlEt_3$ which avoids isomerization of 1-butene to 2-butene, hence no superfractionation (a distillation process that generally requires a large number of theoretical plates and high flux ratios for the separation of liquid mixtures that have close boiling points such as olefin isomers) of the product stream is needed. High yields (nearly 90%) of 1-butene from ethylene are obtained in the Philips process, which employs a homogeneous catalyst system consists of bis(tri-n-butylphosphine) nickel dichloride and $AlEtCl_2$ in an olefin dimerization reactor purged with cleaning solvent followed by the reaction solvent prior to the addition of the catalyst and ethylene feed [129, 130]. In the 1980s DOW developed a process to dimerize ethylene into 1-butene using an organic aluminum compound (AlR_3) as the catalyst in a boiling solvent [124, 131]. The above chemical processes demanding high selectivity utilize homogeneous molecular catalysis, where organic solvent such as alkanes and aromatics are required to stabilize the catalyst in ~ 6.9 mmol/l concentration [132] making the recycle or removal of those catalysts difficult. Additionally, the homogeneous catalysts generally require an organoaluminum compound (e.g., MAO) as co-catalyst to form the active species, and the Al/M (M represents the active metal center) ratio is in the range of 1 – 1000. The organoaluminum co-catalysts are highly air and moisture sensitive necessitating careful handling and storage and use of dry organic solvents. Consequently, the development of an effective heterogeneous catalyst system is desirable for the large-scale manufacture of chemical commodities to reduce operating cost.

Studies on ethylene dimerization with acidic heterogeneous catalysts have shown less than a 20% 1-butene selectivity at industrially relevant conversions due to double bond isomerization producing 2-butenes. For example,

ethylene dimerization catalyzed by Rh-Y at a conversion of 5-10% produces 2% 1-butene, 77% *trans*-2-butene and 21% *cis*-2-butene [133]. Rapid isomerization of 1-butene into 2-butene was also observed for nickel-containing MCM-41 and AlMCM-41 molecular sieves for ethylene dimerization [134]. Several other Ni – containing heterogeneous catalysts including NiO-ZrO_2/WO_3 [135], Ni/Al-KIT-6 [136], Ni/SiO_2-Al_2O_3 [137], Ni-Y [55] and Ni-MCM-36 [57] all produced mainly 2-butene from ethylene. A nickel catalyst bearing two PEt_3 ligands supported on SiO_2, however, showed a 95% 1-butene selectivity at 23% ethylene conversion as reported by Cai *et al* [22]. Recently, Metzger *et al.* synthesized a Ni-exchanged MOF molecular catalyst (Ni-MFU-4*l*) which combines a high activity (turnover frequency (TOF)=21,000 h^{-1}) with a high 1-butene selectivity (92.0 wt.%) [23]. Nevertheless, Ni-MFU-4*l* requires a co-catalyst (MAO) with 50-500 equivalents to the metal center to show dimerization activity.

Schultz *et al.* have used cobalt oxide supported on ammonia-treated carbon for the dimerization of light olefins [21, 75, 118]. Ort *et al*. [138] improved the activity of this catalyst by approximately two fold by adding ZnO into the cobalt oxide on carbon catalyst. Addy *et al*.[139] have reported that the incorporation of nickel, chromium, and copper into the cobalt oxide supported on carbon catalyst was able to show improved activity for olefin oligomerization. Hill [140] have demonstrated a nearly two fold improvement in activity after treating the cobalt oxide on carbon catalyst with CrO_3. We have identified a cobalt oxide species to be the main phase of the active cobalt oxide on carbon catalyst [119], and have established a positive correlation between the pyridinic nitrogen content in the carbon support and the catalyst's oligomerization activity [141]. The selectivity of the catalyst can be explained by invoking a Cossee-Arlman mechanism [142]. During ethylene oligomerization, a 1-butene selectivity of 87.0% was observed at a conversion of 10.0% with the carbon supported cobalt catalyst [142]. The promotional effect of adding a second metal into the primary metal or metal oxide is commonly seen in many chemical reactions such as biomass upgrading [143-145], oxygen reduction reaction (ORR) [146], and Fischer-Tropsch synthesis [147, 148]. In Chapter 5, we will report the enhanced activity and promotional effect of the incorporation of chromium into the CoO_X/N-C catalyst and the high 1-butene selectivity achieved during ethylene oligomerization with this catalyst. Chromium itself is also a widely used active metal in the oligomerization and polymerization of ethylene both in the form of soluble metal complexes [149] (after activation with a co-catalyst) and as a SiO_2-supported metal oxide [89, 150]. The chromium-promoted cobalt oxide on carbon catalyst *via* facile synthesis could provide an alternative for selective dimerization of ethylene into 1-butene without the use of a co-catalyst.

5.2 Experimental

5.2.1 Catalyst Preparation

The 13 wt.% cobalt on carbon catalyst was synthesized based on a wetness impregnation method previously described in the literature [75, 119]. The catalyst is denoted as CoO_X/N-C. The chromium-promoted cobalt on carbon catalyst was synthesized as follows: 2.00 g sieved activated carbon (Norit, Darco MRXm-1721; BET surface area 600-800 m^2/g; 250-600 μm particle size) was first treated with 1.8 mL 30% NH_4OH solution at room temperature. The carbon was then dried at 403 K for 2 h. A solution of 1.15 g $Co(NO_3)_2 \cdot 9H_2O$ (Sigma-Aldrich) and 0.78 g $Cr(NO_3)_3 \cdot 9H_2O$ (Sigma-Aldrich) dissolved in 1.82 g deionized water was prepared and added dropwise onto the treated carbon. After drying at 403 K overnight, the impregnated carbon was treated with another 3.0 mL of 30% NH_4OH solution. The theoretical metal loadings are 8 wt.% Co and 5 wt.% Cr based on the corresponding metal oxides on carbon. The catalyst is denoted as Cr-CoO_X/N-C. The chromium on carbon catalyst was synthesized following the same steps as above. During the synthesis, 0.78 g $Cr(NO_3)_3 \cdot 9H_2O$ (Sigma-Aldrich) was dissolved in 1.82 g deionized water and deposited on the carbon support previously treated with NH_4OH followed by the same drying steps as mentioned above. The catalyst is denoted as CrO_X/N-C.

5.2.2 Catalyst Characterization

The X-ray diffraction (XRD) profiles were collected between $2\theta = 5^o$ and $2\theta = 45^o$ with Rigaku Rapid II diffractometer with a Mo K_α source at 50 kV and 50 mA. The crystallite phase identification was performed with JADE 9 software. Samples for XRD analysis were pretreated in flowing helium at 150 mL/min with 5.5 K/min ramp rate and held at 503 K for 2 h then cooled to RT prior to the XRD measurement.

X-ray absorption spectroscopy (XAS) measurements were taken at beamline 12-BM of the Advanced Photon Source (APS) at Argonne National Lab (Lemont, IL). Catalyst samples were crushed and diluted with boron nitride (Sigma-Aldrich). Self-supporting pellets were pressed inside a 4 mm I.D. stainless steel cylindrical sample holder. Dilution ratios were calculated to give an edge step of ~1. The stainless steel sample holder was sealed in a 1” O.D. Kapton-windowed quartz tube fitted with Swagelok valves. The sealed sample was pretreated in a tube furnace and continually purged with He. After pretreatment, the sealed samples were transferred to the beamline without exposure to air. XAS measurements of the Cr (5.989 keV) and Co K-edge (7.709 keV) were collected in the

transmission geometry. X-ray absorption was measured with gas ionization chambers before and after the sample holder. Energy calibration was performed with metallic reference foils placed between ion chambers after the sample. Data normalization and background subtraction were performed in Athena [151].

X-ray photoelectron spectroscopy (XPS) was conducted on K-alpha XPS spectrometer (Thermo Scientific) with a micro-focused monochromated Al K_α X-ray source. Prior to the measurements, the samples were pretreated in 150 mL/min flow of helium at 503 K for 2 h and sealed in a stainless steel tube. The samples were then packed into a vessel (Transfer Vessel K-Alpha) and sealed under vacuum in a glove box under a nitrogen atmosphere. The XPS measurements were taken of the samples without exposure to air. Samples were analyzed at 10^{-7} mbar and room temperature with the flood gun on to avoid sample charging. Spectra were taken in the regions of C 1s, O 1s, N 1s, Co 2p, Cr 2p. The binding energy (BE) values were referred to the BE of the graphite C 1s peak at 284.8 eV. The Co 2p and Cr 2p spectra were taken over 30 scans with a pass energy of 50 eV and a dwell time of 50 ms. The energy step size was 0.2 eV for all scans in all regions. No difference was observed in the XPS spectra for two different spots for each sample. The peak fitting was performed using Avantage (Thermo Scientific) software package.

Scanning transmission electron microscopy (STEM) images were collected with an FEI Titan microscope equipped with a Cs aberration corrector operated at 200 kV. High-angle annular dark field (HAADF) images were obtained in the range of 54 to 270 mrad using a 0.8 nm probe and 24.5 mrad probe convergence semi-angle. Catalyst samples were suspended in ethanol with sonication then deposited on a carbon-coated copper grid (EMS). Samples were plasma cleaned for 15 min prior to analysis.

5.2.3 Catalytic Measurement

The ethylene oligomerization reactions were conducted in a tubular down-flow fixed-bed reactor described elsewhere [18, 119]. The reaction pressure was adjusted with a back pressure regulator. For a typical reaction, 0.5 g to 2.0 g of the catalyst sample was packed into a 3/8 in. stainless steel tube without diluent. The reactions were carried out at 353 K and 13.4 bar ethylene partial pressure (unless otherwise specified) in the gas phase. The overall reaction pressure was kept at 31 bar, and ethylene (UHP, Airgas) was co-fed with helium (UHP, Airgas) at 34.8

mL/min and 45.4 mL/min flow rate, respectively. The gas effluent was analyzed by an online gas chromatograph (GC-FID, Shimadzu) every 0.5 h. The liquid products were gathered from a cold trap and analyzed by a comprehensive two-dimensional gas chromatograph-mass spectrometer (2D GC-MS). The GC operation conditions and the compound standard information can be found elsewhere [18, 119]. Ethylene conversion, product selectivity, product yield, α-butene distribution and weight hourly space velocity (WHSV) were calculated based on Eq. 5.1-5.5.

Equation 5.1 Ethylene conversion (%) = $\frac{\textit{moles of carbon in the overall detected products}}{\textit{overall moles of carbon detected at the outlet}} \times \mathbf{100}\%$

Equation 5.2 Product selectivity (%) = $\frac{\textit{moles of carbon in a specific group of product}}{\textit{moles of carbon in the overall detected products}} \times \mathbf{100}\%$

Equation 5.3 Product yield (%) = $\boldsymbol{\textit{Ethylene conversion} \times \textit{Product selectivity}}$

Equation 5.4 $\boldsymbol{\alpha}$-Butene distribution (%) = $\frac{\textit{moles of } \alpha\textit{-butene in the product}}{\textit{moles of all butenes in the product}} \times \mathbf{100}\%$

Equation 5.5 Weight hourly space velocity (WHSV, h^{-1}) = $\frac{\textit{hourly mass feed flow rate}}{\textit{catalyst mass}}$

5.3 Results and Discussion

5.3.1 Selectivity

Figure 5.1 shows the butene isomer selectivity with time on stream (TOS) for ethylene oligomerization at a WHSV of h^{-1}. At the initial TOS (< 2.0 h TOS), the reactor was in the transient state with below 60% carbon balance. The average yield and selectivity data reported in the later section was taken after 2.0 h TOS. After 2 h TOS, the catalyst did not show any signs of deactivation with an average ethylene conversion of 19.3% and a 1-butene selectivity of 70.1%. At steady state 84.0% of the butenes were 1-butene.

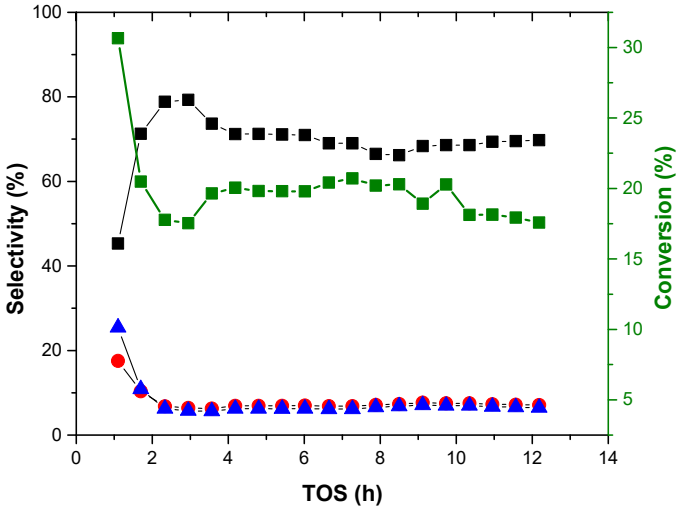

Figure 5.1 Ethylene conversion (■) and product selectivity *vs.* time-on-stream including (■) 1-butene, (●) *trans*-2-butene and (▲) *cis*-2-butene with Cr-CoO_X/N-C. Reaction conditions: 32.63 h^{-1} WHSV, T = 353 K, p (ethylene) = 13.4 bar.

The product selectivity was studied at different ethylene conversions by varying the WHSV from 16.3 h^{-1} to 65.3 h^{-1} as shown in Figure 5.2 and Table 5.1. The main products were 1-butene > *trans*- and *cis*-2-butene > C6 olefins > C8 olefin and C10+ olefins. Olefins up to C20 were detected although they were less than 1% of the products. The 1-butene selectivity decreased from 82.4% to 53.5% with an increasing ethylene conversion from 8.9% to 31.5%. The C6 olefin selectivity increased from 11.8% to 15.0%, and the *trans*- and *cis*-2-butene selectivity increased from 5.6% to 24.1% over this same range. A 44.4 % loss in activity was observed during 12 h TOS at the highest WHSV (65.3 h^{-1}) as shown in Figure 5.3, while no loss in activity was observed at the other WHSVs. Though slightly lower in 1-butene yield at 31.5% ethylene conversion compared to the silica supported nickel complex [22], the Cr-CoO_X/N-C catalyst surpasses the majority of the heterogeneous nickel-based catalysts for ethylene dimerization in overall 1-butene yield.

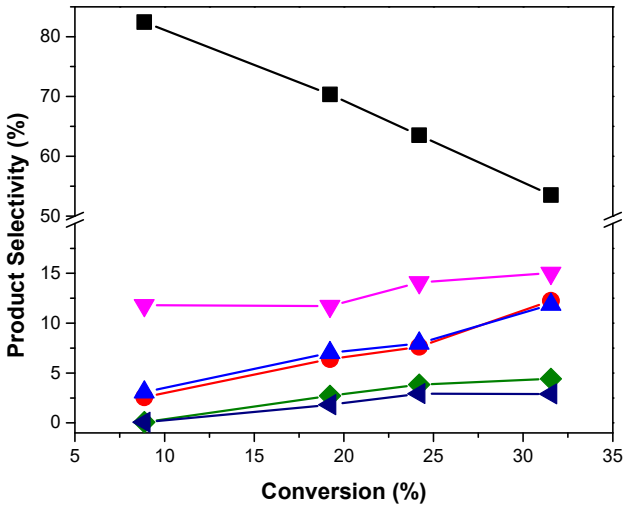

Figure 5.2 Product selectivity including (■) 1-butene, (●) *trans*-2-butene, (▲) *cis*-2-butene, (▼) C6 olefins, (◆) C8 olefins, (◀) C10 and C10+ olefins at different levels of ethylene conversions with Cr-CoO_X/N-C. The selectivity data is averaged after steady state is reached (2.3 h -12.0 h TOS). Lines were added to guide the eye.

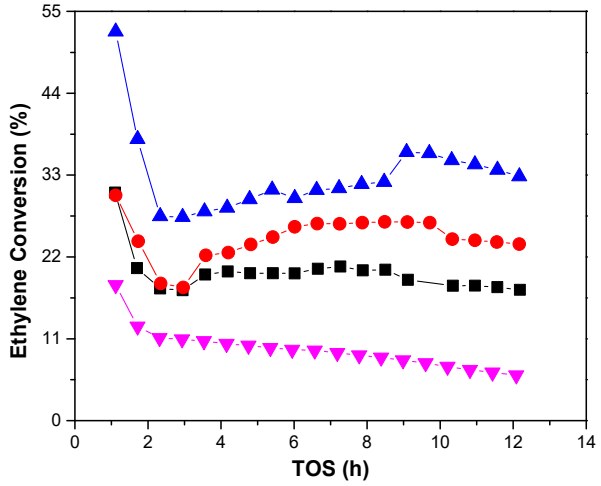

Figure 5.3 Ethylene conversion with time-on-stream at (▲) 16.31 h^{-1}, (●) 21.75 h^{-1}, (■) 32.63 h^{-1} and (▼) 65.25 h^{-1} WHSV. Reaction conditions: 80 ℃, 13.4 bar ethylene partial pressure with helium flow. The WHSV is varied by changing the catalyst loading.

We identified the distribution of C6 and C8 products by two-dimensional GC as shown in Table 5.1. The most abundant C6 olefin species are linear internal hexenes (2- and 3-hexene). The 1-hexene distribution decreased, accompanied by an increase in the linear internal hexene and mono-branched hexene distributions, with increasing

ethylene conversion. The 1-octene distribution also decreased from 9.3% to below 1.0% as ethylene conversion increased from 8.9% to 31.5%. No major change in the total linear octene distribution was observed at different ethylene conversions. The catalyst isomerized the linear terminal olefins into linear internal isomers with increasing conversion.

Table 5.1 Product selectivity and distribution of various products as a function of ethylene conversion over Cr-CoO_X/N-C catalyst. Reaction conditions: 353 K, 13.4 bar ethylene partial pressure balanced in helium, and 12 h TOS.

Ethylene conversion (%)		8.9	19.2	24.2	31.5
WHSV (h^{-1})		65.2	32.6	21.7	16.3
Butene Distribution (%)	1-butene	93.6	84.0	80.3	69.0
	2-butene	6.4	16.0	19.7	31.0
	Total butene selectivity	88.1	83.8	79.1	77.6
Hexene Distribution (%)	1-hexene	31.5	9.8	7.3	3.4
	2- and 3-hexene	66.7	88.0	89.3	93.1
	3-methyl-1-pentene	1.7	2.1	3.3	3.5
	Total hexene selectivity	11.8	11.7	14.1	15.0
Octene Distribution (%)	1-octene	9.3	2.5	1.6	0.6
	trans-2-octene	7.1	7.9	8.0	8.8
	cis-2-octene	4.0	3.7	3.7	3.9
	3-octene	60.5	63.2	58.2	63.4
	4-octene	6.1	10.5	12.1	9.4
	trans-3-methyl-2-heptene	0.9	1.2	1.4	1.6
	trans-5-methyl-2-heptene	0.8	0.1	0.3	0.2
	cis-5-methyl-2-heptene	10.3	8.0	11.5	8.2
	trans-5-methyl-3-heptene	0.2	2.1	2.3	2.6
	cis-5-methyl-3-heptene	0.7	0.6	0.8	1.3
	Total linear octene	87.1	87.8	83.6	86.1
	Total octene selectivity	0.1	4.5	6.8	7.3

5.3.2 Cr Promotion Effect on Catalyst Activity

Figure 5.4 shows ethylene conversion over both Cr-Co O_X/N-C and CoO_X/N-C catalysts. A description of the details of ethylene conversion with CoO_X/N-C catalyst is reported elsewhere [152]. The ethylene conversion with Cr-CoO_X/N-C is 1.6 times as high as CoO_X/N-C at steady state (after 2.3 h TOS) at a 16.3 h^{-1} WHSV. The difference between the Cr-promoted and non-promoted catalyst became less (1.2 times) at higher WHSV (32.63 h^{-1}). The Cr-CoO_X/N-C catalyst increased in conversion slightly after the initial transient period, which was not seen with the CoO_X/N-C catalyst. At both WHSVs, the Cr-CoO_X/N-C is more stable with TOS compared to CoO_X/N-C. Less than 0.1 % ethylene conversion was observed with CrO_X/N-C (at 353 K, 13.4 bar ethylene partial pressure and 65.25 h^{-1} WHSV) as compared to 8.9% conversion at the same conditions with Cr-CoO_X/N-C. This indicates that the activity of monometallic chromium on carbon is negligible.

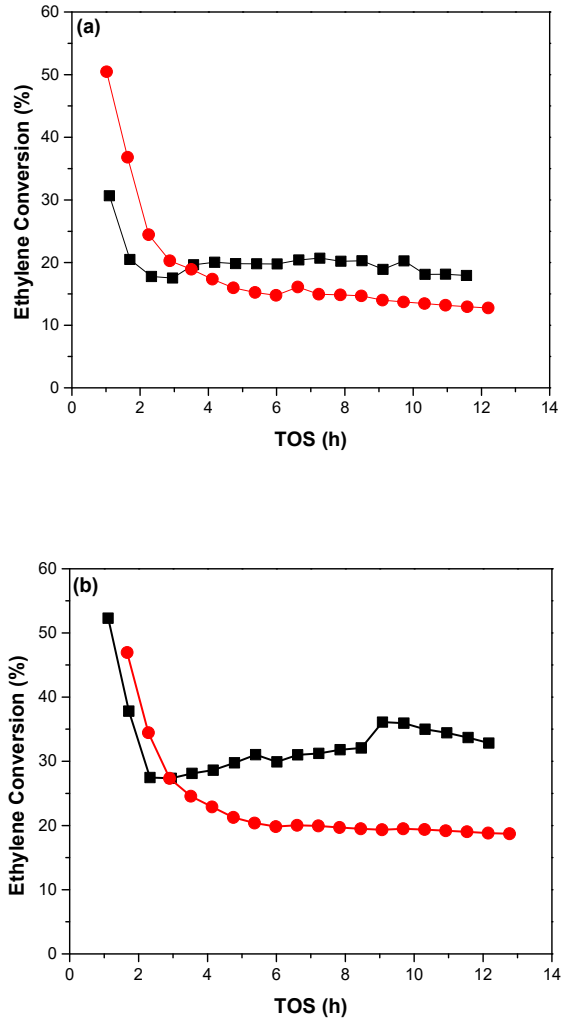

Figure 5.4 Ethylene conversion with time-on-stream for (■) Cr-CoO_X/N-C and (●) CoO_X/N-C catalyst at (a) 46.89 h^{-1} WHSV, and (b) 23.45 h^{-1} WHSV.

5.3.3 Catalyst Characterization

In our previous study of 1-butene conversion with CoO_X/N-C, we have confirmed the existence of Co(III) and Co(II) on this catalyst [119]. At elevated pretreatment temperatures (above 823 K) Co(0) forms in an inert gas atmosphere [119]. A reduction of cobalt was observed for the Cr-CoO_X/N-C compared to CoO_X/N-C catalyst with both x-ray absorption near edge structure (XANES) and XPS. Upon chromium addition, the Co K-edge shifted to lower energy indicative of a partial reduction of Co(III) oxide to Co(II) as shown in Figure 5.5. The CoO_X/N-C catalyst showed a characteristic sharpening of the main $2p_{3/2}$ and $2p_{1/2}$ peaks in the XPS at 780.9 eV and 796.0 eV,

respectively. The main $2p_{3/2}$ and $2p_{1/2}$ peaks were found at 781.1 eV and 796.5 eV respectively for the Cr-CoO_X/N-C catalyst. The minor differences associated with the binding energies of Co^{3+} and Co^{2+} [153] makes it difficult to accurately quantify the amount of Co_3O_4 and CoO within each sample by XPS. However, the satellite peaks (at 787.1 eV and 803.9 eV) for the two catalysts reveals more information regarding the Co_3O_4 and CoO features. A dramatic decrease in intensity of the satellite structure was observed for CoO_X/N-C, whereas a much higher intensity was observed in the satellite peaks for Cr-CoO_X/N-C relative to the main peaks. The high-spin character of the Co^{2+} oxides is unique, and it allows for strong electron correlation which leads to various d-d coupling and charge-transfer from O 2p to the Co 3d. In contrast, the low-spin octahedrally-coordinated Co^{3+} or tetrahedrally-coordinated Co^{2+} does not possess the above effects [154, 155]. Therefore, the relatively sharper Co 2p XPS peaks and the diminished satellite intensity observed from CoO_X/N-C suggest it has more cobalt in the Co_3O_4 structure [156], while the cobalt oxides within Cr-CoO_X/N-C possess more Co^{2+}.

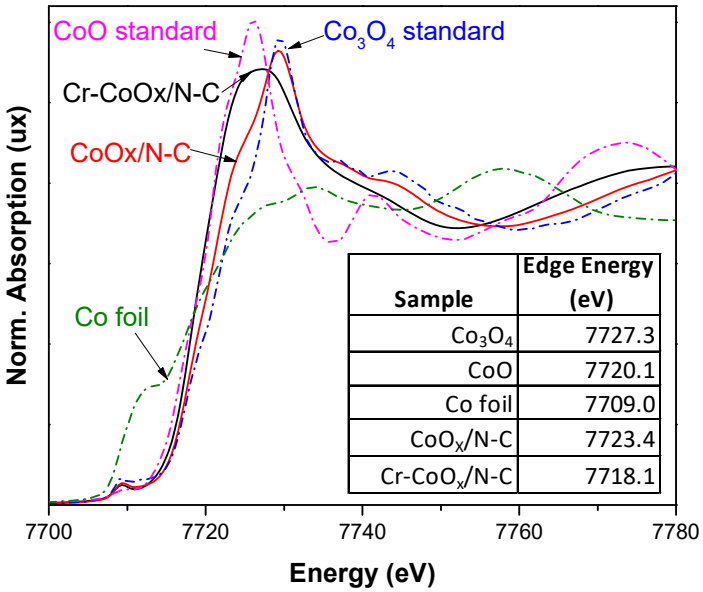

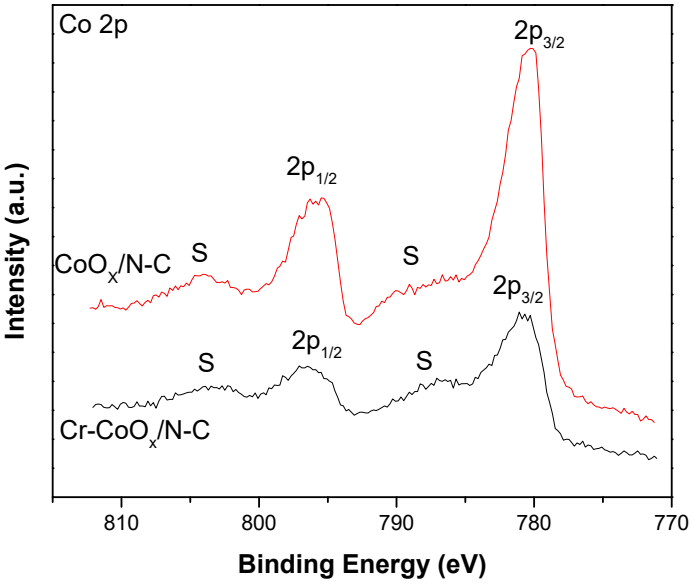

Figure 5.5 Top: XANES spectra collected at the Co K edge. Pink dotted trace: CoO standard; blue dotted trace: Co_3O_4 standard; green dotted line: Co foil; black trace: Cr-CoO_X/N-C catalyst; red trace: CoO_X/N-C catalyst. The cobalt edge energy for each sample is reported in the table. Bottom: Co 2p XPS region comparing CoO_X/N-C catalyst (red) and Cr-CoO_X/N-C catalyst (black). S represents the satellite peak.

As shown in Figure 5.6 upon cobalt addition, there is a shift in the Cr K-ede to higher energy and more notably an increase in the intensity of the pre-edge features consistent with partial oxidation of the Cr (III) to higher oxidation states. The XPS Cr 2p region suggests different chromium species exist for CrO_X/N-C and Cr-CoO_X/N-C on the surface (Figure 5.6). The XPS Cr spectra are similar to what was observed by X. Zhang *et al.* [157] for CrOx/ZnO, and by Y. Zhang *et al.* [158] for Cr/Al_2O_3. For CrO_X/N-C, two peaks representing Cr $2p_{3/2}$ with a binding energy of 577.6 eV and Cr $2p_{1/2}$ with a binding energy of 586.8 eV were observed, and they are the characteristic peaks of Cr^{3+} oxides [153]. The deconvolution of the Cr 2p region for Cr-CoO_X/N-C (Figure 5.7) has resulted in four peaks: Cr^{3+} $2p_{3/2}$, BE=576.6 eV; Cr^{6+} $2p_{3/2}$, BE=579.3 eV; Cr^{3+} $2p_{1/2}$, BE=579.3 eV; and Cr^{6+} $2p_{1/2}$, BE=588.5 eV. The Cr^{3+} and Cr^{6+} compositions for the Cr-CoO_X/N-C surface are 55.9% and 44.1%, respectively, while CrO_X/N-C contains almost entirely Cr^{3+}, consistent with the XANES results.

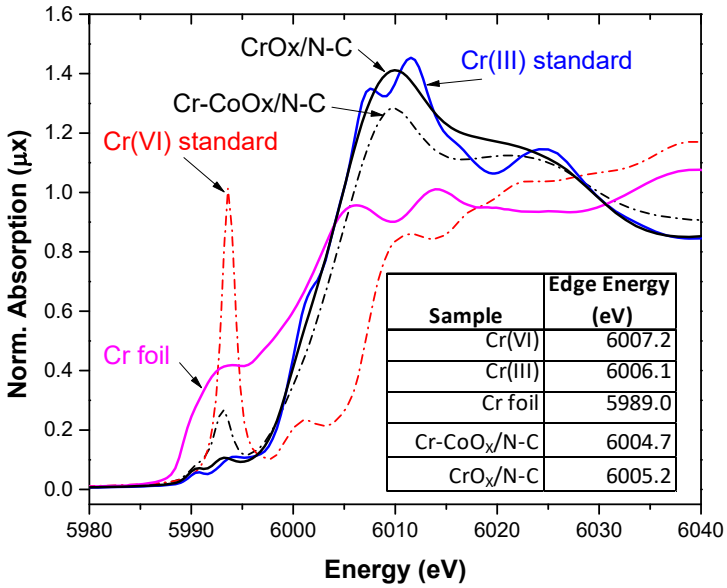

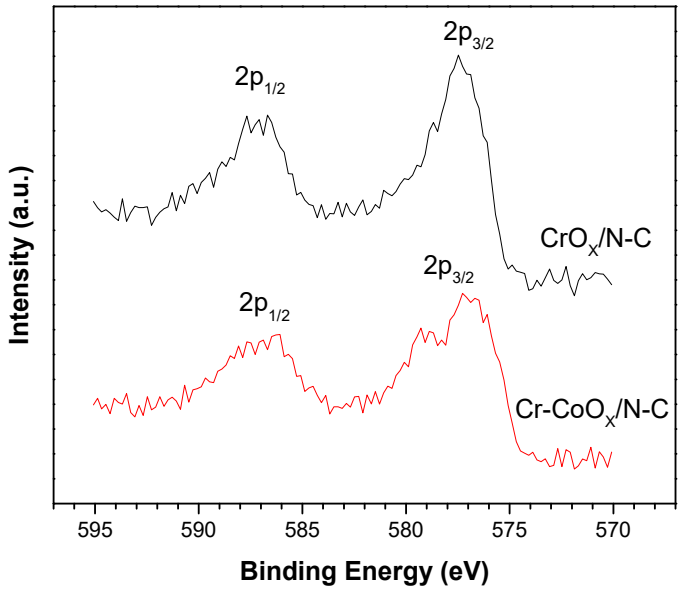

Figure 5.6 Top: XANES spectra collected at the Cr K edge. Red dotted trace: Cr(IV) standard. Blue solid trace: Cr (III) standard. Pink solid trace: Cr foil. Black dotted trace: Cr-CoO_X/N-C catalyst. Black solid trace: CoO_X/N-C catalyst. The chromium edge energy for each sample is reported in the table. Bottom: Cr 2p *in-situ* XPS spectra of CoO_X/N-C (black) and Cr-CoO_X/N-C (red).

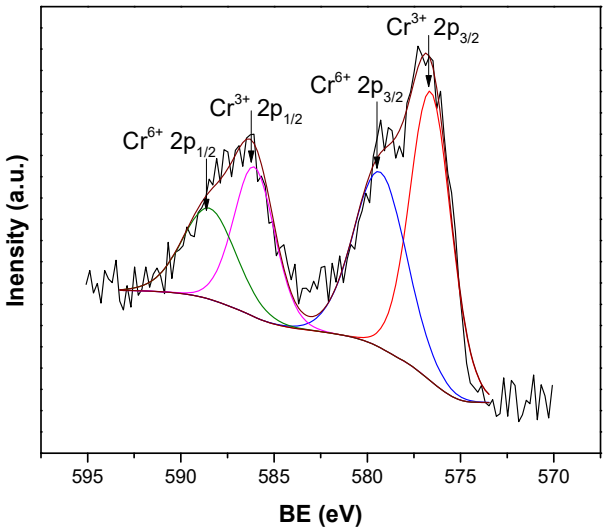

Figure 5.7 Cr 2p region XPS peak deconvolution for Cr-CoO_X/N-C.

The results from XANES and XPS analysis indicate a possible charge transfer from Cr to Co when both metals exist in their corresponding oxide form on the carbon support. As a group VIII metal, Co has a higher electronegativity (χ=1.88) than Cr (χ=1.66), and hence Co would appear in a more reduced form when Cr is present. The electronic effect observed from bimetallic catalysts is very common in transition metal systems [159, 160]. The more reduced Co does not offer any advantage during the initial step where the formation of a metal-olefin complex is favored over a metal center with more electron-accepting features [88, 119]. However, the increased electron density in Co within our Cr-CoO_X/N-C catalyst allows for easier product desorption [22], so that Cr-CoO_X/N-C would suffer less from product olefin deposition. Our prior report hypothesized olefin product deposition as a mode of catalyst deactivation [152]. The weaker binding of the products on the Cr-CoO_X/N-C catalyst could be the reason for the improved catalyst stability.

Figure 5.8 Shows the XRD patterns of the non-promoted and Cr-promoted catalyst. As discussed in the previous chapter, the CoO_X/N-C catalyst contains both Co(III) and Co(II) oxide. The Co_3O_4 (2θ=16.79^o) peak decreases in intensity with Cr addition with no other major peaks appearing. The diminished peak intensity indicates that the addition of Cr has resulted in a cobalt oxide that is primarily amorphous, and possibly with smaller crystallite size and more defects within the Co_3O_4 phase [161]. Additionally, no Cr-containing peak is observed in the XRD

patterns of Cr-CoO_X/N-C and CrO_X/N-C (Figure 5.9), indicating that the Cr exists in either an amorphous form or with very small crystallite size.

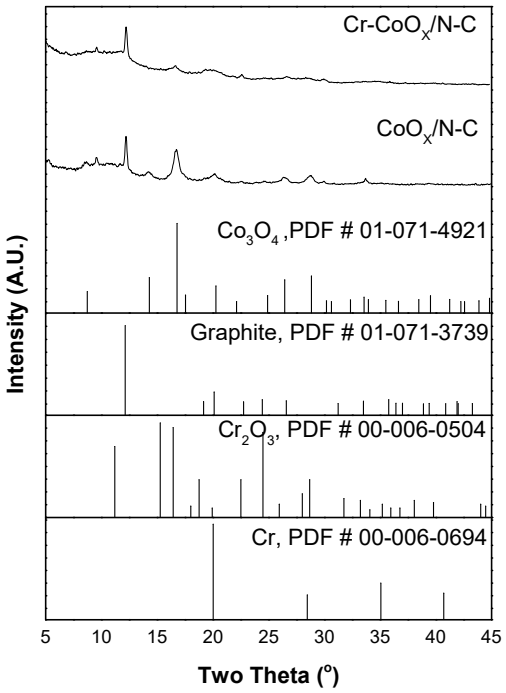

Figure 5.8 Mo-pXRD spectra for Cr-CoO_X/N-C catalyst and CoO_X/N-C catalyst after pretreatment at 503 K in helium.

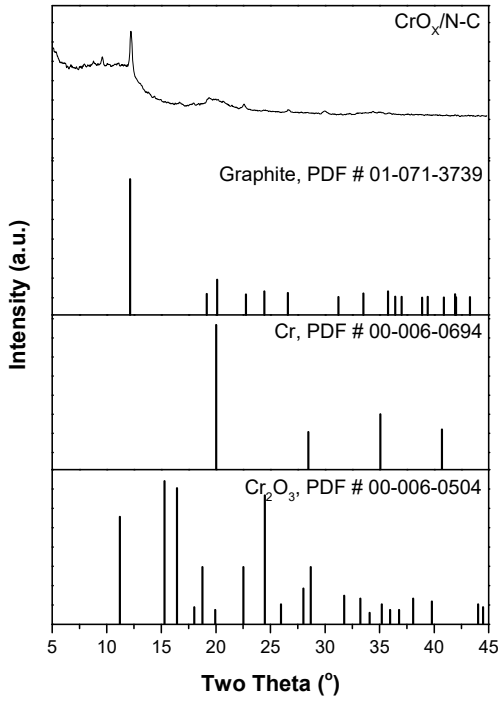

Figure 5.9 Mo-pXRD pattern for CrO_X/N-C after pretreatment at 503 K in helium and the XRD references for graphite, metallic Cr, and Cr_2O_3.

Figure 5.10 shows the STEM-HAADF image of the Cr-CoO_X/N-C catalyst. The high metal loading on an amorphous support resulted in a poor contrast. The particles were typically on the order of 5 nm or less. Occasionally large clusters were observed (10-50 nm). A precise particle size measurement was not obtained as it was challenging to resolve the smallest particles. The particle size observed with Cr-CoO_X/N-C was smaller than the particle size previously observed for CoO_X/N-C (5-10 nm) [119].

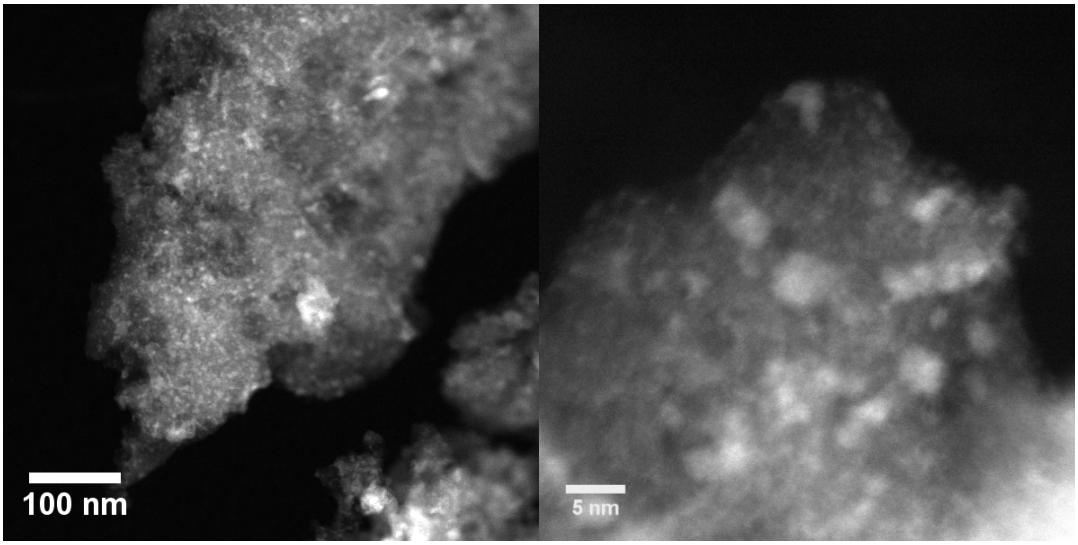

Figure 5.10 Representative STEM-HAADF images of Cr-CoO_X/N-C catalyst.

Figure 5.11 Shows the Co K-edge EXAFS of different catalysts. The first and second shells of CoO_X/N-C align with the spinel Co_3O_4 crystal structure. The first peak (~1.5 Å) in Figure 5.11 b-d is assigned to the nearest Co-O bonds. The second (~2.5 Å) and third peaks (3.1 Å) in Figure 5.11 b-c are from the two Co-Co scattering paths due to the coordination geometries of octahedral and tetrahedral Co sites [162] found in spinel structures. The spectra of Cr-CoO_X/N-C shows similar shells although the features were too weak to definitively identify any Co-Cr scattering. The decrease in amplitude of the Fourier transformed EXAFS (Figure 5.11 d) can be attributed to either an increase in crystalline disorder or a decrease in particle size (i.e. lower coordination numbers). The weak scattering of higher shells (>3.5 Å) is further evidence for the high dispersion of this system. The Cr EXAFS spectra with and without the addition of Co can be found in Figure 5.12.

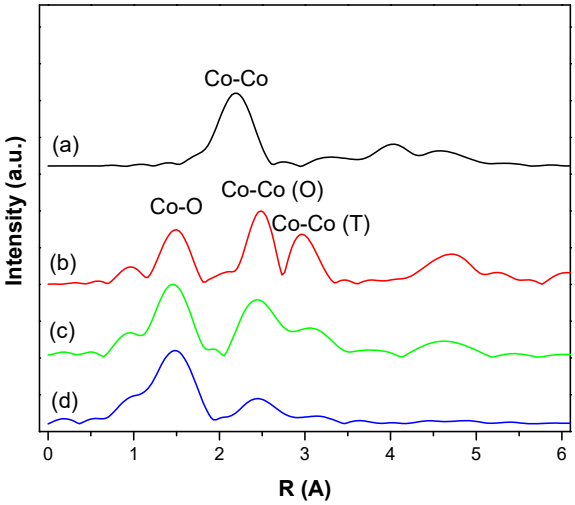

Figure 5.11 The k^3-weighted Fourier-transformed spectra from EXAFS collected at the Co K edge. Key (a): Co foil; (b): Co_3O_4 standard; (c): CoO_X/N-C catalyst; (d): Cr-CoO_X/N-C catalyst. All the catalysts were pretreated at 503 K in helium then cooled to RT prior to the measurement without exposure to air.

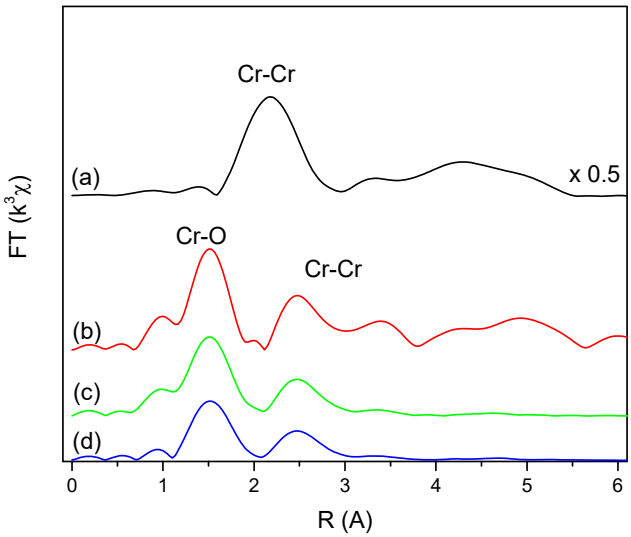

Figure 5.12 The k^3-weighted Fourier transform spectra from EXAFS collected at the Cr K edge. Key (a): Cr foil; (b): Cr2O3 standard; (c): CrOX/N-C catalyst; (d): Cr-CoOX/N-C catalyst. All the catalysts were pretreated at 503 K in helium then cooled to RT prior to the measurement without exposure to the air.

XRD, EXAFS and STEM results indicate a decrease in the particle size of the cobalt oxide on carbon for Cr-CoO_X/N-C compared to CoO_X/N-C, which indicates that the promotional effect of Cr could be due to a geometric effect. Nevertheless, geometric and electronic influences cannot often be separated. The change in geometry could alter the nature of the exposed planes and the topology of the surface sites., while it could also result in a change in the electron bandwidth and binding energies of core electron [160].

When supported and properly calcined on silica, the chromium itself can act as an effective metal site for ethylene polymerization (Philips catalyst). A number of studies have excluded Cr(VI) as an active oxidation state for ethylene conversion [150, 163, 164]. As reported in this study the Cr(III) on carbon was not active for ethylene oligomerization. The introduction of Cr has increased the dispersion and population of Co(II) sites.

5.3.4 Development of a Reaction Kinetics Model

The reaction order with respect to ethylene (7 to 14 bar, 353 K) is close to first order as shown in Figure 5.13 b for the Cr-CoO_X/N-C catalyst. The catalyst suffered from deactivation under the reaction conditions, and the apparent reaction rate is averaged across the entire TOS (Figure 5.14). The ethylene consumption rate was averaged between 3 – 12 h TOS. A Schulz-Flory distribution of oligomer products from ethylene oligomerization was also observed with Cr-CoO_X/N-C (Figure 5.15) at 16.31 h^{-1} WHSV. The observations are consistent with the Cossee-Arlman mechanism, a classic mechanism to describe the carbon-carbon bond-forming step occurring by insertion of the coordinated olefin into the metal-alkyl bond [88, 165]. The reaction pathway (Figure 5.13a) was proposed based on Cossee-Alrman mechanism to describe ethylene chain propagation and 1-butene isomerization. Isomerization of oligomers higher than butene was not considered in the construction of the kinetic model.

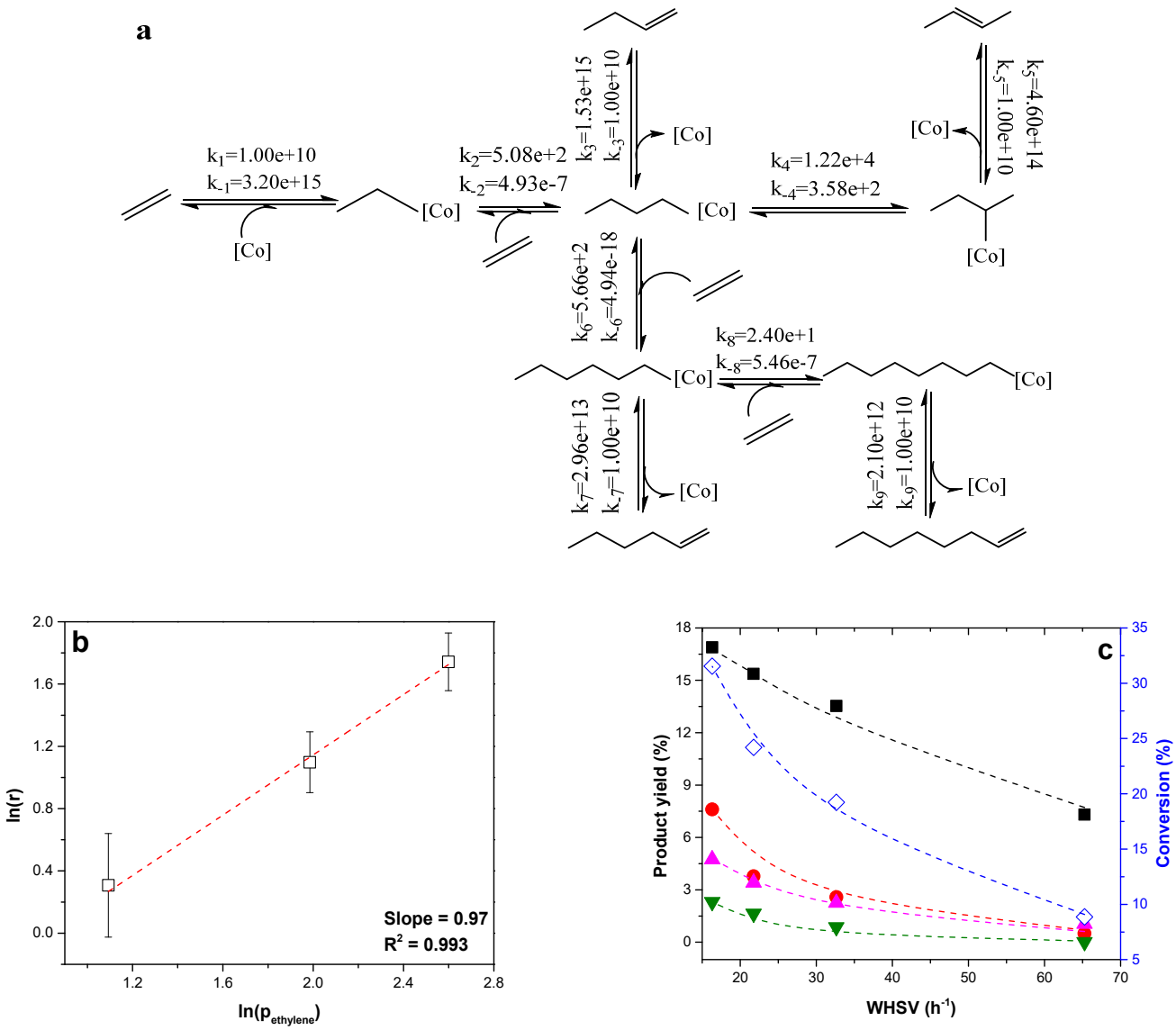

Figure 5.13 Pathway, reaction order, and kinetic model fitting of ethylene oligomerization with Cr-CoO_X/N-C. (a) Proposed reaction pathway for ethylene oligomerization with Cr-CoO_X/N-C. (b) Ethylene consumption rate ($g_{ethylene}/g_{cat}/h$) as a function of ethylene partial pressure (bar). The dotted line represents the linear fitting result. (c) Kinetic model fit (dotted line) with product yield including 1-butene (■), 2-butene (●), hexenes (▲) and octenes (▼), together with ethylene conversion (◇) at different WHSVs.

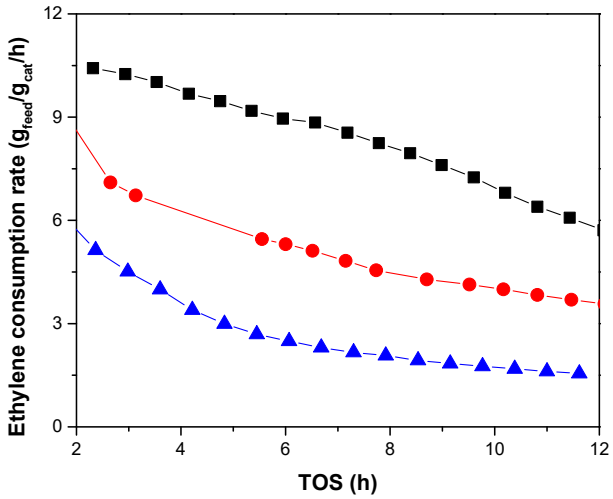

Figure 5.14 Ethylene consumption rate with TOS at ethylene partial pressure of (■) 13.45 bar, (●) 7.28 bar, and (▲) 2.98 bar.

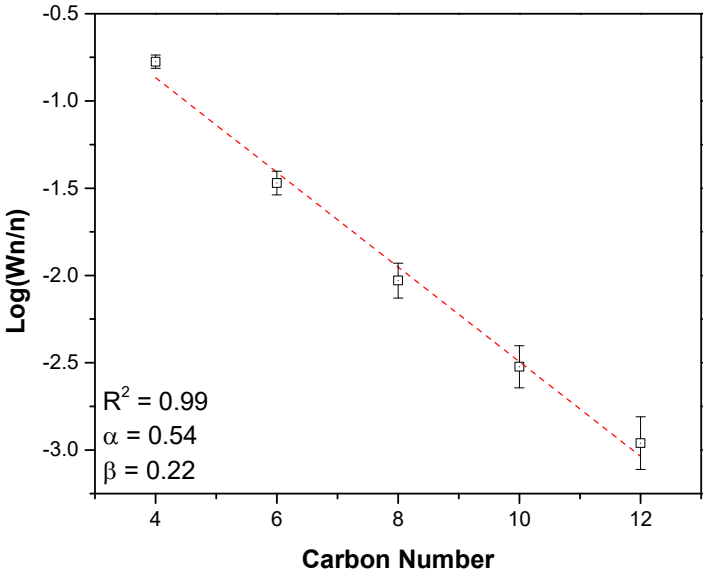

Figure 5.15 Fitting of ethylene oligomer average distribution (between 3-12 h TOS) with Schulz-Flory distribution over Cr-CoO_X/C catalyst. The error bar is added based on standard deviation.

The product selectivity with Cr-CoO_X/N-C was measured at different ethylene conersions as shown in Figure 5.13. The kinetic model was built based on a plug flow reactor (PFR) model, where the concentration of the reactants and products is a function of position in the reactor (catalyst loading). The model-predicted reaction rates and product

yields were obtained by solving the PFR rate equations using the built-in ordinary differential equation solvers in the MATLAB software package. The rate constants of all the adsorption/desorption steps (Steps 1, 3, 5, 7, and 9) were estimated using collision theory [166]. The rate constants of the surface reaction steps (Steps 2, 4, 6, 8) were estimated using transition state theory [167]. Further analyses of the reversibility of each elementary step suggested that all the adsorption/desorption steps were essentially quasi-equilibrated, and the reaction kinetics was mainly determined by surface steps. The four activation energies (Ea_2, Ea_4, Ea_6, and Ea_8, reported in Table 5.2) plus the active site dispersion were adjusted during the model-fitting process so that the predicted product yields matched those collected experimentally. The model predicts an increased energy barrier for the reaction steps forming higher oligomers products. Step four, the 1-butene isomerization step, is kinetically more favored compared to step six, oligomerization, with a 9.4 kJ/mol lower activation energy. It can be inferred that once formed, the linear alpha olefin products are more likely to undergo double bond isomerization to form internal olefins, rather than further oligomerization with ethylene. Our catalyst would thus have better control over the carbon chain length of the oligomer products, and be used as an efficient catalyst to selectively dimerize ethylene into butenes. The same set of reaction rate constants were then used to estimate the active site dispersion for CoO_X/N-C catalyst, by fitting the product yields data collected with this catalyst (Table 5.3) at reaction conditions reported in Figure 5.4. The thermodynamic data of different species was gathered from [168] and adjusted to the reaction conditions. The heats of adsorption of the hydrocarbon species on cobalt oxide were estimated from [120]. The model gives an excellent fit for both catalysts (Figure 5.13c and Table 5.3). The model predicts an active site dispersion of 20.9% and 13.9% for Cr-CoO_X/N-C and CoO_X/N-C, respectively. Based on the characterization results discussed previously, the 50.3% increase in the active site dispersion could be due to 1) the decrease in the cobalt oxide particle size and 2) the increase in the Co(II) composition for Cr-CoO_X/N-C compared to CoO_X/N-C. The higher apparent reaction rate observed from Cr-CoO_X/N-C can be attributed to the increase in the number of active sites per gram of Cr-CoO_X/N-C as compared to CoO_X/N-C catalyst.

Table 5.2 Activation energy fitting results from the reaction kinetic model for both Cr-CoO_X/N-C and CoO_X/N-C.

Step number	Reaction steps	Activation Energy kJ/mol
2	C2* + C2 -> 1-C4*	68.66
4	1-C4* -> 2-C4*	59.33
6	1-C4* + C2 -> 1-C6*	68.34
8	1-C6* + C2 -> 1-C8*	77.62

Table 5.3 Kinetic model fitting results at two WHSVs with CoO_X/N-C catalyst during ethylene oligomerization. Reaction conditions: 353 K, 15 bar ethylene partial pressure balanced in helium. The same set of parameters (reaction rate constants, activation energies, etc.) of Cr-CoO_X/N-C was used to fit the CoO_X/N-C data.

WHSV h^{-1}	1-Butene yield		2-Butene yield		Hexene yield		Octene yield	
	Exp.	Fit	Exp.	Fit	Exp.	Fit	Exp.	Fit
23.44	14.34	14.65	3.96	3.96	2.30	2.91	0.60	0.89
46.89	11.39	9.58	2.67	1.16	1.35	1.00	0.20	0.15

5.3.5 Cr-CoO_X/N-C catalyst for 1-Butene Conversion

The improved activity and stability with Cr-CoO_X/N-C were initially observed during 1-butene conversion. As mentioned in Chapter 3, the CoO_X/N-C catalyst suffered from more rapid deactivation at high WHSV (14.1 h^{-1}). Figure 5.16 compares the activity of Cr-CoO_X/N-C with CoO_X/N-C under the same reaction conditions for 1-butene oligomerization. To prove the reproducibility of the result with Cr-CoO_X/N-C, the same reaction was operated in two fixed-bed reactor systems: reactor 1 (R1) was operated in a down-flow mode – the same reactor system used and described by previous chapters; reactor 2 (R2) was operatred in an up-flow mode which shares the same setup with reactor 1 but with an opposite direction of flow. The Cr-CoO_X/N-C catalyst showed nearly the same oligomer yield and 1-butene total conversion in both reactors. From Figure 5.16 (a), it can be seen that the average oligomer yield with Cr-CoO_X/N-C is two times that of CoO_X/N-C. The 1-butene total conversion drastically decreased from about 90% to about 20% within 9 h TOS with CoO_X/N-C whereas no significant loss of activity was observed with Cr-CoO_X/N-C.

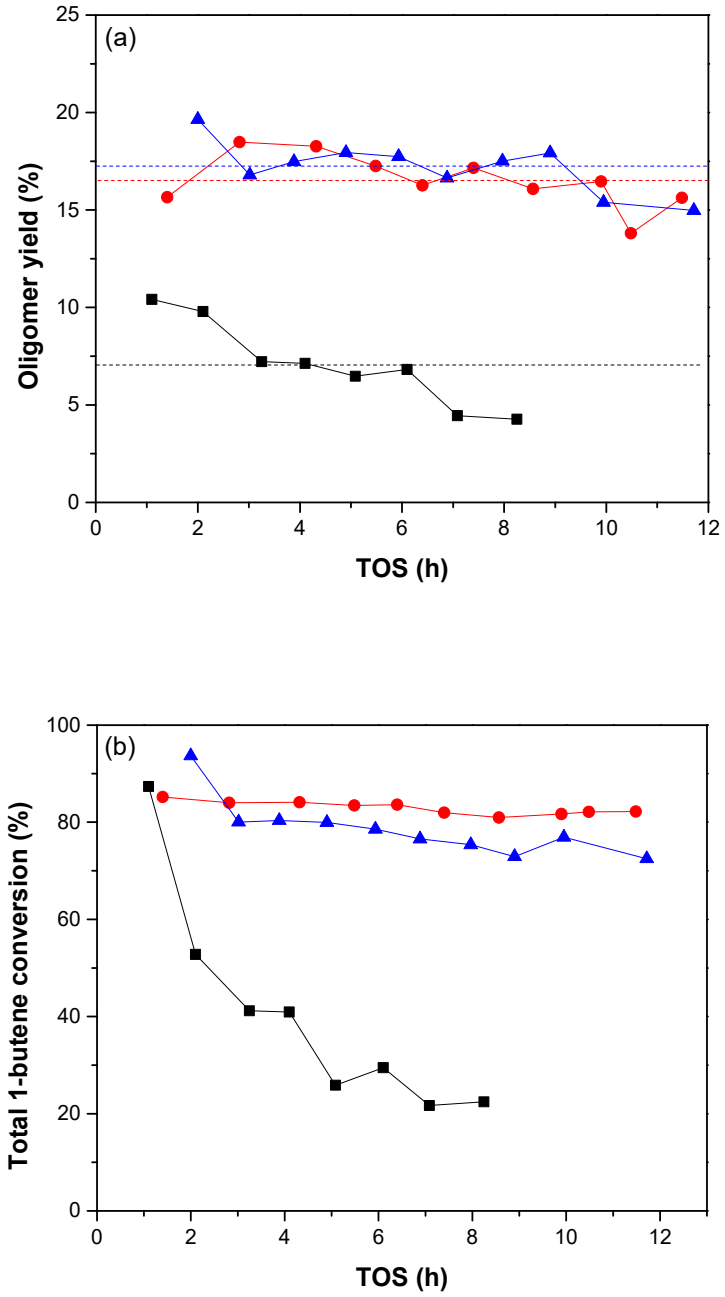

Figure 5.16 A comparison of the oligomer yield (a) and 1-butene total conversion (b) at 80 ℃, 450 psig and 14.1 h^{-1} WHSV with (■) CoO_X/N-C, (●) Cr-CoO_X/N-C R1 and (▲) Cr-CoO_X/N-C R2. The dotted line in (a) represents the average value calculated across the entire TOS tested.

The TGA analysis was conducted for the spent CoO_X/N-C and spent Cr-CoO_X/N-C catalysts after 1-butene conversion. The weight losses between 200 ℃ and 550 ℃ are 11.76% and 7.1% for CoO_X/N-C and Cr-CoO_X/N-C, respectively (Figure 5.17). The weight loss within this temperature range is frequently assigned to the removal of

soft coke possibly caused by oligomer accumulation. The used Cr-CoO_X/N-C catalyst showed 4.66% less soft coke accumulation compared to CoO_X/N-C. This could explain the more stable performance of Cr-CoO_X/N-C during 1-butene oligomerization.

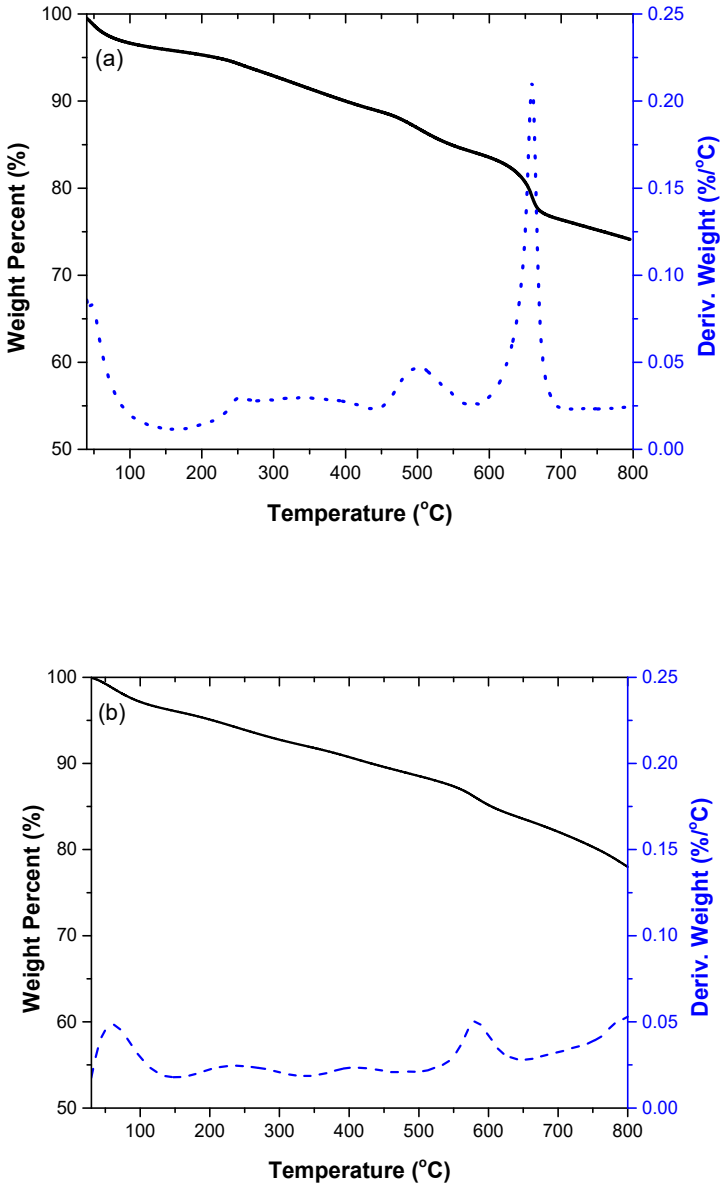

Figure 5.17 TGA analysis of (a) CoO_X/N-C and (b) Cr-CoO_X/N-C after 1-butene conversion as described in Figure 5.16.

Our contemporaneous studies on the NH_3 - treated carbon - supported cobalt oxide catalyst for 1-butene conversion demonstrated a 2.6 times increase in oligomerization selectivity when the carbon support was treated in NH_3 at 800 ℃. The oligomer selectivity of this catalyst is found to have a positive correlation with the content of a pyridine-type N species [141]. This carbon support was used to exam the promotion effect of Cr. The effect of metal loading was investigated about the oligomerization activity for 1-butene conversion. Four catalysts were synthesized using the carbon support treated at 800 ℃ and were compared in parallel for 1-butene oligomerization at a WHSV of 14.1 h^{-1}. The catalysts are denoted as: 13Co/800A_AWC, 8Co5Cr/800A_AWC, 5Co8Cr/800A_AWC, and 3Co10Cr/800A_AWC. The number in front of the metal indicates the metal weight loading of each catalyst based on the carbon support. A_AWC indicates that the carbon support is acid washed and treated in NH_3. And the number 800 in front of the letter A indicates that the carbon support was treated in flowing NH_3 at 800 ℃. Figure 5.18 compares the oligomer yield and the oligomer cobalt-time yield among the four catalysts where the oligomer cobalt-time yield is defined as per mole of oligomer (carbon basis) produced per hour over per mole of cobalt atom in the catalyst, assuming cobalt is the only active metal for every catalyst. From Figure 5.18 (a) it can be seen that the compared to the non-promoted catalyst, both 8Co5Cr/800A_AWC and 5Co8Cr/800A_AWC showed improved stability especially for the initial 6 h TOS. The overall oligomer yields for the Cr promoted catalysts were all higher than that of the non-promoted 13Co/800A_AWC catalyst. The highest oligomer yield was observed with 8Co5Cr/800A_AWC and 5Co8Cr/800A_AWC. Figure 5.18 (b) shows that the addition of Cr has greatly improved the cobalt atomic efficiency in converting 1-butene into oligomer products.

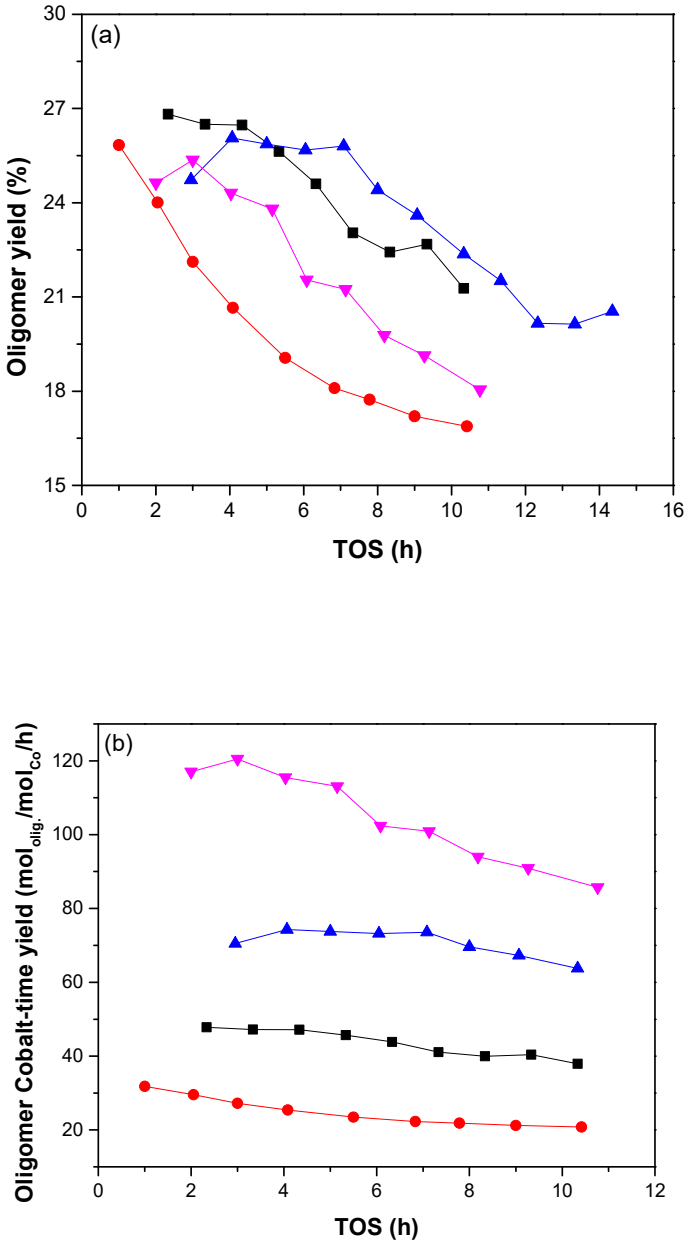

Figure 5.18 Oligomer yield (a) and oligomer cobalt-time yield (b) comparing the carbon supported cobalt catalyst with various cobalt and chromium loadings including: (■) 8Co5Cr/800A_AWC, (●) 13Co/800A_AWC, (▲) 5Co8Cr/800A_AWC and (▼) 3Co10Cr/800A_AWC.

A summary of the product distribution can be found in Table 5.4. An increase in the oligomerization selectivity was observed for all the Cr – promoted catalyst as compared to the non-promoted catalyst. Compared with 13Co/800A_AWC, 8Co5Cr/800A_AWC showed similar total 1-butene conversion, whereas the other two Cr –

promoted catalysts showed declined 1-butene conversion with higher oligomerization selectivities. All the catalysts showed similar linear octene distribution and overall octene distribution.

Table 5.4 Summary and comparison of product selectivity with Cr promoted cobalt catalyst supported on high-temperature ammonia-treated carbon support.

Catalyst		13Co/ 800A_AWC	8Co5Cr/ 800A_AWC	5Co8Cr/ 800A_AWC	3Co10Cr/ 800A_AWC
1-butene feed concentration (mol/L)		9.22	9.22	9.22	9.22
Outlet concentration (mol/L)	1-butene	0.66	0.92	2.07	2.71
	2-butene	6.99	6.47	5.30	4.79
	Linear octene	0.80	0.95	0.99	0.95
	Iso-octene	0.23	0.25	0.24	0.20
	Dodecenes	0.03	0.04	0.03	0.02
	Cetene	5.37×10^{-4}	5.72×10^{-4}	1.31×10^{-3}	4.66×10^{-4}
$(1\text{-butene}/2\text{-butene})_{reaction}/(1\text{-butene}/2\text{-butene})_{equilibrium}$		1.42	2.17	6.63	9.55
Total 1-butene conversion (%)		93.30	90.73	79.09	72.50
Oligomerization selectivity (%)		22.62	26.58	31.85	30.95
Isomerization selectivity (%)		77.38	73.42	68.15	69.05
Oligomerization product distribution (%)	Linear Octene	74.40	75.69	77.76	80.47
	Total Octene	95.90	95.54	96.63	97.36
	Dodecene	4.00	4.37	3.15	2.53
	Cetene	0.10	0.09	0.22	0.11

A detailed specific octene products distribution is summarized in Table 5.5. The Cr-promoted catalyst showed slightly improved linear octene distribution, with an increasing amount of *cis*-2-octene and a decreasing amount of *trans*-3-methyl-2-heptene in the product mixture. *Trans*-3-octene remains the most abundant octene isomer from 1-butene conversion for all the catalysts.

Table 5.5 Detailed specific octene product distribution for the Cr-promoted cobalt catalyst supported with NH_3 treated carbon support at 800 ℃.

Catalyst	Catalyst	13Co/ 800A_AWC	8Co5Cr/ 800A_AWC	5Co8Cr/ 800A_AWC	3Co10Cr/ 800A_AWC
Specific octene distribution(%)	*Cis*-2-octene	6.77	7.37	8.52	9.86
	Trans-2-octene	17.77	18.66	17.18	16.10
	3-octene	46.37	45.45	51.73	54.34
	4-octene	6.58	7.49	3.33	2.38
	Cis-5-methyl-3-heptene	2.39	2.37	2.39	2.36
	Trans-5-methyl-3-heptene	2.62	2.49	2.38	2.31
	Trans-3-methyl-2-heptene	10.09	8.10	7.21	5.82
	Trans-5-methyl-2-heptene	4.01	3.79	3.24	2.92
	Cis-5-methyl-2-heptene	3.39	4.27	4.03	3.90
Linear Octene Distribution (%)		77.59	79.22	80.5	82.67
NCB		0.22	0.21	0.19	0.17

5.4 Conclusion

Cr-CoO_X/N-C catalyst was able to dimerize ethylene into butenes with a 1-butene selectivity of 82.5% at a conversion of 8.9%. The 1-butene selectivity decreases with increasing ethylene conversion due to the formation of 2-butene and higher oligomers. The catalyst showed a low rate of 1-butene double bond isomerization after an initial transient period, which is different from most of the Ni-containing heterogeneous catalysts. Compared to the CoO_X/N-C catalyst, Cr-CoO_X/N-C demonstrated 1.2-1.6 times higher apparent rate in ethylene conversion. The XRD, STEM and EXAFS results have evidenced a decrease of the Co_3O_4 particle size upon addition of Cr. The XANES and XPS results have evidenced a change in the cobalt oxidation state upon Cr addition. The cobalt is more reduced with a higher proportion of Co^{2+} in Cr-CoO_X/N-C than in CoO_X/N-C. At the same time, Cr^{6+} was seen in the Cr-CoO_X/N-C while CrO_X/N-C contains mostly Cr^{3+}. The CrO_X/N-C was not active in ethylene conversion. The Cr-CoO_X/N-C catalyst also demonstrated improved activity and stability during 1-butene conversion. The product selectivity observed during ethylene conversion with Cr-CoO_X/N-C catalyst can be described with Cosee-Arlman mechanism. A simplified kinetic model was constructed to describe the reaction network, which predicted a nearly 50% increase in the active site dispersion that resulted in a higher apparent reaction rate based on the mass of the catalyst.

CHAPTER 6 Conclusions and Suggestions for Future Work

6.1 Conclusions

This thesis demonstrates oligomerization of light alkenes into oligomers with controlled carbon chain length and carbon bone structure using heterogeneous catalysts. Unmodified zeolites produced highly branched oligomers from 1-butene (>99% in selectivity). The Brønsted acid sites within zeolites catalyze olefin conversion based on a carbocation mechanism, where the formation of secondary and tertiary carbocations followed by the production of branched olefins is favored. H-ferrierite showed between 76.8% and 91.6% selectivity of olefinic products when operating 1-butene conversion at supercritical conditions. The products followed a Schulz-Flory product distribution. Oligomer deposition and pore blocking were found to have caused catalyst deactivation. At supercritical conditions, catalyst deactivation rate decreases by 3.8 times, which indicates that the transition from the butene subcritical to supercritical state either removes coke or inhibits its formation.

We were able to obtain above 50% of linear dimer distribution from the conversion of ethylene, propylene, 1-butene and 1-hexene with a carbon supported cobalt oxide catalyst (CoO_X/N-C) without the use of a co-catalyst. This catalyst can be synthesized by a facile wetness impregnation method, where carbon supported cobalt oxide material can be formed by decomposing cobalt nitrate on an NH_4OH-treated carbon support. The reaction requires mild conditions with 80 ℃ reaction temperature and 450 psig total pressure. Olefin feed isomerization was found to be the main side reaction for this catalyst. The product selectivity observed from CoO_X/N-C can be explained with a Cossee-Arlman mechanism. The catalyst is featured by a non-regioselective initial insertion step followed by a regioselective 2,1 insertion step. Linear internal olefin products can be formed following a 2,1-2,1 insertion sequence. The oligomer products observed from both ethylene and 1-butene conversion were found to follow a Schulz-Flory distribution.

The active species for light olefin conversion with CoO_X/N-C is composed of a Co(II) and Co (III) oxide mixture. The carbon support was essential to show activity towards oligomerization. At pretreatment temperatures above 350 ℃, the carbon support reduces the cobalt into lower oxidation states which resulted in a decline in the oligomerization activity. The addition of Cr into CoO_X/N-C catalyst showed improved activity by 1.6 times and stability compared to non-promoted CoO_X/N-C during ethylene and 1-butene oligomerization. The introduction of

Cr was found to slightly reduce Co(III) to Co(II). Additionally, the Cr-promoted catalyst showed an approximately 50% increase in the cobalt active site dispersion as compared to CoO_X/N-C.

Our studies have pointed out that highly dispersed, slightly oxidized cobalt particles supported on base-treated carbon are the important requirements of an active oligomerization catalyst in the production of straight-chain oligomers. Our findings have shown the potential of implementing the cobalt-on-carbon catalyst for the conversion of light alkenes in a continuous flow process without the need of any organic solvent.

6.2 Suggestions for Future Work

Ethylene can be selectively dimerized into 1-butene with Cr-CoO_X/N-C catalyst at ethylene conversions less than 20%. However, increasing conversion decreases 1-butene selectivity because undesired isomerization reactions start to occur. Therefore one critical future direction is to develop improved catalysts that have lower rates of isomerization. Although a similar catalytic technology using MOF-based materials showed 100 times higher activity and selectivity during ethylene conversion compared to Cr-CoO_X/N-C, this previous MOF has drawbacks such as: 1. it requires a co-catalyst to show activity; 2. the tedious synthesis of this material is hardly reproducible with potential difficulty of scaling up; and 3. besides ethylene, it cannot convert other alkene feeds with a high selectivity towards straight-chain oligomers. Based on the positive results we have obtained from our studies, I suggest the following aspects as future research direction:

1) Downstream and upstream process integration with biomass-derived feedstocks. The technology reported by this work can be used to convert molecules derived from renewable resources. For example, the technology of selective oligomerization of light olefins studied here can be coupled with the biomass-derived feedstocks to obtain value-added alcohols with controlled chain structure. 1-Butanol and other primary alcohols generated from the biomass-derived molecules can be made into light alkene feeds to our process, after which a heavier hydrocarbon compound with less branching can be derived that could be used to make fuels and biodiesels. Diesel fuel is composed of highly paraffinic components with a cetane number of above 70, with a mixture of a high percentage of linear paraffins and a small percentage of slightly branched paraffins [169, 170]. Synthetic diesel is currently produced following a Fischer-Tropsch process where the synthesis gas comes from gasification of the raw materials including biomass, biogas, natural gas, coal and others. The light alkene oligomerization technology studied here could provide an alternative route for the production of synthetic diesel bypassing the energy-intensive gasification process.

2) Synthesis of semi-molecular catalysts with ligand treatment. As of today, the production of LAOs with a high yield is still achieved with homogeneous catalysts. It is possible, however, to treat a supported metal moiety with a ligand structure analogy to its homogeneous counterparts in the synthesis of LAOs. With the advancement of catalyst synthesis technology such as atomic layer deposition (ALD) and controlled surface reaction (CSR), it is plausible to synthesize well-controlled metal or metal oxide structure with a specified ligand structure. For example, Camacho-Bunquin J. *et al.* have successfully synthesized a single-site zinc on silica catalyst *via* ALD for propylene

hydrogenation and propane dehydrogenation. The ALD experiments allow for the synthesis of an alkyl-zinc site with a higher dispersion and improved stability by dosing the material with diethylzinc [171]. In this case, the alkyl (ligand) structure has two effects: 1. equipped Zn with a proper electronic configuration and 2. isolated each Zn site making it into a single site catalyst. The synthesis of a highly dispersed and selective catalyst for light alkene oligomerization into LAOs can be realized following the similar principle. Furthermore, the addition of a promoting metal, such as Cr in our studies, can also be achieved by either ALD or CSR technique, possibly forming a better controlled particle size distribution.

3) *Identification of the active site.* During our studies, we have encountered problems such as effectively counting the active cobalt site, identifying the cobalt active site structure, and determining the particle size distribution. This is due to the following two problems: the carbon support we're using is sensitive to high temperature, and it also has a low contrast to the metal oxide of our interest; the metal loading we're using for our catalysts is high (>10 wt.%), which resulted in severely overlapping particles. Future efforts can be done to mitigate such problems by trying various supports and reducing metal loading. Such changes might sacrifice the activity of the catalyst, whereas a much clearer picture about the active site requirement for the catalytic material can be derived.

References

[1] P. Cossee, On the reaction mechanism of the ethylene polymerization with heterogeneous Ziegler-Natta catalysts, Tetrahedron letters, 1 (1960) 12-16.
[2] G.T. Institute, Unlocking the Potential of Unconventional Gas, Pipeline & Gas Journal, 240 (2013).
[3] M.B. Elvira O. Camara Greiner, Yuko Yamaguchi, Chemical Economics Handbook, Linear Alpha-Olefins (681. 5030), in, IHS, 2013.
[4] Oxo Alcohol Market to Reach $20,976.6 Million by 2020, in, Coatings World, 2015.
[5] N. Kashiwa, T. Tokuzumi, H. Fujimura, Process for the polymerization and/or copolymerization of olefins with the use of ziegler-type catalysts supported on carrier, US Patent 3642746, 1972.
[6] M.P. Bailey, Plant watch, Chemical Engineering, 121 (2014) 71-72.
[7] G. Belov, P. Matkovsky, Processes for the production of higher linear α-olefins, Petroleum Chemistry, 50 (2010) 283-289.
[8] H. Sinn, W. Kaminsky, Ziegler-Natta catalysis, Advances in Organometallic Chemistry, 18 (1980) 99-149.
[9] G. Belov, Oligomerization of olefins under the action of zirconium-containing catalysts, Petroleum chemistry, 34 (1994) 105-124.
[10] P. Shi, Y. Liu, S. Peng, S. Liu, Ligand effect of tritdentate versus bidentate coordination on the oligomerization of ethylene, Organometallics, 21 (2002) 3203-3207.
[11] F. Speiser, P. Braunstein, L. Saussine, R. Welter, Nickel complexes with oxazoline-based P, N-chelate ligands: Synthesis, structures, and catalytic ethylene oligomerization behavior, Organometallics, 23 (2004) 2613-2624.
[12] J. Du, L. Han, Y. Cui, J. Li, Y. Li, W.-H. Sun, Synthesis, characterization, and ethylene oligomerization of 2, 6-bis (imino) phenoxy cobalt complexes, Australian journal of chemistry, 56 (2003) 703-706.
[13] B.L. Small, M. Brookhart, Iron-based catalysts with exceptionally high activities and selectivities for oligomerization of ethylene to linear α-olefins, Journal of the American Chemical Society, 120 (1998) 7143-7144.
[14] J.R. Briggs, The selective trimerization of ethylene to hex-1-ene, Journal of the Chemical Society, Chemical Communications, (1989) 674-675.
[15] A. Forestière, H. Olivier-Bourbigou, L. Saussine, Oligomerization of monoolefins by homogeneous catalysts, Oil & Gas Science and Technology-Revue de l'IFP, 64 (2009) 649-667.
[16] Y. Li, Recent Advances in Sulfur Resistant Aromatic Hydrogenation Catalysts, Progress In Chemistry, 6 (2004) 008.
[17] K.P. Tellmann, V.C. Gibson, A.J. White, D.J. Williams, Selective dimerization/oligomerization of α-olefins by cobalt bis (imino) pyridine catalysts stabilized by trifluoromethyl substituents: group 9 metal catalysts with productivities matching those of iron systems, Organometallics, 24 (2005) 280-286.
[18] Y.T. Kim, J.P. Chada, Z. Xu, Y.J. Pagan-Torres, D.C. Rosenfeld, W.L. Winniford, E. Schmidt, G.W. Huber, Low-temperature oligomerization of 1-butene with H-ferrierite, Journal of Catalysis, 323 (2015) 33-44.
[19] J. Franken, C.E.A. Kirschhock, G.M. Mathys, J.A. Martens, Design of a Cobalt-Zeolite Catalyst for Semi-Linear Higher-Olefin Synthesis, Chemcatchem, 4 (2012) 1245-1248.
[20] P. Beltrame, L. Forni, A. Talamini, G. Zuretti, Dimerization of 1-butene over nickel zeolitic catalysts - a search for linear dimers, Appl. Catal. A-Gen., 110 (1994) 39-48.
[21] R.G. Schultz, R.M. Engelbrecht, R.N. Moore, L.T. Wolford, Olefin dimerization over cobalt-oxide-on-carbon catalysts: II. Butene and hexene dimerization, Journal of Catalysis, 6 (1966) 419-424.
[22] F. Cai, C. Lepetit, M. Kermarec, D. Olivier, Dimerization of ethylene into 1-butene over supported tailor-made nickel catalysts, Journal of molecular catalysis, 43 (1987) 93-116.
[23] E.D. Metzger, C.K. Brozek, R.J. Comito, M. Dincă, Selective dimerization of ethylene to 1-butene with a porous catalyst, ACS central science, 2 (2016) 148.
[24] S. Tabak, F. Krambeck, W. Garwood, Conversion of propylene and butylene over ZSM‐5 catalyst, AIChE Journal, 32 (1986) 1526-1531.
[25] K. Wilshier, P. Smart, R. Western, T. Mole, T. Behrsing, Oligomerization of propene over H-ZSM-5 zeolite, Applied catalysis, 31 (1987) 339-359.
[26] R.J. Quann, L.A. Green, S.A. Tabak, F.J. Krambeck, Chemistry of olefin oligomerization over ZSM-5 catalyst, Industrial & engineering chemistry research, 27 (1988) 565-570.

[27] Y. Chu, B. Han, A. Zheng, F. Deng, Influence of acid strength and confinement effect on the ethylene dimerization reaction over solid acid catalysts: A theoretical calculation study, The Journal of Physical Chemistry C, 116 (2012) 12687-12695.
[28] J.A. Martens, R. Ravishankar, I.E. Mishin, P.A. Jacobs, Tailored Alkene Oligomerization with H‐ZSM‐57 Zeolite, Angewandte Chemie International Edition, 39 (2000) 4376-4379.
[29] M. Occelli, J. Hsu, L. Galaya, Propylene oligomerization over molecular sieves: Part i. zeolite effects on reactivity and liquid product selectivities, Journal of molecular catalysis, 32 (1985) 377-390.
[30] A.G. Stepanov, M.V. Luzgin, S.S. Arzumanov, H. Ernst, D. Freude, N-Butene conversion on H-Ferrierite studied by 13C MAS NMR, Journal of Catalysis, 211 (2002) 165-172.
[31] J.P. Pater, P.A. Jacobs, J.A. Martens, Oligomerization of hex-1-ene over acidic aluminosilicate zeolites, MCM-41, and silica-alumina co-gel catalysts: A comparative study, Journal of catalysis, 184 (1999) 262-267.
[32] Y. Iwase, Y. Sakamoto, A. Shiga, A. Miyaji, K. Motokura, T.-r. Koyama, T. Baba, Shape-selective catalysis determined by the volume of a zeolite cavity and the reaction mechanism for propylene production by the conversion of butene using a proton-exchanged zeolite, The Journal of Physical Chemistry C, 116 (2012) 5182-5196.
[33] J.A. Martens, W.H. Verrelst, G.M. Mathys, S.H. Brown, P.A. Jacobs, Tailored catalytic propene trimerization over acidic zeolites with tubular pores, Angewandte Chemie, 117 (2005) 5833-5836.
[34] J.W. Yoon, J.H. Lee, J.-S. Chang, D.H. Choo, S.J. Lee, S.H. Jhung, Trimerization of isobutene over zeolite catalysts: Remarkable performance over a ferrierite zeolite, Catalysis Communications, 8 (2007) 967-970.
[35] C.S.H. Chen, R.F. Bridger, Shape-selective oligomerization of alkenes to near-linear hydrocarbons by zeolite catalysis, Journal of Catalysis, 161 (1996) 687-693.
[36] S. van Donk, E. Bus, A. Broersma, J.H. Bitter, K.P. de Jong, Probing the Accessible Sites for n-Butene Skeletal Isomerization over Aged and Selective H-Ferrierite with d 3-Acetonitrile, Journal of catalysis, 212 (2002) 86-93.
[37] H. Cerqueira, G. Caeiro, L. Costa, F.R. Ribeiro, Deactivation of FCC catalysts, Journal of Molecular Catalysis A: Chemical, 292 (2008) 1-13.
[38] A. Corma, C. Corell, J. Pérez-Pariente, Synthesis and characterization of the MCM-22 zeolite, Zeolites, 15 (1995) 2-8.
[39] S. Ernst, R. Kumar, J. Weitkamp, Studies on the Kinetics of ZSM-23 Crystallization, in, ACS Publications, 1989.
[40] L. Zhang, A.N. van Laak, P.E. de Jongh, K.P. de Jong, Synthesis of large mordenite crystals with different aspect ratios, Microporous and mesoporous materials, 126 (2009) 115-124.
[41] B. De Ménorval, P. Ayrault, N.-S. Gnep, M. Guisnet, Mechanism of n-butene skeletal isomerization over HFER zeolites: a new proposal, Journal of Catalysis, 230 (2005) 38-51.
[42] M. Henry, M. Bulut, W. Vermandel, B. Sels, P. Jacobs, D. Minoux, N. Nesterenko, S. Van Donk, J. Dath, Low temperature conversion of linear C 4 olefins with acid ZSM-5 zeolites of homogeneous composition, Applied Catalysis A: General, 413 (2012) 62-77.
[43] C. Costa, J. Lopes, F. Lemos, F.R. Ribeiro, Activity–acidity relationship in zeolite Y: Part 1. Transformation of light olefins, Journal of Molecular Catalysis A: Chemical, 144 (1999) 207-220.
[44] M. Boronat, P. Viruela, A. Corma, Theoretical study on the mechanism of the hydride transfer reaction between alkanes and alkylcarbenium ions, The Journal of Physical Chemistry B, 101 (1997) 10069-10074.
[45] O. Levenspiel, Experimental search for a simple rate equation to describe deactivating porous catalyst particles, Journal of Catalysis, 25 (1972) 265-272.
[46] O. Levenspiel, The coming-of-age of chemical reaction engineering, Chemical Engineering Science, 35 (1980) 1821-1839.
[47] J.A. Beattie, S. Marple Jr, The Vapor Pressure, Orthobaric Liquid Density, and Critical Constants of 1-Butene, Journal of the American Chemical Society, 72 (1950) 1449-1452.
[48] L. Fan, I. Nakamura, S. Ishida, K. Fujimoto, Ethylene oligomerization on H-ZSM-5 zeolite catalysts in supercritical-phase n-pentane mixtures, Journal of chemical engineering of Japan, 31 (1998) 585-588.
[49] J.C. Gee, S.T. Williams, Dimerization of linear olefins on Amberlyst® 15: Effects of chain length and double-bond position, Journal of catalysis, 303 (2013) 1-8.
[50] M.C. Clark, B. Subramaniam, Extended alkylate production activity during fixed-bed supercritical 1-butene/isobutane alkylation on solid acid catalysts using carbon dioxide as a diluent, Industrial & engineering chemistry research, 37 (1998) 1243-1250.
[51] X. Liu, W. Linghu, X. Li, K. Asami, K. Fujimoto, Effects of solvent on Fischer–Tropsch synthesis, Applied Catalysis A: General, 303 (2006) 251-257.
[52] E. Iglesia, S.C. Reyes, R.J. Madon, Transport-enhanced α-olefin readsorption pathways in Ru-catalyzed hydrocarbon synthesis, Journal of Catalysis, 129 (1991) 238-256.

[53] E. Iglesia, Design, synthesis, and use of cobalt-based Fischer-Tropsch synthesis catalysts, Applied Catalysis A: General, 161 (1997) 59-78.
[54] A.N. Mlinar, P.M. Zimmerman, F.E. Celik, M. Head-Gordon, A.T. Bell, Effects of Brønsted-acid site proximity on the oligomerization of propene in H-MFI, Journal of catalysis, 288 (2012) 65-73.
[55] M. Lallemand, A. Finiels, F. Fajula, V. Hulea, Catalytic oligomerization of ethylene over Ni-containing dealuminated Y zeolites, Applied Catalysis A: General, 301 (2006) 196-201.
[56] M. Lallemand, O.A. Rusu, E. Dumitriu, A. Finiels, F. Fajula, V. Hulea, NiMCM-36 and NiMCM-22 catalysts for the ethylene oligomerization: Effect of zeolite texture and nickel cations/acid sites ratio, Applied Catalysis A: General, 338 (2008) 37-43.
[57] M. Lallemand, O.A. Rusu, E. Dumitriu, A. Finiels, F. Fajula, V. Hulea, Ni-MCM-36 and Ni-MCM-22 catalysts for the ethylene oligomerization, Studies in Surface Science and Catalysis, 174 (2008) 1139-1142.
[58] M.A. Sanchez-Castillo, N. Agarwal, C. Miller, R.D. Cortright, R.J. Madon, J. Dumesic, Reaction kinetics study and analysis of reaction schemes for isobutane conversion over USY zeolite, Journal of Catalysis, 205 (2002) 67-85.
[59] C.S.H. Chen, R.F. Bridger, Shape-Selective Oligomerization of Alkenes to Near-Linear Hydrocarbons by Zeolite Catalysis, Journal of Catalysis, 161 (1996) 687-693.
[60] M.R. Apelian, J.R. Boulton, A.S. Fung, Olefin oligomerization with surface modified zeolite catalyst, US Patent 5284989, 1994.
[61] J.C. Cheng, S. Miseo, S.L. Soled, J.S. Buchanan, J.S. Feeley, Lightly branched higher olefin oligomerization with surface modified zeolite catalyst, US Patent 7759533 B2, 2010.
[62] W. Keim, Oligomerization of Ethylene to α‐Olefins: Discovery and Development of the Shell Higher Olefin Process (SHOP), Angewandte Chemie International Edition, 52 (2013) 12492-12496.
[63] R.D. Broene, M. Brookhart, W.M. Lamanna, A.F. Volpe, Cobalt-catalyzed dimerization of α-olefins to give linear α-olefin products, Journal of the American Chemical Society, 127 (2005) 17194-17195.
[64] A. Bollmann, K. Blann, J.T. Dixon, F.M. Hess, E. Killian, H. Maumela, D.S. McGuinness, D.H. Morgan, A. Neveling, S. Otto, Ethylene tetramerization: a new route to produce 1-octene in exceptionally high selectivities, Journal of the American Chemical Society, 126 (2004) 14712-14713.
[65] J. Zhang, Y. Yan, Q. Chu, J. Feng, Solid phosphoric acid catalyst for propene oligomerization: Effect of silicon phosphate composition, Fuel Processing Technology, (2014).
[66] M. Bjørgen, K.-P. Lillerud, U. Olsbye, S. Bordiga, A. Zecchina, 1-Butene oligomerization in brönsted acidic zeolites: mechanistic insights from low-temperature in situ FTIR spectroscopy, The Journal of Physical Chemistry B, 108 (2004) 7862-7870.
[67] J.F. Knifton, J.R. Sanderson, P.E. Dai, Olefin oligomerization via zeolite catalysis, Catalysis letters, 28 (1994) 223-230.
[68] J. Franken, C.E. Kirschhock, G.M. Mathys, J.A. Martens, Design of a Cobalt‐Zeolite Catalyst for Semi‐Linear Higher‐Olefin Synthesis, ChemCatChem, 4 (2012) 1245-1248.
[69] Y. Chauvin, D. Commereuc, F. Hugues, J. Thivolle-Cazat, Nickel-based heterogeneous catalysts for olefin oligomerization: I. Support and anion effects, Applied catalysis, 42 (1988) 205-216.
[70] M. Vicari, P. Polanek, Oligomerization of olefins to highly linear oligomers, and catalysts for this purpose, EP Patent 0730567 B1, 1998.
[71] J. Qiu, H. Zhang, C. Liang, J. Li, Z. Zhao, Co/CNF catalysts tailored by controlling the deposition of metal colloids onto CNFs: preparation and catalytic properties, Chemistry–A European Journal, 12 (2006) 2147-2151.
[72] L. Xing, J. Qiu, C. Liang, C. Wang, L. Mao, A new approach to high performance Co/C catalysts for selective hydrogenation of chloronitrobenzenes, Journal of Catalysis, 250 (2007) 369-372.
[73] P. Zhang, C. Yu, X. Fan, X. Wang, Z. Ling, Z. Wang, J. Qiu, Magnetically recoverable Ni/C catalysts with hierarchical structure and high-stability for selective hydrogenation of nitroarenes, Physical Chemistry Chemical Physics, 17 (2015) 145-150.
[74] C. Wang, J. Qiu, C. Liang, L. Xing, X. Yang, Carbon nanofiber supported Ni catalysts for the hydrogenation of chloronitrobenzenes, Catalysis Communications, 9 (2008) 1749-1753.
[75] R.G. Schultz, J. Schuck, B. Wildi, Olefin dimerization over cobalt-oxide-on-carbon catalysts: I. Propylene dimerization, Journal of Catalysis, 6 (1966) 385-396.
[76] R.A. Alberty, C.A. Gehrig, Standard chemical thermodynamic properties of alkene isomer groups, Journal of physical and chemical reference data, 14 (1985) 803-820.
[77] J. Shabaker, R. Davda, G. Huber, R. Cortright, J. Dumesic, Aqueous-phase reforming of methanol and ethylene glycol over alumina-supported platinum catalysts, Journal of Catalysis, 215 (2003) 344-352.

[78] K. Toch, J. Thybaut, G. Marin, Ethene oligomerization on Ni-SiO 2-Al 2 O 3: Experimental investigation and Single-Event MicroKinetic modeling, Applied Catalysis A: General, 489 (2015) 292-304.
[79] D.W. Green, Perry's chemical engineers' handbook, McGraw-hill New York, 2008.
[80] C.A. Carrero, C.J. Keturakis, A. Orrego, R. Schomäcker, I.E. Wachs, Anomalous reactivity of supported V_2O_5 nanoparticles for propane oxidative dehydrogenation: influence of the vanadium oxide precursor, Dalton Transactions, 42 (2013) 12644-12653.
[81] J. Lee, S.P. Burt, C.A. Carrero, A.C. Alba-Rubio, I. Ro, B.J. O'Neill, H.J. Kim, D.H. Jackson, T.F. Kuech, I. Hermans, Stabilizing cobalt catalysts for aqueous-phase reactions by strong metal-support interaction, Journal of Catalysis, 330 (2015) 19-27.
[82] C.-W. Tang, C.-B. Wang, S.-H. Chien, Characterization of cobalt oxides studied by FT-IR, Raman, TPR and TG-MS, Thermochimica Acta, 473 (2008) 68-73.
[83] W. Keely, H.W. Maynor, Thermal Studies of Nickel, Cobalt, Iron and Copper Oxides and Nitrates, Journal of Chemical and Engineering Data, 8 (1963) 297-300.
[84] T. Mansoure, Direct fabrication of cobalt oxide nanoparticles employing sucrose as a combustion fuel, Journal of Nanoparticles, 2013 (2013).
[85] S.D. Jackson, F.A. Wigzell, Characterizing the Processes of Calcination and Reduction in the Preparation of Supported Cobalt Catalysts, AIChE Annual Meeting, 2008, Philadelphia.
[86] T. Cseri, S. Bekassy, G. Kenessey, G. Liptay, F. Figueras, Characterization of metal nitrates and clay supported metal nitrates by thermal analysis, Thermochimica acta, 288 (1996) 137-154.
[87] W.-H. Sun, P. Hao, S. Zhang, Q. Shi, W. Zuo, X. Tang, X. Lu, Iron (II) and cobalt (II) 2-(benzimidazolyl)-6-(1-(arylimino) ethyl) pyridyl complexes as catalysts for ethylene oligomerization and polymerization, Organometallics, 26 (2007) 2720-2734.
[88] J.F. Hartwig, Organotransition metal chemistry: from bonding to catalysis, Univ Science Books, 2010.
[89] T. Agapie, Selective ethylene oligomerization: recent advances in chromium catalysis and mechanistic investigations, Coordination chemistry reviews, 255 (2011) 861-880.
[90] J.W. Bae, Y.-J. Lee, J.-Y. Park, K.-W. Jun, Influence of pH of the Impregnation Solution on the Catalytic Properties of Co/γ-Alumina for Fischer− Tropsch Synthesis, Energy & Fuels, 22 (2008) 2885-2891.
[91] Y. Li, C. Lee, B. Gullett, Importance of activated carbon's oxygen surface functional groups on elemental mercury adsorption, Fuel, 82 (2003) 451-457.
[92] J. Lei, H. Dong, X. Duan, W. Chen, G. Qian, D. Chen, X. Zhou, Insights into activated carbon-supported platinum catalysts for base-free oxidation of glycerol, Industrial & Engineering Chemistry Research, 55 (2016) 420-427.
[93] G.R. Jenness, M.A. Christiansen, S. Caratzoulas, D.G. Vlachos, R.J. Gorte, Site-dependent Lewis acidity of γ-Al_2O_3 and its impact on ethanol dehydration and etherification, The Journal of Physical Chemistry C, 118 (2014) 12899-12907.
[94] J. Tittensor, R. Gorte, D. Chapman, Isopropylamine adsorption for the characterization of acid sites in silica-alumina catalysts, Journal of Catalysis, 138 (1992) 714-720.
[95] E. Auer, A. Freund, J. Pietsch, T. Tacke, Carbons as supports for industrial precious metal catalysts, Applied Catalysis A: General, 173 (1998) 259-271.
[96] E. Furimsky, Carbons and carbon supported catalysts in hydroprocessing, Royal Society of Chemistry, 2008.
[97] P.U. Karanjkar, S.P. Burt, X. Chen, K.J. Barnett, M.R. Ball, M.D. Kumbhalkar, X. Wang, J.B. Miller, I. Hermans, J.A. Dumesic, Effect of carbon supports on RhRe bifunctional catalysts for selective hydrogenolysis of tetrahydropyran-2-methanol, Catalysis Science & Technology, 6 (2016) 7841-7851.
[98] F.A. Al-Sherehy, IFP-SABIC process for the selective ethylene dimerization to butene-1, Studies in Surface Science and Catalysis, 100 (1996) 515-523.
[99] R.F. Leary, H.T. Oakley, J.F. Mckay, Steam cracking of light naphtha and preparation of resins, in, US Patent 2964504 A, 1960.
[100] T. Kaufmann, A. Kaldor, G. Stuntz, M. Kerby, L. Ansell, Catalysis science and technology for cleaner transportation fuels, Catalysis Today, 62 (2000) 77-90.
[101] C.H. Bartholomew, Recent technological developments in Fischer-Tropsch catalysis, Catalysis Letters, 7 (1990) 303-315.
[102] E. Crooks, US Shale Gas Sparks a Chemical Revolution, in: Financial Times, URL: https://www.ft.com/content/d1a183d2-40a3-11e2-aafa-00144feabdc0, 2012.
[103] G. Bellussi, F. Mizia, V. Calemma, P. Pollesel, R. Millini, Oligomerization of olefins from Light Cracking Naphtha over zeolite-based catalyst for the production of high quality diesel fuel, Microporous and Mesoporous Materials, 164 (2012) 127-134.

[104] P.-A.R. Breuil, L. Magna, H. Olivier-Bourbigou, Role of Homogeneous Catalysis in Oligomerization of Olefins: Focus on Selected Examples Based on Group 4 to Group 10 Transition Metal Complexes, Catalysis Letters, 145 (2015) 173-192.
[105] F.-J. Wu, Ethylene oligomerization, US Patent 5744677 A, 1998.
[106] A.K. Tomov, J.J. Chirinos, R.J. Long, V.C. Gibson, M.R. Elsegood, An unprecedented α-olefin distribution arising from a homogeneous ethylene oligomerization catalyst, Journal of the American Chemical Society, 128 (2006) 7704-7705.
[107] L.H. Slaugh, G.W. Schoenthal, Ethylene oligomerization catalyst and process, US Patent 5043515 A, 1991.
[108] A. Finiels, F. Fajula, V. Hulea, Nickel-based solid catalysts for ethylene oligomerization – a review, Catalysis Science & Technology, 4 (2014) 2412.
[109] G.P. Belov, P.E. Matkovsky, Processes for the production of higher linear α-olefins, Petroleum Chemistry, 50 (2010) 283-289.
[110] A. de Klerk, D.O. Leckel, N.M. Prinsloo, Butene oligomerization by phosphoric acid catalysis: Separating the effects of temperature and catalyst hydration on product selectivity, Industrial & engineering chemistry research, 45 (2006) 6127-6136.
[111] D.S. McGuinness, J.A. Suttil, M.G. Gardiner, N.W. Davies, Ethylene Oligomerization with Cr− NHC Catalysts: Further Insights into the Extended Metallacycle Mechanism of Chain Growth, Organometallics, 27 (2008) 4238-4247.
[112] A.K. Tomov, V.C. Gibson, G.J. Britovsek, R.J. Long, M. van Meurs, D.J. Jones, K.P. Tellmann, J.J. Chirinos, Distinguishing chain growth mechanisms in metal-catalyzed olefin oligomerization and polymerization systems: C_2H_4/C_2D_4 co-oligomerization/polymerization experiments using chromium, iron, and cobalt catalysts, Organometallics, 28 (2009) 7033-7040.
[113] T. Agapie, S.J. Schofer, J.A. Labinger, J.E. Bercaw, Mechanistic studies of the ethylene trimerization reaction with chromium-diphosphine catalysts: Experimental evidence for a mechanism involving metallacyclic intermediates, Journal of the American Chemical Society, 126 (2004) 1304-1305.
[114] W. Janse van Rensburg, C. Grové, J.P. Steynberg, K.B. Stark, J.J. Huyser, P.J. Steynberg, A DFT study toward the mechanism of chromium-catalyzed ethylene trimerization, Organometallics, 23 (2004) 1207-1222.
[115] R. Raucoules, T. de Bruin, P. Raybaud, C. Adamo, Theoretical Unraveling of Selective 1-Butene Oligomerization Catalyzed by Iron− Bis (arylimino) pyridine, Organometallics, 28 (2009) 5358-5367.
[116] R.D. Broene, M. Brookhart, W.M. Lamanna, A.F. Volpe Jr, Cobalt-Catalyzed Dimerization of γ-Olefins to Give Linear γ-Olefin Products, (2005).
[117] R.Y. Brogaard, U. Olsbye, Ethene Oligomerization in Ni-Containing Zeolites: Theoretical Discrimination of Reaction Mechanisms, ACS Catalysis, 6 (2016) 1205-1214.
[118] R.G. Schultz, Olefin dimerization over cobalt-oxide-on-carbon catalysts: III. Oligomerization of ethylene, Journal of Catalysis, 7 (1967) 286-290.
[119] Z. Xu, J.P. Chada, D. Zhao, C.A. Carrero, Y.T. Kim, D.C. Rosenfeld, J.L. Rogers, S.J. Rozeveld, I. Hermans, G.W. Huber, Production of Linear Octenes from Oligomerization of 1-Butene over Carbon Supported Cobalt Catalysts, ACS Catalysis, 6 (2016) 3815-3825.
[120] Y. Moro-oka, Heats of adsorption for C 4, C 5 and C 6 hydrocarbons on cobalt oxide determined by gas chromatography, Transactions of the Faraday Society, 67 (1971) 3381-3387.
[121] A. Tavakoli, M. Sohrabi, A. Kargari, Application of Anderson–Schulz–Flory (ASF) equation in the product distribution of slurry phase FT synthesis with nanosized iron catalysts, Chemical Engineering Journal, 136 (2008) 358-363.
[122] J. Patzlaff, Y. Liu, C. Graffmann, J. Gaube, Studies on product distributions of iron and cobalt catalyzed Fischer–Tropsch synthesis, Applied Catalysis A: General, 186 (1999) 109-119.
[123] G. Lappin, L. Nemec, J. Sauer, J. Wagner, Higher Olefins; Kirk-Othmer Encyclopedia of Chemical Technology, in, Wiley & Sons, Inc.: New York, NY, USA, 2000.
[124] A. Al-Jarallah, J. Anabtawi, M. Siddiqui, A. Aitani, A. Al-Sa'doun, Ethylene dimerization and oligomerization to butene-1 and linear α-olefins: a review of catalytic systems and processes, Catalysis Today, 14 (1992) 1-121.
[125] E.D. Metzger, R.J. Comito, C.H. Hendon, M. Dinca, Mechanism of Single-Site Molecule-Like Catalytic Ethylene Dimerization in Ni-MFU-4l, Journal of the American Chemical Society, (2017).
[126] S.P.G. Platts, US Gulf Coast ethane prices fall to 10-year low on high inventories, in, S&P Global Platts, http://www.platts.com, 2012.
[127] E. Schwartzel, Drillers rattled as ethane, propane prices plunge, in: Pressreader, Pressreader, http://www.pressreader.com, 2012.

[128] D.S. McGuinness, Olefin oligomerization via metallacycles: dimerization, trimerization, tetramerization, and beyond, Chemical reviews, 111 (2010) 2321-2341.
[129] C.O. Carter, Surface conditioning in olefin dimerization reactors, US Patent 4538018, 1985.
[130] C.O. Carter, Olefin dimerization, US Patent 4309387, 1982.
[131] D.M. Maschmeyer, A.E. Fowler, S.A. Sims, G.E. White, Process for making a mixture of ethylene and butene-1, US Patent 4484016 A, 1984.
[132] A.W. Al-Sa'doun, Dimerization of ethylene to butene-1 catalyzed by Ti (OR') 4-AlR3, Applied Catalysis A: General, 105 (1993) 1-40.
[133] Y. Okamoto, N. Ishida, T. Imanaka, S. Teranishi, Active states of rhodium in rhodium exchanged Y zeolite catalysts for hydrogenation of ethylene and acetylene and dimerization of ethylene studied with X-ray photoelectron spectroscopy, Journal of Catalysis, 58 (1979) 82-94.
[134] M. Hartmann, A. Pöppl, L. Kevan, Ethylene dimerization and butene isomerization in nickel-containing MCM-41 and AlMCM-41 mesoporous molecular sieves: an electron spin resonance and gas chromatography study, The Journal of Physical Chemistry, 100 (1996) 9906-9910.
[135] J.R. Sohn, D.C. Shin, New Catalyst of NiO–ZrO_2/WO_3 for Ethylene Dimerization, Journal of Catalysis, 160 (1996) 314-316.
[136] A. Hwang, S. Kim, G. Kwak, S.K. Kim, H.-G. Park, S.C. Kang, K.-W. Jun, Y.T. Kim, Low Temperature Oligomerization of Ethylene over Ni/Al-KIT-6 Catalysts, Catalysis Letters, (2017) 1-12.
[137] A. Peter W. Glockner, Kenneth W. Barnett, Ethylene oligomerization, in: S.O. Co. (Ed.), US, 1970.
[138] M.R. Ort, J.M. Schuck, R.G. Schultz, Polymerization process and cobalt oxide-metal oxide catalyst therefor, US Patent 3333017 A, 1967.
[139] T.H. Leslie Ernest Addy, Improvements relating to the oligomerisation of olefines and catalysts therefor, US Patent 1102298 A, 1966.
[140] T. Hill, Olefin oligomerization Catalysts, GB Patent 1183201, 1967.
[141] D. Zhao, Z. Xu, J.P. Chada, C.A. Carrero, D.C. Rosenfeld, J.L. Rogers, I. Hermans, G.W. Huber, Cobalt oxide on N-doped carbon for 1-butene oligomerization to produce linear octenes, ACS Catalysis, (2017).
[142] Z. Xu, D. Zhao, J.P. Chada, D.C. Rosenfeld, J.L. Rogers, I. Hermans, G.W. Huber, Olefin conversion on nitrogen-doped carbon-supported cobalt catalyst: Effect of feedstock, Journal of Catalysis, 354 (2017) 213-222.
[143] G.W. Huber, J.W. Shabaker, S.T. Evans, J.A. Dumesic, Aqueous-phase reforming of ethylene glycol over supported Pt and Pd bimetallic catalysts, Applied Catalysis B: Environmental, 62 (2006) 226-235.
[144] D. Simonetti, E. Kunkes, J. Dumesic, Gas-phase conversion of glycerol to synthesis gas over carbon-supported platinum and platinum–rhenium catalysts, Journal of Catalysis, 247 (2007) 298-306.
[145] G.W. Huber, J. Shabaker, J. Dumesic, Raney Ni-Sn catalyst for H2 production from biomass-derived hydrocarbons, Science, 300 (2003) 2075-2077.
[146] N. Markovic, T. Schmidt, V. Stamenkovic, P. Ross, Oxygen reduction reaction on Pt and Pt bimetallic surfaces: a selective review, Fuel cells - Weinheim, 1 (2001) 105-116.
[147] E. Iglesia, S.L. Soled, R.A. Fiato, G.H. Via, Bimetallic synergy in cobalt ruthenium Fischer-Tropsch synthesis catalysts, Journal of Catalysis, 143 (1993) 345-368.
[148] M.C. Bahome, L.L. Jewell, K. Padayachy, D. Hildebrandt, D. Glasser, A.K. Datye, N.J. Coville, Fe-Ru small particle bimetallic catalysts supported on carbon nanotubes for use in Fischer–Tröpsch synthesis, Applied Catalysis A: General, 328 (2007) 243-251.
[149] R. Manyik, W. Walker, T. Wilson, A soluble chromium-based catalyst for ethylene trimerization and polymerization, Journal of Catalysis, 47 (1977) 197-209.
[150] D.D. Beck, J.H. Lunsford, The active site for ethylene polymerization over chromium supported on silica, Journal of Catalysis, 68 (1981) 121-131.
[151] A. Athena, HEPHAESTUS: data analysis for x-ray absorption spectroscopy using IFEFFIT Ravel, B.; Newville, M, Journal of Synchrotron Radiation, 12 (2005) 537-541.
[152] Z. Xu, D. Zhao, J.P. Chada, D.C. Rosenfeld, J.L. Rogers, I. Hermans, G.W. Huber, Olefin Conversion on Nitrogen-doped Carbon-Supported Cobalt Catalyst: Effect of Feedstock, Journal of Catalysis, (2017).
[153] A.V. Naumkin, A. Kraut-Vass, C.J. Powell, NIST X-ray photoelectron spectroscopy database, Measurement Services Division of the National Institute of Standards and Technology (NIST) Technology Services, 2008.
[154] U.D. Wdowik, K. Parlinski, Lattice dynamics of CoO from first principles, Physical Review B, 75 (2007) 104306.
[155] Z.-X. Shen, J. Allen, P. Lindberg, D. Dessau, B. Wells, A. Borg, W. Ellis, J. Kang, S.-J. Oh, I. Lindau, Photoemission study of CoO, Physical Review B, 42 (1990) 1817.

[156] S.C. Petitto, E.M. Marsh, G.A. Carson, M.A. Langell, Cobalt oxide surface chemistry: the interaction of CoO (100), Co 3 O 4 (110) and Co 3 O 4 (111) with oxygen and water, Journal of Molecular Catalysis A: Chemical, 281 (2008) 49-58.
[157] X. Zhang, C. van den Bos, W. Sloof, H. Terryn, A. Hovestad, J. de Wit, Effect of Drying Temperature on Chromate Conversion Coatings on Zinc, Journal of Corrosion Science & Engineering, 6 (2003).
[158] Y. Zhang, S. Kumar Megarajan, X. Xu, J. Lu, H. Jiang, Catalytic Abatement of Nitrous Oxide Coupled with Ethane Oxydehydrogenation over Mesoporous Cr/Al_2O_3 Catalyst, Catalysts, 7 (2017) 137.
[159] S. Hu, L. Scudiero, S. Ha, Electronic effect on oxidation of formic acid on supported Pd–Cu bimetallic surface, Electrochimica Acta, 83 (2012) 354-358.
[160] B. Coq, F. Figueras, Bimetallic palladium catalysts: influence of the co-metal on the catalyst performance, Journal of Molecular Catalysis A: Chemical, 173 (2001) 117-134.
[161] W.-Y. Li, L.-N. Xu, J. Chen, Co3O4 nanomaterials in lithium‐ion batteries and gas sensors, Advanced Functional Materials, 15 (2005) 851-857.
[162] H.-Y. Wang, S.-F. Hung, H.-Y. Chen, T.-S. Chan, H.M. Chen, B. Liu, In operando identification of geometrical-site-dependent water oxidation activity of spinel Co_3O_4, J. Am. Chem. Soc, 138 (2016) 36-39.
[163] A. Zecchina, E. Groppo, Surface chromium single sites: open problems and recent advances, in: Proc. R. Soc. A, The Royal Society, 2012, pp. 2087-2098.
[164] D.L. Myers, J.H. Lunsford, Silica-supported chromium catalysts for ethylene polymerization: The active oxidation states of chromium, Journal of Catalysis, 99 (1986) 140-148.
[165] E. Arlman, P. Cossée, Ziegler-Natta catalysis I. Mechanism of polymerization of α-olefins with Ziegler-Natta catalysts. Journal of Ctalysis, 3 (1964), 80-88.
[166] K.W. Kolasinski, Surface science: foundations of catalysis and nanoscience, 3rd ed., John Wiley & Sons, 2012; p 267-303.
[167] H. Eyring, The activated complex in chemical reactions, The Journal of Chemical Physics, 3 (1935) 107-115.
[168] C.L. Yaws, Chemical properties handbook, McGraw-Hill, 1999.
[169] P. Schaberg, Application of Synthetic Diesel Fuels, in: 11^{th} Diesel Engine Emissions Reduction Conference, Sasol Technology, Chicago, 2015.
[170] G. Rosinski, Cetane Improvement in Diesel Hydrotreating, in: C. Olsen (Ed.), ART Catalagram, Chicago, 2009.
[171] J. Camacho-Bunquin, P. Aich, M. Ferrandon, U. Das, F. Dogan, L.A. Curtiss, J.T. Miller, C.L. Marshall, A.S. Hock, P.C. Stair, Single-site zinc on silica catalysts for propylene hydrogenation and propane dehydrogenation: Synthesis and reactivity evaluation using an integrated atomic layer deposition-catalysis instrument, Journal of Catalysis, 345 (2017) 170-182.